Inaugural-Dissertation

zur Erlangung der Doktorwürde (Dr. rer. nat.)

der Gesamtfakultät für

Mathematik, Ingenieur- und Naturwissenschaften

der Ruprecht-Karls-Universität Heidelberg

vorgelegt von

Parvathi Valsalan

Tag der mündlichen Prüfung: 04-07-2025

Strong Light-Matter Coupling with N-Heteropolycycles

Gutachter: Prof. Dr. Jana Zaumseil

Prof. Dr. Oriol Vendrell

Abstract

In optical microcavities, strong light–matter coupling gives rise to exciton polaritons, hybrid light–matter states formed through the interaction between confined photons and molecular excitons. While the criteria for achieving strong coupling are well established, the influence of molecular properties on lower polariton (LP) population and polariton-mediated energy transfer remains underexplored.

This thesis investigates the potential of N-heteropolycycle-based systems as versatile platforms for strong light–matter coupling in organic microcavities, aiming to deepen insight into exciton–polariton phenomena in molecular materials. Three primary objectives were pursued. First, the viability of N-heteropolycycles for polariton formation was established using thioether-functionalized tetraazaperylene (TFTAP) derivatives (Butyl-, Benzyl-, and p-methoxybenzyl (PMB)-TFTAP) embedded in polystyrene matrices within metal-clad microcavities. Angle-resolved reflectivity and photoluminescence (PL) spectroscopy confirmed polariton formation, with Rabi splitting energies ranging from 40 to 241 meV—comparable to established organic systems. Polariton properties were tuned via cavity thickness and emitter concentration, validating the collective and coherent nature of the coupling. Second, polariton relaxation pathways in vibronically active tetraazacoronene (TAC) trimer systems were explored, revealing detuning-dependent contributions from radiative pumping (RP) and vibrationally assisted scattering (VAS). Spectral signatures indicated that resonance between states and vibronic or Raman-active modes enhances LP population, offering mechanistic insights relevant to low-threshold polariton lasing. Third, polariton-mediated energy transfer was investigated in multilayer microcavities incorporating donor–acceptor pairs (ATTO 680–IRDye and ATTO 655–IRDye). Systems with larger exciton energy offsets exhibited enhanced acceptor emission due to modulation of polariton composition, establishing energy offset as a key parameter for efficient energy transfer design.

Zusammenfassung

In optischen Mikrokavitäten führt starke Licht–Materie-Kopplung zur Bildung von Exziton-Polaritonen – hybriden Licht–Materie-Zuständen, die durch die Wechselwirkung zwischen eingeschlossenen Photonen und molekularen Exzitonen entstehen. Während die Kriterien für das Erreichen starker Kopplung gut etabliert sind, bleibt der Einfluss molekularer Eigenschaften auf die Besetzung des unteren Polaritons (LP) und den polaritonvermittelten Energietransfer bislang weitgehend unerforscht.

Diese Dissertation untersucht das Potenzial von N-Heteropolycyclen als vielseitige Plattformen für starke Licht–Materie-Kopplung in organischen Mikrokavitäten, mit dem Ziel, ein vertieftes Verständnis von Exziton–Polaritonen in molekularen Materialien zu gewinnen. Drei Hauptziele wurden verfolgt. Erstens wurde die Eignung von N-Heteropolycyclen zur Polaritonenbildung anhand von TFTAP-Derivaten (Butyl-, Benzyl- und PMB-TFTAP) gezeigt, die in Polystyrolmatrizes innerhalb metallbeschichteter Mikrokavitäten eingebettet waren. Winkelaufgelöste Reflexions- und PL-Spektroskopie bestätigten die Bildung von Polaritonen mit Rabi-Splitting-Energien im Bereich von 40 bis 241 meV – vergleichbar mit etablierten organischen Systemen. Die Eigenschaften der Polaritonen wurden durch Variation der Kavitätsdicke und der Emittermolekülkonzentration gezielt eingestellt, was die kollektive und kohärente Natur der Kopplung belegt. Zweitens wurden Relaxationspfade von Polaritonen in vibronisch aktiven TAC-Trimersystemen untersucht, wobei detuningabhängige Beiträge von RP und VAS festgestellt wurden. Spektrale Signaturen zeigten, dass eine Resonanz zwischen -Zuständen und vibronischen oder Raman-aktiven Moden die LP-Besetzung erhöht und somit mechanistische Einblicke liefert, die für das Design von Polaritonenlasern mit niedriger Schwelle relevant sind. Drittens wurde der polaritonvermittelte Energietransfer in mehrschichtigen Mikrokavitäten mit Donor–Akzeptor-Paaren (ATTO 680–IRDye und ATTO 655–IRDye) untersucht. Systeme mit größeren Exzitonen-Energieunterschieden zeigten eine verstärkte Akzeptoremission infolge einer veränderten Polaritonen-Zusammensetzung, wodurch der Energieversatz als Schlüsselparameter für ein effizientes Energietransferdesign identifiziert wurde.

Acknowledgements

I believe that any meaningful accomplishment is rarely achieved alone; it is shaped and supported by many people along the way. I am deeply grateful to everyone who has contributed to this journey.

First and foremost, I would like to sincerely thank Prof. Dr. Jana Zaumseil for the opportunity to pursue my doctoral studies in her group. I'm especially grateful for her trust in my work, the opportunities to learn and grow, and her inspiring mentorship. I also appreciate her feedback on my thesis draft. Attending EMRS Spring 2024, presenting a poster, and connecting with inspiring people was a great experience.

I would also like to thank Prof. Dr. Oriol Vendrell, my second committee member, for his time and willingness to evaluate this thesis.

It's been a pleasure working alongside all my colleagues in the Nanomaterials for Optoelectronics (NMOE) group and beyond—Abdurrahman Ali El Yumin, Angus Hawkey, Daniel Heimfarth, Elisa Fresta, Finn Sebastian, Jan Gotthardt, Manuel Hertzog, Nicolas Zorn, Niklas Herrmann, Sebastian Grieger, Sebastian Lindenthal, Simon R. Wald, Simon Settele, Sonja Wieland, Xabier Rodríguez-Martínez, Xuqiang Xu, Yachen Li, and Yan Huang. I've really valued the insightful conversations, the technical support, and the positive, collaborative atmosphere we shared. I'll always remember the laughs, coffee breaks, and fun times outside the lab as well.

A special mention goes to Manuel Hertzog, who offered guidance during the early phase of my research. I'm also thankful to Jan Lüttgens, who was always patient and generous with his time whenever I had questions about experimental setups or general lab work. Ali was incredibly helpful whenever I ran into issues with the Fourier setup—such a core part of my project. I'm equally appreciative of Nicolas, Simon S., Finn, and Sebastian L. for their help with the TCSPC setup and for being supportive throughout. Niklas Herrmann, it was great sharing an office with you. I have always enjoyed our conversations and your insights. And to Sonja, Martin, Yachen, Elisa, and Yan—from hikes to dinners to all our good talks, it meant a lot to share this time with you.

I've also benefited from the steady support of the technical and administrative staff at the Institute of Applied Physical Chemistry. Ms. Isabella deserves special recognition for

her consistent and timely help with administrative matters.

The financial support provided by SFB 1249 made this work possible, and I'm sincerely appreciative of that. I also had the pleasure of collaborating with Dr. Tobias Wesp and Dr. Robert Eichelmann from Prof. Lutz H. Gade's group, whose contributions enriched this work.

Several people took the time to read and comment on parts of my thesis—Felix, Jan L, Martin, and Niklas —your feedback was truly helpful. I also appreciate the encouragement and support from Sergio and the academic writing group during the writing phase.

To Felix, your presence has been my greatest strength throughout this journey. Special appreciation to Shilauni for always wishing the best for me and being a constant source of motivation. To Sankeerth, it meant a lot to have someone to share ideas and progress with during this process. To my dear friends—Adarsh, Amrutha, Drishya, Liz, Mruthul, Nada, Rosmi, Saumya, Sarona, Sreelakshmi, Thabassum, and Theja—you've brought joy, comfort, and perspective along the way. Whether near or far, you've been part of what kept me going.

And finally, to my family—Amma, Achaa, and Kuttu, Shylaja P. M., Valsalan M., and Sanesh P. M. Your love and belief in me have carried me through. This achievement is as much yours as it is mine. Thank you for being my foundation and my strength.

Contents

List of Tables

List of Abbreviations

CHO	coupled harmonic oscillator
DBR	distributed Bragg reflectors
ER	exciton reservoir
FRET	Förster resonance energy transfer
FWHM	full width half maxima
IR Dye	IR Dye800CW carboxylate
JC	Jaynes-Cummings
LP	lower polariton
MeLPPP	methyl-substituted ladder-type poly(p-phenylene)
MP	middle polariton
NHP	N-Heteropolycyclic
NIR	near-infrared
NTCDA	1,4,5,8- naphthalenetetracarboxylic dianhydride
PAH	polycyclic aromatic hydrocarbons
PDI	perylene diimides
PL	photoluminescence
PLQY	photoluminescence quantum yield

PMB p-methoxybenzyl
PS polystyrene
PVA polyvinyl alcohol

RP radiative pumping

SPAD Single Photon Avalanche Diode
SWCNT single-walled carbon nanotubes

TAC tetraazacoronene
TADF 2,7-bis[9,9-di(4-methylphenyl)-fluoren-2-yl]-9,9-di(4-methylphenyl)fluorine
TC Tavis-Cummings
TCSPC time-correlated single-photon counting
TE transverse electric
TFTAP thioether-functionalized tetraazaperylene
TM transverse magnetic
TMM transfer matrix method

UP upper polariton

VAS vibrationally assisted scattering

1. Introduction

The interaction between light and matter lies at the heart of numerous phenomena in modern physics and chemistry. This interplay governs fundamental processes such as absorption, emission, and energy transfer in molecular systems, and it underpins a wide range of technological applications, from photovoltaics and lasers to quantum optics and information processing. [1, 2] In everyday situations around us, light and matter typically interact only weakly, with energy exchange between a photon and an exciton—an electron-hole pair bound by Coulomb attraction—occurring in an inefficient, dissipative manner. However, when the coupling strength between light and matter exceeds the rates of all dissipative channels, the system enters the regime of strong light-matter coupling. In this regime, the photon and exciton states hybridise to form new quasiparticles known as exciton-polaritons. [3, 4]

Exciton-polaritons exhibit a mixed light-matter character, resulting in a set of unique physical properties that are distinct from those of either photons or excitons alone. Their low effective mass, inherited from the photonic component, [5] endows them with high mobility, while their matter component facilitates strong nonlinear interactions. [6, 7] This duality enables a range of novel physical phenomena, of particular interest is the ability of polaritons to undergo Bose-Einstein condensation (BEC), leading to macroscopic occupation of the ground state and the emergence of quantum coherence on a mesoscopic scale. [8, 9]

The formation and dynamics of exciton-polaritons have been extensively studied in inorganic semiconductor systems such as GaAs quantum wells, where low-temperature polariton condensation was first observed. [10] More recently, organic materials have emerged as promising candidates for achieving strong light-matter coupling at room temperature. Organic semiconductors offer several advantages: they exhibit large exciton binding energies, strong oscillator strengths, and well-defined vibronic features in their optical spectra. [3, 11, 12] These characteristics facilitate strong coupling in simple optical cavities, including planar Fabry-Pérot microcavities, and open new opportunities for device applications operating under ambient conditions.

Among organic semiconductors, molecules exhibiting strong vibronic coupling are of particular interest. Vibronic coupling, arising from the interaction between electronic and vibrational degrees of freedom, leads to the appearance of distinct vibrational progressions

in absorption and PL spectra. This spectral structure provides a relaxation pathway, which can play a crucial role in populating LP states and enabling polariton condensation. Notable examples of organic systems displaying strong coupling and polariton condensation include anthracene, perylene diimide (PDI), and other polycyclic aromatic hydrocarbons. [8, 13–16] In these systems, efficient LP population has been observed when the LP energy is resonant with the second vibronic peak of the PL spectrum, particularly at the cavity resonance condition corresponding to zero in-plane wavevector ($k_{||} = 0$).

Despite significant advances, several open questions remain regarding polariton relaxation mechanisms in organic systems. In particular, the dominant relaxation pathways responsible for populating the LP branch are not yet fully understood. Competing processes such as radiative pumping and vibrationally assisted scattering may both contribute. A detailed understanding of these processes is essential for controlling polariton condensation and optimising polariton-based devices.

Polariton-mediated energy transfer is another intriguing phenomenon emerging in the strong coupling regime. Unlike conventional Förster resonance energy transfer (FRET), which is limited to short distances due to the near-field nature of the dipole-dipole interaction, polariton-mediated energy transfer can span hundreds of nanometers. [17] This long-range transfer is enabled by the delocalized nature of polaritons and their ability to couple spatially separated donor and acceptor molecules within an optical cavity. While recent experimental and theoretical efforts have demonstrated the feasibility of this mechanism, a comprehensive understanding of the factors governing its efficiency, including donor-acceptor exciton energy offset, is still lacking.

This thesis addresses these fundamental questions using N-heteropolycyclic molecules, a class of organic semiconductors that exhibit high absorption coefficient (oscillator strength), strong photoluminescence and vibronic features, making them ideal candidates for strong coupling studies. The research presented here seeks to clarify the influence of material properties and cavity parameters on polariton formation, relaxation, and energy transfer efficiency.

The thesis follows a structured approach: beginning with essential theoretical and experimental background necessary to understand strong light-matter coupling in organic systems in **Chapter 2**. This chapter delves into strong light-matter coupling in planar microcavities, with a focus on organic semiconductors, particularly N-Heteropolycycles. It covers key topics such as microcavities, theoretical frameworks for strong light-matter coupling, material classes, and the photophysical properties of exciton-polariton states. **Chapter 3** outlines the materials and experimental methods used in this work, including material selection, device fabrication, and characterisation techniques, with a particular emphasis on angle-resolved spectroscopy. The chapter also discusses simulation methods used to model polariton dis-

persion and extract coupling parameters.

The subsequent chapters present the core experimental findings of this work. **Chapter 4** investigates strong light–matter coupling in planar microcavities incorporating novel peri-functionalized tetraazaperylene derivatives. The formation of exciton–polariton states is demonstrated through angle-resolved reflectance and photoluminescence measurements, and the extracted coupling strengths confirm the achievement of the strong coupling regime. **Chapter 5** examines polariton emission pathways in organic microcavities with TAC Trimer molecules. TAC trimer exhibits distinct vibronic progression in absorption and PL, enabling a systematic study of the effects of cavity detuning on RP and VAS pathways contributing to the population of LP states in such systems. **Chapter 6** explores the influence of donor-acceptor exciton energy offset on long-range energy transfer efficiency in spatially separated donor-acceptor multilayer cavities. Finally, **Chapter 7** concludes the thesis with a summary of results and outlines future research directions in this field.

2. Background

Strong light–matter coupling in planar microcavities leads to the formation of exciton-polaritons through the hybridisation of excitonic and photonic modes. The discussion is centred on N-Heteropolycyclic (NHP) molecules, which form the core material system investigated in this thesis. The chapter outlines the structure and optical properties of planar microcavities and the use of simulation techniques such as the transfer matrix method (TMM) to model their optical response. Theoretical models used to describe strong light-matter coupling are introduced, from quantum mechanical approaches like the Jaynes–Cummings and Tavis–Cummings models to the coupled harmonic oscillator (CHO) model, which is particularly useful for interpreting experimental data. Key photophysical consequences of polariton formation are introduced, including relaxation pathways and long-range energy transfer mechanisms.

2.1 Planar microcavities

Microcavities are optical resonators with dimensions comparable to the wavelength of light. [4] Planar microcavities are a specific type of microcavity consisting of two parallel reflective mirrors separated by a dielectric medium [18] as shown in Figure 2.1 (a). This configuration resembles the classic Fabry-Pérot interferometer [19,20], so they are also called Fabry-Pérot cavities. The reflective mirrors may consist of metallic films [12, 21–24] or dielectric stacks forming distributed Bragg reflectors (DBR) [25, 26]. The distance between these mirrors can be tuned to achieve cavity resonance, which allows a standing wave pattern (i.e cavity modes) to form (see Figure 2.1 (a)).

In a planar microcavity, two partially reflecting mirrors are separated by a distance L. Light is incident on the cavity at an angle θ relative to the surface normal. Upon entering the cavity, the light undergoes multiple reflections between the mirrors, experiencing a 180° phase shift at each metal boundary. This leads to interference between incident and reflected waves. [27] Constructive interference occurs when the path length of the round trip matches an integer multiple of the wavelength, resulting in an enhanced electric field inside the cavity. This condition is expressed mathematically as:

$$2\,n_{cav}L\cos(\theta_{int}) = m\,\lambda \quad \text{where} \quad (m = 1, 2, 3, ...) \tag{2.1}$$

where n_{cav} is the refractive index of the cavity medium, θ_{int} is the internal angle of incidence, or the angle at which light is reflected within the cavity, m is an integer, and λ is the wavelength of incident light. The internal angle (θ_{int}) is related to the external angle of incidence (θ) via Snell's law, expressed as: $\sin\theta_{int} = (n_{air}/n_{cav})\sin\theta$.

At normal incidence ($\theta_{int} = 0$), the resonance condition simplifies to $\lambda = 2\,n_{cav}\,L/m$. This shows that adjusting L allows control over the cavity mode. [28–30] The perpendicular wavevector component ($k_\perp$) of the total wavevector k (see Figure 2.1 (a)) at normal incidence satisfies the following condition:

$$k_\perp = \frac{m\,\pi}{n_{cav}\,L} \quad \text{where} \quad k_\perp = k\cos(\theta_{int}) \tag{2.2}$$

This quantisation of $k_\perp$ results in discrete cavity modes. Furthermore, the energy of these cavity modes (E_c) can be expressed as a function of the angle of incidence: [31]

$$E_c(\theta) = hc\,\frac{k}{2\pi} = hc\,\frac{m}{2\,n_{cav}\,L\cos(\theta_{int})} = E_0\left(1 - \frac{\sin^2(\theta)}{n_{cav}^2}\right)^{-\frac{1}{2}} \tag{2.3}$$

where E_0 is the cavity cut-off energy, leading to quasi-parabolic energy dispersion.

The discrete cavity modes confined within microcavities can be further distinguished by their polarisation, specifically into transverse magnetic (TM) and transverse electric (TE) modes. [32] The TE mode is characterised by an electric field oscillating perpendicular to the plane of incidence, effectively aligning parallel to the cavity plane.

Figure 2.1 (b) shows the electric field (E-field) distribution in a planar microcavity simulated using the TMM simulation, which will be explained in section 2.2. The simulation reveals a standing wave pattern within the cavity, characterised by alternating regions of high and low electric field intensity. At the metal mirrors, the boundary conditions for light reflection result in a near-zero optical field with limited penetration into the mirrors. This penetration follows an exponential decay of the electric field in the metal, given by $\propto \exp(-\alpha\,z)$, where the absorption coefficient is defined as $\alpha = 2\,\pi\,\epsilon_k/\lambda$. Here, z represents the depth into the metal along the direction perpendicular to the surface, and ϵ_k is the extinction coefficient of the metal mirror. [4]

An essential parameter for characterising an optical cavity is the quality factor, commonly referred to as the Q-factor. It is the ratio of stored energy to the energy lost during each optical cycle, multiplied by 2π. [33] To determine the Q-factor, one typically analyses the reflection spectrum of the cavity mode. It can be calculated by taking the ratio of the resonance energy (E_c) at the reflection peak to the full width half maxima (FWHM), denoted as ΔE_c. Additionally, the Q-factor can also be associated with the resonance frequency:

$$Q_c = \frac{E_c}{\Delta E_c} = \frac{\omega_c}{\Delta \omega_c} \tag{2.4}$$

A higher Q-factor corresponds to narrower cavity modes. In metal mirror microcavities, typical Q-factors range from 10 to 200, [12,34–37] as shown in Figure 2.1 (c). Furthermore, the Q-factor of the cavity is connected to the duration for which a photon remains trapped within the cavity (τ_c): $Q_c = \omega_c \tau_c$.

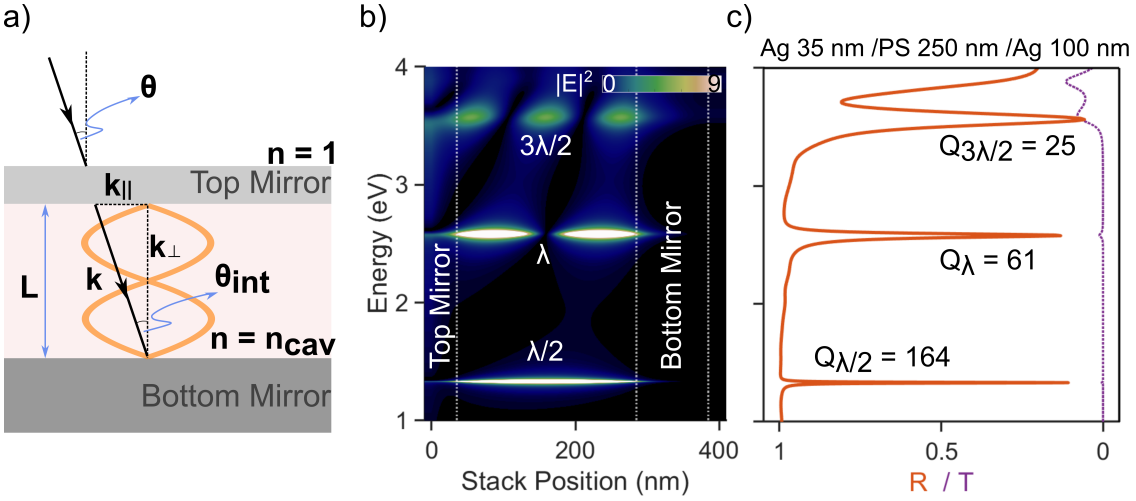

Figure 2.1. (a) Schematic of a planar microcavity with thickness L and refractive index n_{cav}. The cavity confines a λ (m = 2) optical mode. The wavevector k is depicted with its perpendicular and parallel components. The external viewing angle θ and internal angle θ_{int} are shown relative to the cavity normal. (b) Simulated electric field intensity distribution within a silver mirror cavity. Dashed lines indicate the semi-transparent top mirror and fully reflective bottom mirror positions. (c) Simulated reflection (R, solid orange line) and transmission (T, dashed purple line) spectra for a planar microcavity comprising a 250 nm polystyrene layer between silver mirrors. The Q factor of peaks corresponding to $\lambda/2$, λ and $3\lambda/2$ modes are indicated.

Another important parameter for characterising the optical cavity is the mode volume (V_m). Mode volume determines the efficiency of the cavity in concentrating the electromagnetic field in a restricted space. [38] A smaller mode volume leads to a higher electric field intensity, enhancing optical interactions such as absorption and emission processes. The enhancement of the electromagnetic field intensity inside an optical cavity is proportional to Q/V_m, meaning an ideal structure should have a high Q-factor and a small V_m. [39]

When evaluating metallic films and DBR as cavity mirrors, several key trade-offs must be considered, including reflectivity, light confinement, optical loss, and fabrication complexity. Metallic mirrors such as silver (Ag) offer high reflectivity in the visible spectrum and are relatively simple to fabricate. However, metal introduces absorption losses that re-

duce the Q-factor (< 200). [36] In contrast, DBRs can achieve higher reflectivity with lower absorption losses and Q-factor of several thousands [40, 41] but require precise multilayer fabrication processes. A key advantage of metallic cavities is smaller mode volumes due to stronger electromagnetic field confinement near the metal surface, compared to DBRs, with their distributed reflectivity profile, which often leads to larger mode volumes. [42] Another crucial factor in the performance of an optical cavity is the film roughness. The dielectric layer between the interface acts as a crucial interface between mirrors, and its smoothness directly affects the Q-factor and E-field intensity within the cavity. When the dielectric layer exhibits surface roughness, it leads to scattering losses, reducing reflectivity, introducing optical losses and resulting in a distorted spatial profile of resonant modes within the cavity. [43] Post-deposition treatments, like annealing or polishing, are often required to achieve sub-nanometer roughness levels suitable for high-performance cavities.

The mirror thickness also influences electric field confinement. While increasing thickness initially enhances confinement, it eventually reaches a saturation point. [44] Therefore, in many experimental designs, a thick bottom mirror and a thinner top mirror are used to enhance optical confinement while allowing the system to be easily probed optically through the top mirror. The bottom thick mirror improves reflectivity, while the thinner top mirror allows some light to pass through, enabling excitation of the cavity modes and the detection of reflected or emitted light.

2.2 Transfer matrix method simulation

The TMM is a powerful analytical tool for modelling linear propagation of electromagnetic waves through optical microcavities and other layered structures. [45, 46] The TMM simplifies the analysis of electromagnetic wave propagation in layered structures by modelling each layer as a uniform medium and using matrix operations to track how waves transmit and reflect at boundaries. It allows for the calculation of reflectivity, transmission, and field distribution within the cavity structure, making it valuable for designing microcavities with specific optical properties. [47–49]

The model structure as shown in Figure 2.2 (a) consists of N layers, each with a specific thickness L_j (where j ranges from 1 to N) and refractive index n_j, which may be complex. The structure is bounded by two semi-infinite regions: a substrate with refractive index n_0 on the bottom side, and an incidence medium with refractive index n_{N+1} on the top side.

Light enters the multilayer structure from the topmost layer at an incident angle θ, with a vacuum wavelength λ. It propagates through the stack as a plane harmonic wave in the positive z-direction. At each interface between layers with different optical properties, the incident wave splits into a transmitted wave (E_j^f) entering the next medium and a reflected

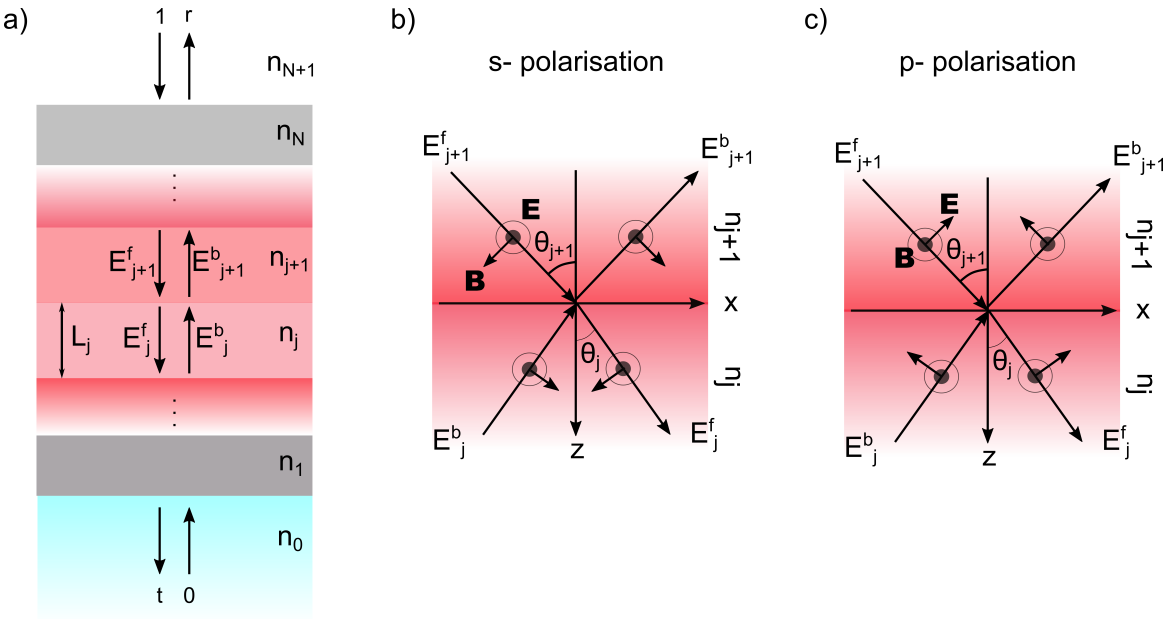

Figure 2.2. (a) Schematic representation of a general microcavity multilayer structure consisting of N layers on a substrate. The structure is positioned between a semi-infinite substrate and the incident medium. Each layer j has a thickness L_j. The optical electric fields at the interface between layers j and j+1 are indicated. Orientation of electromagnetic field and its propagation at the interface between layers j and j+1. for (b) s-polarised and (c) p-polarised light.

wave (E^b_j) returning to the previous medium. The electromagnetic field within each layer is characterised by the complex amplitudes of forward (E^f_j) and backward (E^b_j) propagating plane waves. [46]

$$E_j(z) = E^f_j\, e^{i\, k_{zj}\, L_j} + E^b_j\, e^{-i\, k_{zj}\, L_j} \tag{2.5}$$

$$B_j(z) = \frac{k_{zj}}{\omega}(E^f_j\, e^{i\, k_{zj}\, L_j} - E^b_j\, e^{-i\, k_{zj}\, L_j}) \tag{2.6}$$

where $k_{zj} = \frac{\omega\, n_j}{c}\, \cos\theta_j$ is the wavevector in layer j and $\omega = 2\,\pi\, c/\lambda$.

At the interface between layers j and j+1, the fields on the different layers can be related as follows: [50]

$$\begin{bmatrix} E^f_j \\ E^b_j \end{bmatrix} = T^{int}_j\, T^P_j \begin{bmatrix} E^f_{j+1} \\ E^b_{j+1} \end{bmatrix} \quad \text{with} \quad m = 1, 2, ..., N \tag{2.7}$$

where T^P_j is the interface matrix that describes the transmission (refraction) of light through interface j and j+1 in the structure, which can be written as: [50]

$$T^{int}_j = \frac{1}{t_{j,j+1}} \begin{bmatrix} 1 & r_{j,j+1} \\ r_{j,j+1} & 1 \end{bmatrix} \tag{2.8}$$

where $r_{j,j+1}$ and $t_{j,j+1}$ are the Fresnel complex reflection and transmission coefficients at interface j and j+1. These equations describe the behaviour of light at the interface between two layers with different refractive indices, as illustrated in Figure 2.2 (b) and (c). These coefficients are defined for s-polarised (TE wave) and p-polarised (TM wave) light and can be expressed as follows: [50]

$$\begin{aligned} t_{j,j+1} &= \frac{2\,n_{j+1}}{n_{j+1}\cos(\theta_{j+1}) + n_j\cos(\theta_j)}, \\ r_{j,j+1} &= \frac{n_{j+1}\cos(\theta_{j+1}) - n_j\cos(\theta_j)}{n_{j+1}\cos(\theta_{j+1}) + n_j\cos(\theta_j)} \end{aligned} \quad \text{TE wave} \tag{2.9}$$

$$\begin{aligned} t_{j,j+1} &= \frac{2\,n_j\,n_{j+1}^2\cos(\theta_{j+1})}{n_j^2\,n_{j+1}\cos(\theta_{j+1}) + n_{j+1}^2\,n_j\cos(\theta_j)}, \\ r_{j,j+1} &= \frac{n_j^2\,n_{j+1}\cos(\theta_{j+1}) - n_{j+1}^2\,n_j\cos(\theta_j)}{n_j^2\,n_{j+1}\cos(\theta_{j+1}) + n_{j+1}^2\,n_j\cos(\theta_j)} \end{aligned} \quad \text{TM wave} \tag{2.10}$$

and T_j^P is the propagation matrix, which can be written as :

$$T_j^P = \begin{bmatrix} e^{-i\,k_{zj}\,L_j} & 0 \\ 0 & e^{i\,k_{zj}\,L_j} \end{bmatrix} \tag{2.11}$$

In the same way as equation 2.7, by using the interface matrix of equation 2.8 and the propagation matrix of equation 2.11 the total system transfer matrix T^ML which relates the electric field in the incident medium and the substrate side by:

$$\begin{bmatrix} E_{N+1}^f \\ E_{N+1}^b \end{bmatrix} = T_N^{int}\,T_N^P\,T_{N-1}^{int}\,T_{N-1}^P\,....\,T_1^{int}\,T_1^P\,T_0^{int}\,T_0^P \begin{bmatrix} E_0^f \\ E_0^b \end{bmatrix} = T^S \begin{bmatrix} E_0^f \\ E_0^b \end{bmatrix} \tag{2.12}$$

The matrix T^S describes the response of the whole multilayer structure, and from it, the total transmission and reflection amplitudes t and r can be calculated by substituting an incidence field amplitude of 1 into equation 2.12 :

$$\begin{bmatrix} 1 \\ r \end{bmatrix} = \begin{bmatrix} T_{11}^S & T_{12}^S \\ T_{21}^S & T_{22}^S \end{bmatrix} \begin{bmatrix} 0 \\ t \end{bmatrix} \tag{2.13}$$

which yields

$$t = \frac{1}{T_{11}^S}, \quad r = \frac{T_{21}^S}{T_{11}^S} \tag{2.14}$$

The transmission and reflection coefficients are given by: $T = |t|^2$ and $R = |r|^2$. If scattering is negligible, the absorption A can be calculated directly by:

$$A = 1 - R - T \tag{2.15}$$

The TMM scheme has been widely applied in recent studies of optical cavities, including polaritonic systems. [25,51,52] Figure 2.3 shows TMM simulation results for a microcavity composed of Ag (35 nm)/Active layer (438 nm)/Ag (100 nm), under uncoupled (Figure 2.3 (a,b)) and strongly coupled (Figure 2.3 (c,d)) conditions. In this example, the active layer is modelled using a Lorentzian function with a peak at 1.89 eV, representing an excitonic transition in the material. Typically, the absorption spectrum of the active material is used to extract the complex refractive index via Kramers–Kronig relations, which is then used to simulate the optical response. [53, 54]

Figure 2.3 (a) shows the simulated angle-resolved reflectivity spectra for the uncoupled system, where only the photonic mode is observed. The cavity energy E_c and exciton energy E_x are marked to show the positions of the bare cavity mode and exciton transition, respectively. These energies resonate at an angle of 55°. Figure 2.3 (b) presents the reflectance spectrum at 55° incidence for the uncoupled system, revealing a single Lorentzian-shaped dip centred at the resonance between the cavity and exciton energies. Figure 2.3 (c) shows the TMM simulated dispersion spectra under strong light-matter coupling conditions. At resonance, the cavity mode and exciton transition interact, and instead of crossing each other (as they would in the absence of coupling), they exhibit anticrossing behaviour, as shown in the dispersion spectra. This anticrossing indicates the hybridisation of the cavity mode and exciton transition, resulting in the formation of two distinct energy branches, known as the polariton states. Figure 2.3 (d) shows the corresponding reflection spectra at the resonance angle of 55°. Instead of a single Lorentzian peak, as seen in the uncoupled system, two equal-intensity peaks are observed at this angle. One appears at a higher energy than the resonance energy, corresponding to the upper polariton (UP), and the other at a lower energy, corresponding to the LP. The energy separation between these two states is denoted as 2V, where V is the coupling strength between the exciton and the cavity mode.

The TMM can also be used to predict the electric field intensity (E-Field) within a multilayer stack (see Figure 2.1 (b)), with the relevant equations provided by Pettersson et al. [55]. In real samples, however, interlayer roughness is often present and cannot be neglected. As a first approximation, this roughness can be incorporated through scalar scattering, where the Fresnel coefficients are modified using a roughness coefficient (σ), as described by Yin et al. [56]. When the layers are sufficiently homogeneous, meaning intralayer scattering is minimal, this adapted TMM approach provides a reasonable match to experimental transmission and reflectivity spectra. As demonstrated in this section, a modified version of a TMM code originally developed by T. Chervy [57] is employed throughout this thesis to simulate the reflectivity and field distribution in microcavity systems exhibiting strong light-matter coupling.

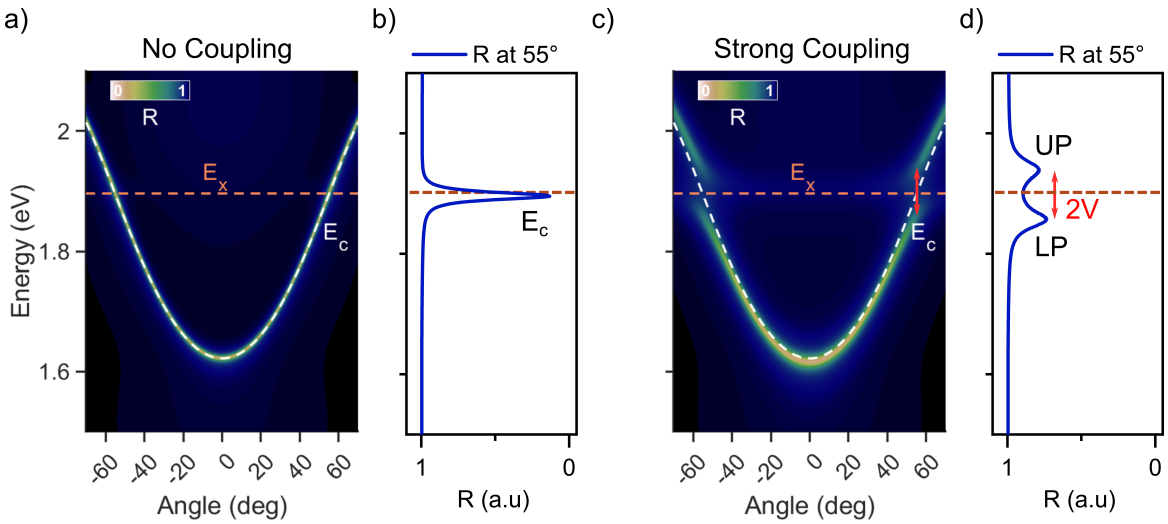

Figure 2.3. TMM simulations comparing optical responses with and without strong coupling. (a) Angular dispersion of the uncoupled system, showing a single photonic mode. The cavity energy E_c and exciton energy E_x are marked. (b) The corresponding reflectance spectrum at 55° incidence for the uncoupled system shows a single Lorentzian peak at the cavity resonance. (c) Angular dispersion under strong coupling conditions, with the characteristic anticrossing at resonance between the cavity mode and exciton energy. The cavity energy E_c and exciton energy E_x are marked. (d) Reflectance at 55° for the strongly coupled system, showing two Lorentzian peaks corresponding to the UP and LP, separated by an energy gap 2V, where V is the coupling strength between the cavity mode and the exciton.

2.3 Fundamentals of strong light-matter coupling

With the microcavity structure established, the next step is to understand how light interacts with active emitters placed inside such cavities. When a confined cavity mode interacts with molecules such as the organic emitters studied in this thesis, the system can exhibit either weak or strong light–matter coupling, depending on how the interaction strength compares to the relevant loss mechanisms. In the weak coupling regime, the cavity modifies the rate of spontaneous emission of the emitters through the Purcell effect. [58] In the strong coupling regime, the energy exchange between the cavity mode and molecular excitations becomes faster than the combined losses from non-radiative decay and photon leakage. This results in the formation of new eigenstates called exciton-polaritons, which are hybrid light-matter states. [59] These states are characterised by a measurable energy splitting, known as Rabi splitting, which appears in reflectance or transmittance spectra.

Theoretical descriptions of the strong coupling regime include classical, semiclassical, and fully quantum mechanical approaches. [60] A simple and intuitive classical analogy is the model of two coupled harmonic oscillators exchanging energy, similar to a pair of

coupled pendulums. [61] A more accurate description of strong light–matter interaction is formulated quantum mechanically, using models such as the Jaynes–Cummings and Tavis–Cummings models, which provide a framework for describing how a single emitter or an ensemble of emitters interacts with a cavity mode. Meanwhile, the CHO model is frequently used to fit experimental spectra and extract key parameters like coupling strength and detuning.

2.3.1 Quantum models for light-matter coupling

At the quantum level, light–matter interactions are described by models that account for coupling between electronic transitions in molecules and quantised electromagnetic modes within a cavity. The simplest system in which light–matter coupling can be studied is a single two-level emitter coupled to a single mode of a quantised electromagnetic field inside a cavity. The physics of this system is described by the Jaynes-Cummings (JC) model, which treats both light and matter quantum mechanically. [62, 63]

The exciton is approximated as a two-level quantum system. The two states are the ground state $|g\rangle$, where no exciton is present, and the excited state $|e\rangle$, where an exciton is formed. The energy difference between $|g\rangle$ and $|e\rangle$ corresponds to the exciton transition energy, E_x. The quantised cavity mode is modelled as a harmonic oscillator. The cavity mode is described by Fock states $|n\rangle$, where n = 0, 1, 2, ... represents the number of photons in the cavity. The ground state is $|0\rangle$ (no photons), and excited states correspond to increasing photon numbers. The cavity photon has a resonance energy E_c. The states $|e, 0\rangle$ and $|g, 1\rangle$ represent product states in which the emitter is excited and the cavity contains no photon, or the emitter is in the ground state and the cavity contains one photon, respectively. These two uncoupled states hybridise to form the UP and LP states in the strong coupling regime as illustrated in Figure 2.4.

Under the rotating wave approximation (RWA), [64] which neglects non-energy-conserving terms (i.e., those oscillating rapidly compared to the system timescales), the JC Hamiltonian becomes: [63, 65, 66]

$$H_{JC} = \frac{1}{2}E_x\,\hat{\sigma_z} + E_c\,\hat{a^\dagger}\,\hat{a} + \hbar V_1(\hat{a^\dagger}\,\hat{\sigma_-} + \hat{a}\,\hat{\sigma_+}) \tag{2.16}$$

Here, $\hat{\sigma_z}$, $\hat{\sigma_+}$ and $\hat{\sigma_-}$ are inversion, raising and lowering operators for the two-level emitter respectively, $\hat{a^\dagger}$ and $\hat{a}$ are photon creation and annihilation operators, E_x and E_c are the transition energies of the emitter and the cavity mode respectively, and V_1 is the coupling strength between a single atom and photon, which is assumed to be real and positive.

When the cavity and emitter are in resonance ($E_x = E_c$), the energies of the hybrid eigenstates are given by:

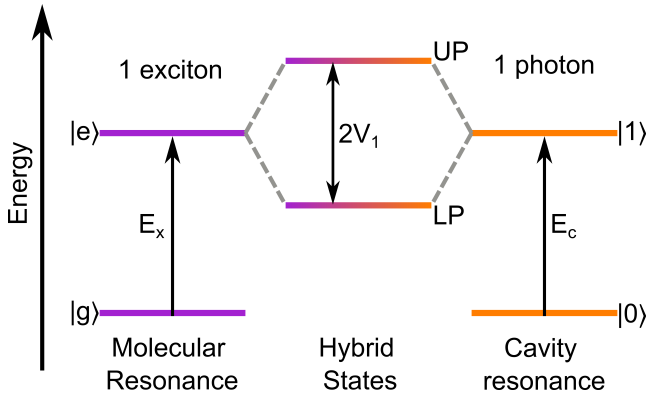

Figure 2.4. Schematic representation of a single two-level emitter with transition energy E_x and a single cavity mode with resonance energy E_c hybridize to form two new eigenstates: the UP and LP, separated by an energy gap $2V_1$. The original uncoupled states $|e, 0\rangle$ (one exciton, no photon) and $|g, 1\rangle$ (ground state with one photon) are mixed to form these hybrid light-matter states under strong coupling conditions.

$$E_{JC} = E_c - \frac{1}{2}\left(\Delta \pm \sqrt{(2V_1)^2 + (\Delta)^2}\right) \tag{2.17}$$

where $\Delta = E_c - E_e$ represents the detuning between the cavity and the atom. For $\Delta = 0$, this leads to the vacuum Rabi splitting of the resonance into two distinct states separated by $2V_1$. The corresponding eigenstates are coherent superpositions of the bare states $|e, 0\rangle$ and $|g, 1\rangle$.

To place the JC model in an experimental context, one may consider the micromaser. [67] In an experimental emitter-cavity system, two loss channels are typically considered: the spontaneous emission rate of the emitter into free-space modes, γ_e, and the cavity decay rate, γ_c. These loss rates can be taken into account by introducing a complex atom and cavity resonance energy $E_x{}^* = (E_x - i\hbar\gamma_e)$ and $E_c{}^* = (E_c - i\hbar\gamma_c)$, respectively. [68] The resulting Hamiltonian, which now includes loss rates, is given by

$$H^*_{JC} = \frac{1}{2} E_x{}^* \hat{\sigma_z} + E_c{}^* \hat{a^\dagger}\,\hat{a} + \hbar V_1 (\hat{a^\dagger}\,\hat{\sigma^-} + \hat{a}\,\hat{\sigma^+}) \tag{2.18}$$

While the JC model applies to a single emitter, most experimental systems, particularly those involving organic materials, contain ensembles of emitters interacting simultaneously with the cavity field. In this case, the interaction becomes collective, and the system is more accurately described by the Tavis-Cummings (TC) model, which captures the enhanced coupling arising from coherent interactions among multiple emitters. The TC model describes a collective interaction between N identical two-level emitters and a single cavity mode. [68, 69] Here, the focus lies on a unique set of molecular states where all molecules act together as one unit, the Dicke states. [70,71] The analysis considers the single-excitation

manifold, where only one excitation exists in the system, either in the cavity or in the emitter ensemble. Under these conditions, the behaviour of the entire group of molecules can be described using the collective inversion, raising and lowering operators of the molecular group as a whole:

$$S_z = \frac{1}{\sqrt{N}} \sum_{n=1}^{N} \hat{\sigma}_z^{(n)}, \quad S_+ = \frac{1}{N} \sum_{n=1}^{N} \hat{\sigma}_+^{(n)}, \quad S_- = \frac{1}{\sqrt{N}} \sum_{n=1}^{N} \hat{\sigma}_-^{(n)} \tag{2.19}$$

The TC Hamiltonian is then written as:

$$H_{TC} = \frac{1}{2} E_x \hat{S_z} + E_c \hat{a^\dagger} \hat{a} + \hbar V(\hat{a^\dagger} \hat{S_-} + \hat{a} \hat{S_+}) \tag{2.20}$$

The N-emitter and cavity mode interaction resembles that of an atom-cavity interaction. Thus, the N-emitters act collectively as a single effective quantum system with a collective coupling strength of $V = \sqrt{N} V_1$. The $\sqrt{N}$-scaling arises because the dipole moments of the N emitters add coherently in the cavity mode, increasing the effective coupling strength. This collective enhancement is a key result of the TC model and is experimentally observed in organic microcavities with high molecular densities. [11,72] Each emitter can have different coupling strengths, $V_{1,n}$, due to spatial variations in the cavity field, but the TC Hamiltonian equation 2.20 remains applicable for defining the collective coupling strength as:

$$V = (\sum_{n=1}^{N} {V_{1,n}}^2)^{\frac{1}{2}} = \sqrt{N} V_1^* \tag{2.21}$$

where $V_1^* = \left(\frac{1}{N} \sum_{n=1}^{N} V_{1,n}^2\right)^{\frac{1}{2}}$ refers to the root mean square of the individual coupling strengths of each single emitter. This formulation generalises the standard case of identical emitters to systems with spatially inhomogeneous coupling, particularly relevant for organic molecules in planar microcavities, where each emitter experiences a different electric field amplitude depending on its position within the cavity mode profile.

The TC model assumes that all relevant rates and frequencies are smaller than the free spectral range ν_{FSR} of the resonator. The ν_{FSR} is another key property of an optical cavity, representing the frequency spacing between two adjacent resonant modes of the system. However, as the number of emitters, N, increases, two quantities may violate this condition: the collective coupling strength, V, and the emitter-induced photon loss rate of the system, V^2/γ_c. Both these quantities must remain smaller than ν_{FSR} for the TC Hamiltonian to remain valid. [68]

$$\nu_{FSR} >> V \tag{2.22}$$

$$\nu_{\mathrm{FSR}} >> \frac{\mathrm{V}^2}{\gamma_{\mathrm{c}}} \tag{2.23}$$

When the collective coupling strength exceeds the free spectral range of the resonator, the system enters the superstrong coupling regime, which has been realised in specially engineered systems. [73, 74]

2.3.2 The coupled harmonic oscillator approach for modelling exciton-polaritons

The coupled harmonic oscillator (CHO) model is a widely adopted framework for analysing hybrid light–matter states and extracting key parameters from experimental data. [75, 76] In its simplest form, the model considers an exciton as a two-level system with a ground state ($|\mathrm{g}\rangle$) and an excited state ($|\mathrm{e}\rangle$), while the cavity mode is treated as a quantised electromagnetic field capable of containing multiple photons. The interaction between the exciton and the cavity photon is described within the single-excitation manifold, where only one quantum of excitation exists in the system—either an excited exciton or a single photon, but not both simultaneously. Under these conditions, the system is captured using a 2×2 Hamiltonian, which yields two hybrid eigenstates corresponding to the UP and LP branches.

While the 2×2 model accurately describes systems with a single excitonic resonance coupled to a single cavity mode, more complex systems involving two distinct excitonic modes, either from different molecular species (e.g., donor and acceptor) or from vibronic sub-bands of the same molecule, [77, 78] can also be treated within an extended CHO framework. In such cases, the system is represented by a 3×3 Hamiltonian, enabling the modelling of the interaction of both exciton modes with the cavity photon. These multilevel coupling scenarios are discussed in detail in Section 2.7.1. For now, this section focuses on the conventional 2×2 case, which forms the foundation for understanding polariton dispersion and composition in single-mode exciton–cavity systems.

Within single-excitation manifold, the single-mode exciton–cavity system reduces to two basis states: $|\mathrm{g}, 1\rangle$, where the exciton is in the ground state and the cavity contains one photon, and $|\mathrm{e}, 0\rangle$, where the exciton is excited and the cavity is empty. Any quantum state of the system under this approximation can be described as a superposition of these two states:

$$|\psi\rangle = \alpha\ |e, 0\rangle + \beta\ |g, 1\rangle \tag{2.24}$$

where α and β describe how much of each component (photon-like or exciton-like) contributes to the hybrid state and are known as Hopfield coefficients. The system is described by the following matrix equation:

$$H\psi = E\psi \tag{2.25}$$

with the Hamiltonian given by:

$$\begin{bmatrix} E_c & V \\ V & E_x \end{bmatrix} \begin{bmatrix} \alpha \\ \beta \end{bmatrix} = E \begin{bmatrix} \alpha \\ \beta \end{bmatrix} \tag{2.26}$$

Here, E_c is the energy of the cavity photon, and E_x is the energy of the exciton. The off-diagonal terms, V, represent the coupling strength between the exciton and photon. This matrix describes the interaction between a cavity photon and molecular excitons. Diagonal elements describe the energies of the uncoupled systems, whereas the off-diagonal elements account for their mutual interaction, which results in the formation of new hybrid states known as exciton–polaritons.

Solving the matrix equation yields the eigenvalues and eigenvectors of the system. The eigenvalues correspond to the energies of the UP and LP branches, given by:

$$E_{UP,LP} = \frac{E_x + E_c}{2} \pm \frac{1}{2}\sqrt{(E_x - E_c)^2 + (2V)^2} \tag{2.27}$$

where $2V = \hbar\Omega$ defines the Rabi splitting at zero detuning. The square root term includes both the detuning (energy difference between the exciton and photon) and the coupling strength. The ± signs indicate two distinct solutions, reflecting the splitting of energy levels due to the strong interaction.

The corresponding eigenvectors describe the polariton states as mixtures of photon and exciton components. These compositions depend on the detuning and coupling strength, and can be quantified through the Hopfield coefficients α and β. At zero detuning ($E_c = E_x$), the mixing is maximal, resulting in polaritons that are equal parts exciton and equal parts photon. As the detuning increases, LP becomes more photon-like while the UP becomes more exciton-like.

The Rabi splitting ($\hbar\Omega$) is a direct measure of the coupling strength (V), observable as the energy gap between the UP and LP branches at zero detuning. It serves as a clear signature of strong coupling, distinguishing hybridised states from independent excitons and photons. The coupling strength V, and therefore the Rabi splitting, depends on several physical parameters. It scales with the exciton dipole moment d, which governs how strongly the exciton interacts with the cavity electric field. The electric field amplitude is inversely proportional to the square root of the cavity mode volume V_m, so smaller mode volumes enhance the interaction. Additionally, the coupling strength increases with the square root of the photon number n_{ph}. The relationship between the Rabi splitting and these parameters is given by: [79]

$$\hbar\Omega = 2\,V = 2\,d\,\sqrt{n_{ph}+1}\,\sqrt{\frac{E_c}{2\,\epsilon_0 V_m}} \tag{2.28}$$

This expression highlights how cavity design and material properties together influence the light–matter interaction strength. A large dipole moment and a small mode volume are crucial for reaching the strong coupling regime.

Strong coupling between an exciton and a cavity photon arises when the rate of coherent energy exchange between the two exceeds their respective loss rates. This regime is achieved when the coupling strength V is greater than one-quarter of the sum of the exciton and cavity photon linewidths (FWHM): [80]

$$V > \frac{FWHM_e + FWHM_c}{4} \tag{2.29}$$

When this criterion is satisfied, the system enters the strong coupling regime, characterised by the formation of hybrid light–matter states known as exciton-polaritons. Conversely, if the coupling strength is too low or the loss rates are too high, the system remains in the weak coupling regime, where exciton and photon modes do not form hybrid states.

2.3.3 Properties of microcavity exciton-polariton states

Exciton–polaritons are hybrid light-matter quasiparticles that exhibit properties of both their constituent components. These states possess a very small effective mass inherited from their photonic component, due to the massless nature of photons. [5] This photon component allows direct interaction with light, facilitating optical probing. From their excitonic component, polaritons inherit the ability to interact with molecular vibrations via vibronic interactions, [81, 82] enables interactions with other quasiparticles such as phonons or excitons, contribute to nonlinear optical behaviour, [6, 7, 83] and access phonon-assisted relaxation channels [84]. The exciton transition energy, linewidth, and absorption strength also determine the coupling strength and spectral characteristics of polariton states.

Polaritons also inherit the angle-dependent behaviour of their photonic component, a consequence of the in-plane wavevector dependence of the cavity mode energy (see equation 2.3). While dispersions are conventionally represented as energy versus in-plane momentum using $|k_{||}| = \frac{2\pi}{\lambda}\sin\theta$ where θ is the incident angle and λ is the peak wavelength. This thesis adopts an energy versus incident angle representation. The dispersion diagram in Figure 2.5 (b) shows the LP and UP branches as functions of angle θ, revealing an avoided crossing at the intersection of the non-dispersive exciton energy (E_x) and the dispersive cavity energy (E_c). The minimal energy gap at the avoided crossing corresponds to the Rabi splitting or coupling strength 2V, a direct measure of the interaction strength between light and matter.

The detuning, defined as $\Delta = E_c(0°) - E_x$, quantifies the energy difference between the cavity mode energy and exciton energy at normal incidence and controls the relative photonic and excitonic contributions to each polariton branch. The parameters 2V and Δ, introduced theoretically in Section 2.3.1, are directly extracted from the experimental dispersion and play a crucial role in characterising and manipulating polariton states.

The fundamental configuration used to achieve such strong coupling is illustrated in Figure 2.5 (a), which shows a λ-cavity formed by two reflective silver mirrors enclosing an ensemble of N two-level molecular emitters. In organic microcavities, strong coupling involves a large number of molecular emitters, typically, on the order of $N \approx 10^5$ molecules interacting coherently with a single cavity mode. This collective interaction leads to a significant enhancement of the coupling strength due to the in-phase coupling of all molecular dipoles to the same photonic mode. [79] According to the Tavis–Cummings model, the collective coupling strength scales as $V = V_1\sqrt{N}$, where V_1 is the coupling strength for a single emitter. The resulting polaritonic system consists of N+1 collective states: two detectable bright polariton states and N-1 collective dark states where transitions from ground states are forbidden, as illustrated in Figure 2.5 (c). [85] These dark states, along with high

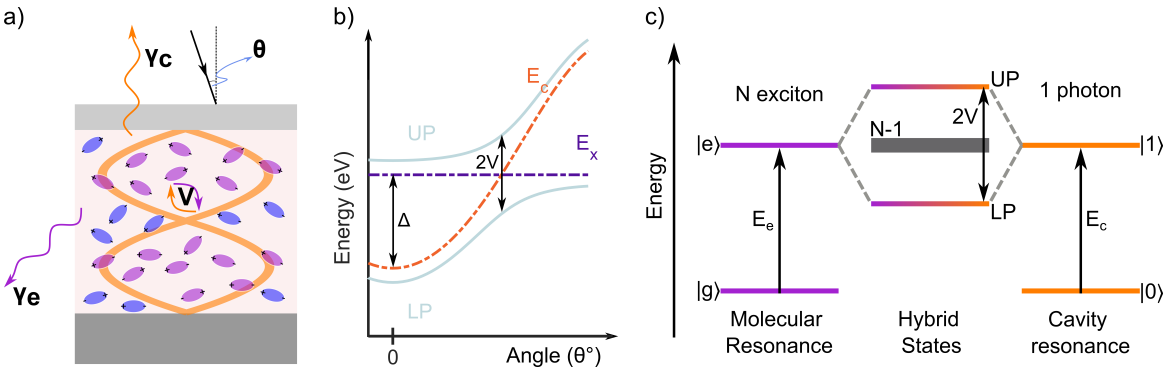

Figure 2.5. (a) Schematic diagram of a λ-cavity mode formed between two highly reflective silver mirrors. The cavity contains N two-level active emitters resonant with the cavity mode. Key parameters are indicated: light-matter coupling strength V, cavity decay rate γ_c, and spontaneous emission rate γ_e from the emitter to free space. (b) Dispersion diagram showing the UP and LP branches formed via strong coupling between a cavity photon mode (E_c, dashed orange line) and a molecular exciton transition (E_x, dashed violet line). The energy separation between the polariton branches defined by the coupling strength 2V and the detuning $\Delta = E_c(0°) - E_x$ determines that the exciton–photon admixture at normal incidence is indicated. (c) Energy-level diagram illustrating the formation of hybrid polariton states from a single cavity photon state $|1\rangle$ and an ensemble of N molecular excitons. The coupling produces two bright polariton states (UP and LP) and an $(N-1)$-fold degenerate manifold of dark states that do not couple to light.

momentum and uncoupled states, form the exciton reservoir, which exhibits properties of weakly coupled emitters. In the linear regime, the bright state population is about 10^{-7} times smaller than the exciton reservoir population, highlighting the importance of exciton reservoir-mediated processes. Experimentally, the collective nature of strong coupling is confirmed by the observed dependence of coupling strength on molecular concentration (c), with $V \propto \sqrt{N/V} = \sqrt{c}$ consistent with the $\sqrt{N}$ scaling. [79]

Figure 2.6 presents simulations illustrating how varying the coupling strength V influences both the polariton dispersion and the Hopfield coefficients, which quantify the photonic and excitonic content of the polariton states. The left panels in Figure 2.6 (a) and (b) display the dispersion plots for two different coupling strengths: V = 40 meV and V = 80 meV, respectively. As the coupling strength increases, the mode splitting between the LP and UP branches becomes more pronounced, with the polariton bands (shown in light blue) diverging further from the uncoupled exciton and photon modes. The right panels of Figure 2.6 (a) and (b) show the corresponding Hopfield coefficients, which describe the excitonic (orange) and photonic (black) content of the polariton states. With stronger coupling, the hybridisation between light and matter becomes more extensive across a broader angular range, as evidenced by the increased mixing of exciton and photon components. While the CHO model used here does not explicitly include the emitter concentration c, the coupling strength V is directly influenced by it through the collective interaction of molecular excitons with the cavity field, as discussed earlier in this section. Therefore, these simulations imply that experimentally increasing the molecular concentration enhances the coupling strength, resulting in larger Rabi splitting, consistent with the trends observed in Figure 2.6.

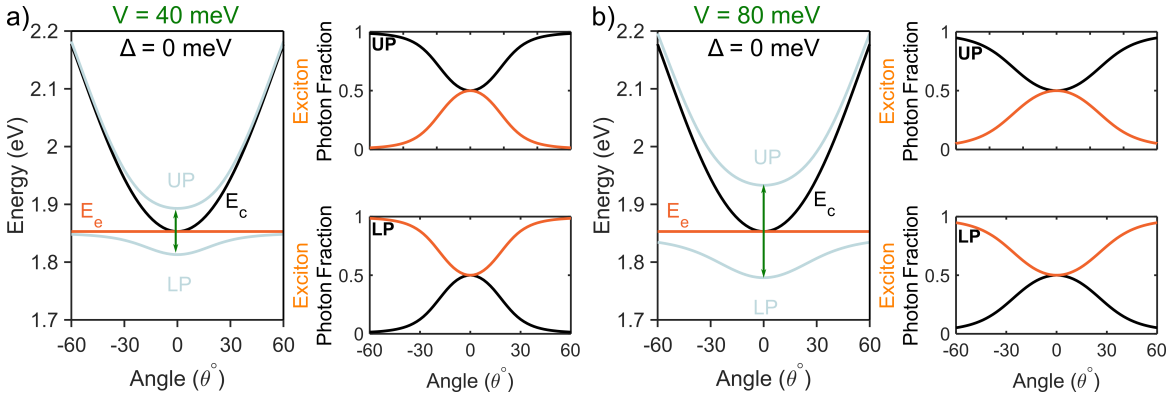

Figure 2.6. Dispersion plot (left) and Hopfield coefficients (right) for UP and LP (light blue) at different coupling strengths: (a) V = 40 meV and (b) V = 80 meV. The exciton (orange) and photon (black) fractions are calculated using the coupled oscillator model, maintaining a constant detuning of zero.

The resonant energy of the cavity mode can be tuned by adjusting the cavity length L, introducing detuning Δ between the photon and exciton energies. This detuning defines three

key regimes: This detuning defines three key regimes: zero detuning ($E_c = E_x$), positive detuning ($E_c > E_x$), and negative detuning ($E_c < E_x$). Figure 2.7 shows the effect of detuning on polariton dispersion and composition. Under positive detuning (Figure 2.7 (a)), the LP branch exhibits more exciton-like character, while the UP branch shows more photon-like behaviour. Conversely, under negative detuning (Figure 2.7 (b)), the LP branch becomes predominantly photonic in nature, and the UP branch displays more excitonic character at small angles of incidence. These results emphasise that cavity detuning, readily controlled by fabrication parameters such as spacer layer or active thickness, provides a versatile handle for tuning polariton properties.

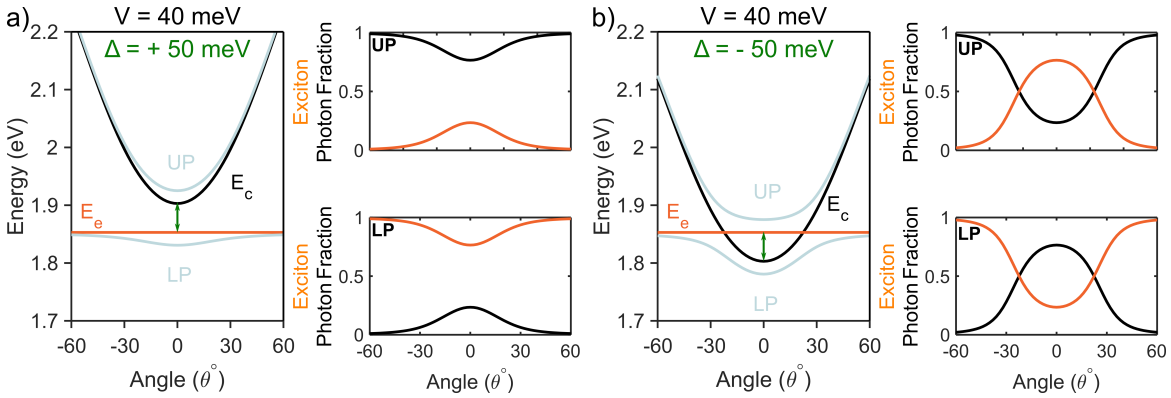

Figure 2.7. Dispersion plot (left) and Hopfield coefficients (right) for UP and LP (light blue) at different coupling strengths: (a) Δ = -50 meV and (b) Δ = +50 meV. The exciton (orange) and photon (black) fractions are calculated using the coupled oscillator model, maintaining constant coupling strength (V).

Finally, the spatial distribution of the vacuum field within the cavity strongly influences the coupling strength. As described by Equation 2.28, the coupling strength exhibits a strong dependence on the field strength E_0. The vacuum field varies within the cavity, reaching its minimum at nodes and maximum at antinodes. The coupling strength directly follows this field strength pattern, resulting in maximised Rabi splitting when molecules are concentrated near antinodes. [86–88] The relative orientation of molecular transition dipole moments d along with E_0 also affects coupling strength. In a Fabry-Pérot cavity, maximum interactions occur in the cavity plane (parallel to the mirrors), while molecules with transition dipole moments perpendicular to this plane do not couple effectively. [11, 89] Consequently, in samples with random molecular orientations and varying electric fields, the measured coupling strength V represents an average value. This spatial and orientational dependence has important implications for device design and data interpretation: placing molecules at antinodes and aligning dipoles with the cavity field can enhance coupling, while neglecting these factors may lead to underestimation of the true interaction strength or misinterpretation of spectra. [86, 87]

2.4 Excitonic materials for strong light–matter coupling

Strong coupling was first observed in microcavities containing Rydberg atoms in the microwave range, aligning with JC model predictions. [90] In 1992, Weisbuch et al. demonstrated strong coupling in a GaAs quantum well microcavity flanked by GaAlAs-AlAs distributed Bragg reflectors, observing cavity exciton-polaritons at cryogenic temperatures. Reflectivity measurements showed clear anticrossing behaviour between exciton and photon modes, with a Rabi splitting of approximately 3.4 meV at resonance, confirming the formation of exciton–polariton states at cryogenic temperatures. [91] This early work established the suitability of inorganic semiconductors for achieving strong coupling. This system relied on Wannier–Mott excitons, which are delocalised electron–hole pairs with binding energies in the range of 5–50 meV, low oscillator strengths, and transition linewidths at cryogenic temperatures. [92] However, the low binding energy of these excitons makes them thermally unstable at room temperature, where $k_BT \approx 26$meV, often necessitating cryogenic operation. Moreover, the resulting Rabi splittings (≈10 meV) are comparable to or smaller than thermal broadening, complicating the resolution of polariton modes at room temperatures. [75, 80, 93]

To overcome these limitations, strong coupling in inorganic systems typically relies on a combination of low-temperature environments to preserve exciton coherence, high-quality-factor cavities to minimise photonic losses, and quantum well architectures that enhance oscillator strength and spatial confinement. These strategies have led to the development of strong coupling platforms based on III–V GaAs-based semiconductors, [91, 94] II–VI materials such as ZnSe and CdTe, [95, 96] and wide-bandgap semiconductors like III–V nitrides and ZnO, which offer larger exciton binding energies and enable room-temperature operation [97–103]. However, the fabrication of such cavities relies on epitaxial techniques, which are complex and resource-intensive.

Organic materials present an alternative that overcomes some of these constraints. The first demonstration of strong coupling in an organic emitter was reported by Lidzey et al. in 1998, using tetra-(2,6-t-butyl)phenol-porphyrin zinc (4TBPPZn), a porphyrin derivative with a narrow Soret band. [3] Despite a low cavity Q-factor, a large Rabi splitting of 160 meV allowed clear observation of mode anticrossing in reflectance at room temperature. Porphyrins were initially selected for their rigid planar structure that minimises vibronic coupling and their significant oscillator strengths ($\approx 105\text{cm}^{-1}$). Subsequent studies used J-aggregated cyanine dyes, which offered even higher oscillator strengths ($\approx 106\text{cm}^{-1}$) and much narrower linewidths. [11] It was demonstrated that placing cyanine J-aggregates within a metallic microcavity resulted in a 300 meV Rabi splitting. [12] This splitting surpassed that observed in a microcavity confined by DBR mirrors, attributed to the greater electromagnetic

field magnitude in the smaller mode volume of a fully metallic microcavity. A challenge with these materials is achieving uniform J-aggregation, particularly at high dye volume in an inert matrix, as disruption of aggregates leads to a return to vibronic progression-dominated and inhomogeneously broadened optical spectra typical of organic materials. [104]

Strong coupling has also been demonstrated in other organic materials, including small molecules such as thermally evaporated small molecules like 1,4,5,8- naphthalenetetracarboxylic dianhydride (NTCDA) [77], as well as rigid-backbone polymers such as σ-conjugated polysilane [105] and the ladder-type conjugated polymer methyl-substituted ladder-type poly(p-phenylene) (MeLPPP). [8] These materials were selected due to their narrow absorption line widths, minimal Stokes shifts, and high photoluminescence quantum yield (PLQY), which facilitated progress in organic polariton research, notably the observation of organic polariton condensation at ambient temperature. [8, 14] Conversely, other studies successfully demonstrated strong light-matter coupling with organic materials like switchable spiropyran/merocyanine system, [106] perylene diimide derivatives, [107] and the small-molecule 2,7-bis[9,9-di(4-methylphenyl)-fluoren-2-yl]-9,9-di(4-methylphenyl)fluorine (TADF) [108] with relatively broad absorption spectra spanning several hundred meV.

Organic emitters support Frenkel excitons, which are spatially localised electron–hole pairs with binding energies in the range of 0.5–1.0 eV. [92, 109, 110] These large binding energies far exceed thermal energies at room temperature. Organic molecules also exhibit large oscillator strengths and transition dipole moments, [111], which enhance light–matter interaction strength and allow strong coupling to be achieved even in microcavities with relatively low quality factors, such as metallic microcavities.

Organic molecules also exhibit coupling between electronic transitions and intramolecular vibrations, leading to observable vibronic structures in their optical spectra. [110, 112] This gives rise to vibronic progressions in absorption and emission spectra, where multiple peaks correspond to transitions between different vibrational levels of the electronic states. [113, 114] The Franck–Condon principle provides a framework for understanding these features, positing that electronic transitions occur on timescales much faster than nuclear motions. [111, 112] Consequently, during an electronic excitation, the nuclei remain in their initial positions, resulting in vertical transitions on a potential energy diagram. [113] The intensity distribution of the vibronic bands is governed by the overlap between vibrational wavefunctions of the initial and final states, known as Franck–Condon factors. [110, 112] This principle is illustrated in Figure 2.8, which shows a Jablonski diagram and simulated absorption and PL spectra, highlighting vibronic transitions typical of organic emitters.

Organic materials typically display inhomogeneously broadened spectra, with broadening often spanning several hundred meV. [110, 114] This broadening arises from a combination of vibronic coupling and energetic disorder within the material. The latter originates

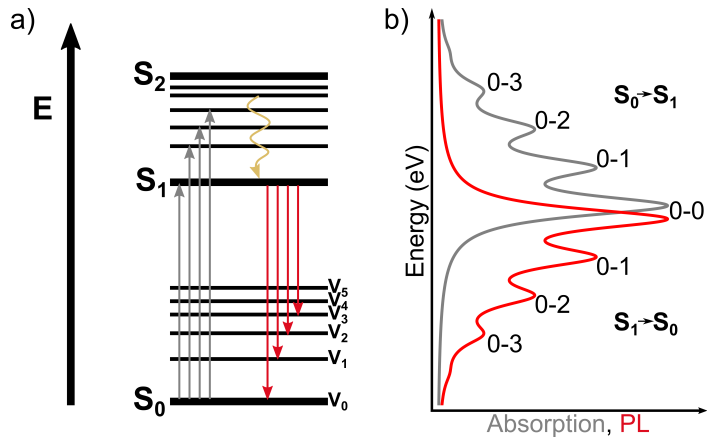

Figure 2.8. (a) Jablonski diagram illustrating electronic states and transitions, including absorption (grey vertical arrows), PL (red vertical arrows), and internal conversion (IC, yellow curved arrow). (b) Simulated absorption and PL spectra showcasing vibronic structures typical of organic emitters.

from variations in local molecular environments, such as differences in molecular packing, polarity, or conformational disorder. [110, 115] As a result, light couples not to a discrete excitonic transition, but rather to a distribution of vibronic states, making spectral resolution more challenging. To resolve anticrossing behaviour and well-defined polariton branches in such disordered systems, the coupling strength must exceed the combined linewidths of both the excitonic and photonic modes. [11, 12] Organic microcavities have successfully demonstrated Rabi splittings of 100–300 meV, significantly larger than those seen in inorganic systems, enabling strong coupling at room temperature. [3, 116, 117]

As the understanding of exciton-polariton systems grows, there is an increasing demand for new classes of organic molecules to further advance the field. A key advantage of organic materials is their chemical tunability. Molecular structure can be readily modified to alter optical properties such as absorption wavelength, linewidth, and dipole moment. One class of emitters receiving growing interest is N-heteropolycyclic aromatic compounds, which are formed by incorporating nitrogen atoms into π-conjugated polycyclic frameworks. [118–126]

2.5 Photophysics of N-Heteropolycycles

N-heteropolycyclic aromatic compounds (NHP) are a class of conjugated organic molecules derived from polycyclic aromatic hydrocarbons (PAH) by substituting sp^2 carbon atoms with nitrogen within the π-conjugated framework. [127] This substitution modifies the electronic structure by introducing nitrogen lone-pair orbitals and increasing the electronegativity of the ring system, which lowers the energy of π^* molecular orbitals. These changes

alter ionisation potential, electron affinity, and HOMO-LUMO energy gaps, directly influencing photophysical properties such as absorption, emission, and excited-state dynamics. [120,128,129] In this thesis, a set of N-heteropolycyclic emitters is examined to evaluate their suitability for strong coupling in microcavity environments. These include tetraazaperylenes [78,118,130–132] and TAC, [133–136] as well as commercially available oxazine and cyanine dyes. These molecules span different regions of the visible to near-infrared spectrum and exhibit diverse vibronic structures, linewidths, and quantum yields.

Perylene comprises two fused naphthalene units with partially connected π-systems, resulting in incomplete π-electron delocalisation across the core. Among perylene-based derivatives, perylene diimides have been investigated for optoelectronic applications due to their thermal and photochemical stability. PDI derivatives have demonstrated strong light–matter coupling in optical microcavities [107, 137], including reports of polariton condensation at room temperature [16]. These findings underscore the potential of perylene-based NHP in molecular polaritonics. The electronic and optical properties of the perylene core can be modified by substituting the peri, ortho, or bay positions with heteroatoms. [78, 118, 131, 138, 139] Tetraazaperylene is a nitrogen-substituted perylene derivative, where four nitrogen atoms are incorporated at the ortho positions, forming 2,5,8,11-tetraazaperylene (Figure 2.9 (a)). Peripheral substitution affects solubility, solid-state packing, and emissive properties. In this work, a series of tetraazaperylene derivatives functionalized at the peri positions with thioether groups—alkyl, benzyl, and PMB are studied. These compounds exhibit molar extinction coefficients greater than $10^5\,\mathrm{M}^{-1}\mathrm{cm}-1$ and PLQY exceeding 60% in solution. [78] Their absorption spectra contain two maxima in the green region and an additional UV absorption band. Compared to unsubstituted perylenes, the TFTAP display broadened absorption and PL spectra due to changes in the electronic structure and vibronic coupling introduced by the substituents. The potential of these compounds in molecular polaritons is further explored and evaluated in Chapter 3 of this thesis.

Coronenes are polycyclic aromatic hydrocarbons composed of six benzene rings fused in a circular arrangement. Their planar geometry and extended π-conjugation render them suitable scaffolds for functionalisation. Nitrogen incorporation into the coronene core leads to TAC, a subclass of azacoronenes containing four nitrogen atoms substituted into the aromatic framework (Figure 2.9 (b)). [140–144] TACs exhibit well-resolved vibronic structure in their UV/Vis absorption spectra, with high molar extinction coefficients that scale with the π-conjugation length. [144] Unlike many organic dyes that exhibit spectral broadening in solid-state or amorphous films, TACs retain well-resolved vibronic features even in solution-processed thin films. This reduced environmental sensitivity allows for clearer interpretation of exciton–phonon interactions under strong coupling conditions. Additionally, their spectral features remain sharp without requiring supramolecular ordering, in contrast to systems

like J-aggregates that rely on aggregation-induced coherence. The PLQY of TACs reach up to 80% in solution. [144] The high quantum yield, together with the rigid molecular backbone, indicates efficient radiative decay and limited non-radiative losses. The retention of vibronic structure in thin films and stable emission properties makes tetraazacoronenes particularly suitable for molecular polaritonics and further exploring the influence of vibronic coupling on exciton-polariton population.

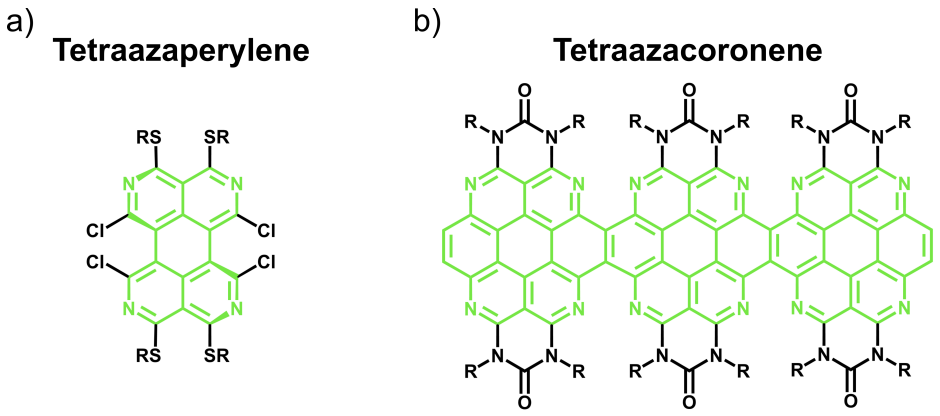

Figure 2.9. Molecular structures of (a) tetraazaperylene and (b) tetraazacoronene derivatives. The core structures are highlighted in green.

Oxazine dyes are planar aromatic compounds belonging to the quinone imine subclass. [145] They typically consist of two phenyl rings fused with a 1,4-oxazine heterocycle as shown in Figure 2.10 (a) and (b), enabling π-conjugation and supporting absorption and PL in the visible to near-infrared range. ATTO 655 and ATTO 680 are members of this dye family and are widely used in super-resolution microscopy techniques such as STORM and STED, owing to their high photostability, efficient PL, and compatibility with aqueous environments. [146–149] These dyes absorb and emit in the red to far-red spectral region and exhibit stable PL under continuous illumination. [150, 151] In this work, ATTO 655 and ATTO 680 are used as donor molecules in polariton-mediated energy transfer studies. Their absorption and PL spectra lie in the red region and were selected to be spectrally compatible with the near-infrared acceptor dye.

Cyanine dyes are a class of polymethine-based fluorophores composed of two nitrogen-containing heterocycles connected by a conjugated polymethine chain. [152] The specific dye used in this work, IRDye 800CW-carboxylate, is an indocarbocyanine that absorbs and emits in the near-infrared (NIR) region (Figure 2.10 (c)). Cyanine dyes are commonly classified as open-chain (streptocyanines) or closed-chain, depending on the substitution pattern around the terminal nitrogen atoms. The optical properties of these dyes are governed by the length of the polymethine chain, which tunes the HOMO–LUMO gap. Each additional vinylene (–CH=CH–) unit in the chain typically red-shifts the absorption maximum

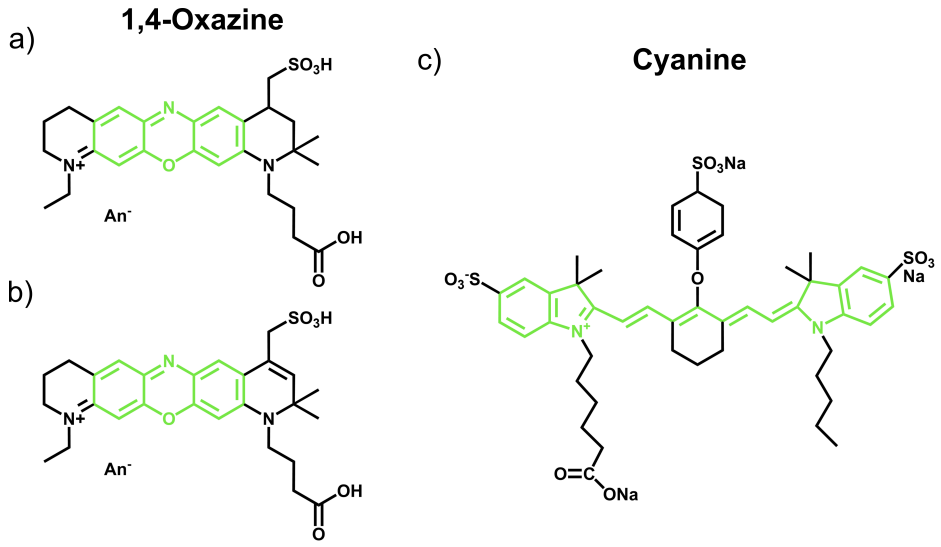

Figure 2.10. Molecular structures of (a) ATTO655 and (b) ATTO680, belonging to the Oxazine family, and (c) IR Dye800CW carboxylate (IR Dye), a Cyanine dye. The core structures are highlighted in green.

by approximately 100 nm. [152] Cyanines are widely used in biomedical imaging due to their strong NIR absorption, relatively narrow spectral features, and moderate PLQY (up to $\approx$ 30%). [153, 154] However, their photostability and emission characteristics can vary depending on chain length, solvent polarity, and the presence of substituents that restrict conformational flexibility. In this study, IRDye 800CW is used as an acceptor molecule in a donor–acceptor microcavity system, where its absorption in the 770–800 nm range complements the emission of red-absorbing donor dyes.

2.6 Polariton population pathways in organic microcavities

Under non-resonant excitation, emission from strongly coupled organic microcavities primarily originates from the LP branch. This reflects relaxation of excitations into the LP states from the exciton reservoir (ER). In contrast, emission from the UP is typically weak due to its short lifetime. [11, 155, 156] The LP population is of particular interest because it plays a central role in phenomena such as polariton lasing, facilitating cavity-mediated energy transfer. [10, 14, 157] These applications rely on achieving and sustaining a sufficiently high LP population, highlighting the importance of understanding the relaxation pathways that populate this branch.

A widely adopted framework to describe polariton population under non-resonant excitation was developed by Lidzey and Coles. [33] In this model, non-resonant optical pumping,

typically at energies above the molecular exciton, generates incoherent electronic excitations that relax into the ER within approximately 100 fs. [72, 158] While the UP branch can be populated from the ER, efficient scattering channels quickly deplete it within about 10 fs. [72, 159] The population of the LP branch is primarily governed by two slower processes that transfer excitations from the ER: VAS [160, 161] and RP [162]. These processes typically act on picosecond timescales and are influenced by molecular photophysics, vibrational structure, cavity detuning, and the energetic alignment between vibrational modes and polariton states.

Figure 2.11 illustrates these two dominant relaxation pathways. Radiative pumping involves spontaneous emission from ER excitons into the cavity mode, leading to LP population. In contrast, vibrationally assisted scattering relies on molecular vibrations to bridge the energy gap between ER and LP states, enabling phonon-mediated population transfer.

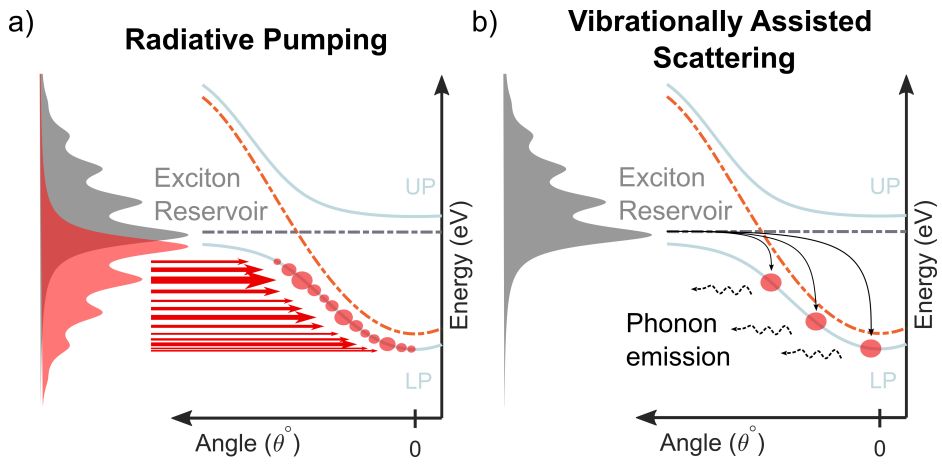

Figure 2.11. Schematic illustration of competing polariton relaxation pathways in organic microcavities. (a) Radiative Pumping: Incoherent excitons in the ER spontaneously emit photons (red arrow) into the cavity mode, populating the LP states. This process is governed by the photonic component of the LP and is enhanced at small angles where the LP is more photon-like. (b) Vibrationally Assisted Scattering: Population transfer from the ER into LP states occurs via interaction with specific molecular vibrations. This process involves the emission of a phonon (vibrational quantum) and enables energy-specific relaxation when the energy gap between the reservoir and LP matches a vibrational mode.

Despite significant experimental and theoretical progress, the precise mechanisms governing polariton population remain incompletely understood, in part due to the complex interplay of radiative, vibronic, and incoherent processes.

2.6.1 Radiative pumping

Radiative pumping describes a mechanism in which photons emitted by incoherent excitons in the ER are reabsorbed by LP modes of the cavity. This process is facilitated by spectral overlap between the PL of uncoupled states and the LP dispersion. In steady-state measurements, radiative pumping is identified by enhanced LP emission that broadly follows the spectral envelope of the uncoupled molecular PL and is strongest where it overlaps with the LP dispersion.

This mechanism has been experimentally demonstrated in both organic [162–165] and hybrid perovskite microcavities [166]. It has been shown to significantly contribute to LP population under non-resonant excitation. [84] Early experimental evidence for radiative pumping was provided by time-resolved and temperature-dependent studies on BODIPY-filled microcavities, where efficient LP population was attributed to high PLQY and favourable spectral alignment. [162] Similar behaviour was observed in bis(phenylethynyl anthracene) (BPEA) systems, where LP population was linked to emission from excimer states and shaped by intermolecular interactions. [164]

Theoretical models based on rate equations have been used to describe RP as a transfer channel between ER and LP states, successfully reproducing observed PL features across varying cavity detunings and temperatures. [162] More recent work has introduced microscopic treatments of RP in molecular ensembles, incorporating internal vibronic structure. [**?**] In these models, RP is described as photon emission from incoherent excitons, followed by photon reabsorption by LP modes. This includes a component termed polariton-assisted photon recycling, wherein photons contribute to long-range energy redistribution across the cavity via reabsorption. Although these models are not implemented explicitly in this thesis, they provide essential conceptual tools for interpreting detuning-dependent PL features in systems with significant vibronic structure, as discussed in Chapter 5.

2.6.2 Vibrationally assisted scattering

Vibrationally assisted scattering is a relaxation pathway by which population from the ER are relaxed into the LP branch via interaction with specific molecular vibrations coupled to the excited state. In strongly coupled systems, VAS enables relaxation by coupling electronic transitions to quantised molecular vibrations, allowing the excess energy to be dissipated through the emission of a vibrational quantum (phonon). [167, 168] This process is driven by vibronic coupling, the interaction between electronic and vibrational degrees of freedom, and is particularly effective in systems exhibiting vibronic progression in their absorption or emission spectra. [14, 15, 107]

VAS does not involve the emission of photons during the transfer itself. Instead, it en-

ables otherwise forbidden transitions between ER and LP states by leveraging resonance with discrete vibrational modes, often those accessible via Raman spectroscopy. [169] However, not all Raman-active modes contribute equally to VAS, and the extent of their participation depends on factors such as vibrational energy alignment and molecular structure. [170, 171]

Experimental evidence for VAS has been observed in various organic microcavity systems. Chovan et al. [160] investigated J-aggregate microcavities and reported enhanced emission from LP states when their energy separation from the ER matched discrete vibrational modes of the dye molecules, which correspond to Raman-active phonons. Quantum kinetic modelling incorporating exciton–phonon interactions supported these observations. Coles et al. [161] demonstrated temperature-dependent redistribution of polariton population in TDBC-based microcavities, further confirming the role of vibrational scattering. Somaschi et al. A rate-equation model incorporating vibrational scattering reproduced the observed emission behaviour, highlighting the tunability of VAS via thermal effects. Somaschi et al. [172] investigated similar systems and showed that VAS enables ultrafast population of LP states on sub-100 femtosecond timescales, highlighting VAS as an efficient relaxation pathway even in disordered J-aggregate systems. Ballarini et al. [173] investigated squaraine-based organic microcavities and provided indirect evidence that phonon-assisted relaxation into LP states can lead to significant emission enhancement.

Theoretical insight into VAS has been expanded through multiscale molecular dynamics simulations. [174] Tichauer et al. studied polariton relaxation in tetracene-based microcavities. They found that specific molecular vibrations can actively drive the transfer of population from ER into the LP states through vibronic (or non-adiabatic) coupling. They also suggested that the previously identified RP mechanism is actually a form of VAS that doesn't require a change in vibrational eigenstates. A more recent work by Pérez et al. [84] identifies VAS as a second-order process in the single-molecule light-matter coupling strength V_1. It involves the emission of virtual photons from an incoherent exciton, followed by Raman scattering on a second molecule.

2.6.3 Competing relaxation pathways: RP versus VAS

The relative contributions of RP and VAS to LP population are governed by a combination of material properties, cavity detuning, light–matter coupling strength, and the excitation conditions. For instance, systems with large Stokes shifts, such as Rhodamine 6G, tend to favour RP due to strong spectral overlap between molecular PL and the LP dispersion, whereas systems with small Stokes shifts, such as J-aggregates, exhibit enhanced VAS through resonance with discrete vibrational modes. [37]

Molecular dynamics simulations suggest that both VAS and RP are governed by vibronic coupling between dark excitonic states and polaritonic modes. [174] The efficiency of these

relaxation channels also depends on the polariton lifetime, typically on the order of 100 fs, which limits further relaxation following initial LP population. This short timescale affects the competition between RP and VAS, as well as the potential for their coexistence. PLQY and radiative rates further modulate the efficiency of relaxation and the formation of polariton condensates. [162]

Polariton lasing has been widely observed in organic materials with vibronic progression, with lasing occurring specifically when the cavity detuning brings the lower polariton into resonance with a molecular vibrational level. [8, 14–16] This highlights the crucial role of vibronic structure in facilitating efficient population of the polariton ground state. While much of the existing research on polariton population pathways has focused on materials systems that often lack resolved vibronic progression in their excited-state manifolds, [37, 162–165] the relaxation mechanism in molecules with spectrally distinct vibronic levels, and how these features influence polariton relaxation mechanisms remain largely unexplored.

Theoretical work by Mazza et al. [167] showed that in organic microcavities with molecules that have pronounced vibronic progression, new pathways can open up for polariton relaxation. In these systems, an exciton can relax by emitting a photon while leaving the molecule in a vibrationally excited ground state. If the energy of the emitted photon matches the energy of a LP state, it can be efficiently absorbed, leading to selective population of that state. This means that vibronic replicas in the molecule create specific energy gaps that enable targeted relaxation into polariton modes, something that is not possible in systems without such vibronic features. A recent theoretical framework by Pérez et al. [84] provides a comprehensive and systematic treatment of polariton relaxation in strongly coupled systems. The authors distinguish between different regimes of vibronic coupling— that is, how strongly the electronic excited states of the molecule interact with its vibrational modes. In systems with weak vibronic coupling, the interaction is relatively small, and the electronic excited state remains mostly unaffected by the vibrational structure. In this case, two main relaxation pathways dominate: RP, which is a first-order process in the light–matter interaction strength V_1, meaning its rate increases directly with the strength of the light–matter interaction for a single molecule and VAS, a second-order process that becomes efficient when the energy difference between molecular fluorescence and the lower polariton matches a Raman-active vibration. In systems with stronger vibronic coupling, where the influence of vibrational motion on the electronic states is much more pronounced, the excited states become more complex, involving combinations of several vibrational levels. As a result, the polariton states are not just mixtures of photons and excitons, but also include multiple vibrational contributions. In this regime, higher-order relaxation processes can begin to play a role. This extended framework highlights how the interplay between vibrational struc-

ture and light–matter coupling strength shapes the available relaxation pathways in organic microcavities. While not applied directly to specific experimental systems in this thesis, these theoretical models help interpret the role of vibronic structure in polariton relaxation mechanisms.

2.7 Polariton-mediated long-range energy transfer

Understanding and controlling energy transfer between molecular species is important for applications such as light harvesting, organic photovoltaics, fluorescence imaging, and molecular sensing. [175–182] In conventional systems, energy transfer between a donor and an acceptor molecule typically occurs through near-field dipole–dipole interactions such as Förster resonance energy transfer (FRET), which is limited to short distances, typically under 10 nm, and strongly dependent on spectral overlap and molecular orientation. [183] This process involves the non-radiative transfer of electronic excitation energy from an excited donor to a spatially separated acceptor without the emission and reabsorption of photons, often leading to radiative emission or chemical reactivity at the acceptor site (see Figure 2.12 (a)). [184]

In contrast, strong light–matter coupling introduces a fundamentally new regime of energy transport. When donor and acceptor molecules are embedded in a resonant optical cavity and both interact coherently with the same cavity mode, the resulting hybrid light–matter states offer a delocalised and coherent channel for mediating energy transfer. [36] This polariton-mediated energy transfer mechanism can operate over distances far exceeding the FRET limit, since the polaritonic states are shared across the entire optical mode volume, often spanning hundreds of nanometres to microns (see Figure 2.12 (b)). [17]

In this context, a donor is typically defined as a molecular species with a higher-energy electronic transition that can populate polaritonic states through optical or vibrational relaxation. The acceptor, on the other hand, is a lower-energy molecule that can receive energy from the polariton states. The formation of shared polariton modes between donors, acceptors, and the cavity mode gives rise to unique transport behaviour that is fundamentally distinct from resonance energy transfer paradigms.

This section first presents the CHO framework for describing hybridisation between two distinct excitonic species and a common cavity mode, following the formalism outlined in [185]. It then reviews recent experimental studies on polariton-mediated energy transfer in spatially separated donor–acceptor systems.

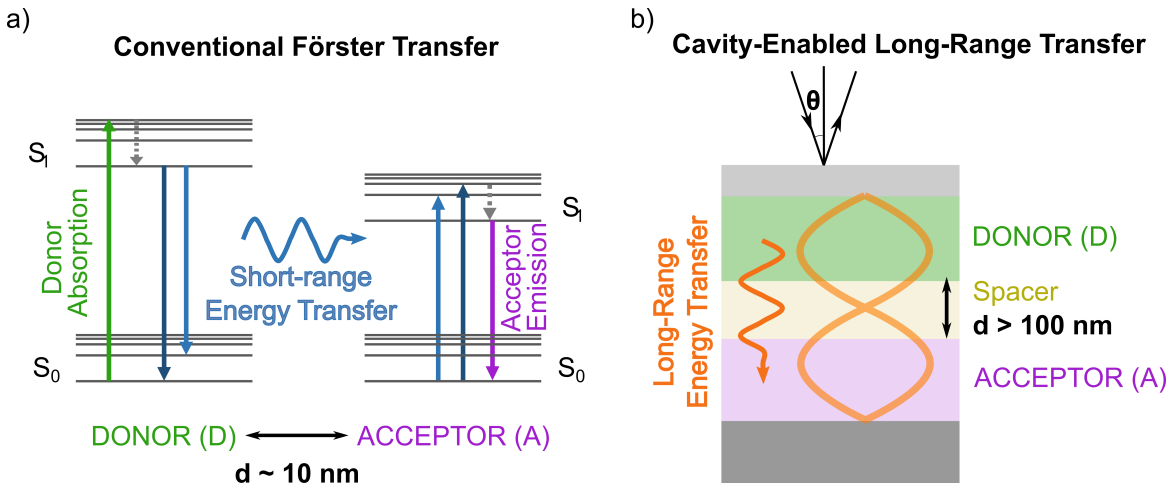

Figure 2.12. (a) Simplified Jablonski diagram of short-range energy transfer in a donor–acceptor pair. Upon photoexcitation (green upward arrow), the donor is excited to its singlet excited state (S_1) and transfers energy non-radiatively to the acceptor via near-field interactions (blue arrows), followed by acceptor emission (purple downward arrow). The donor–acceptor separation is typically ≈10 nm. Grey dashed arrows indicate internal conversion (IC). (b) Microcavity structure enabling long-range energy transfer via a shared cavity mode. The donor (green layer) and acceptor (purple layer) are spatially separated by a spacer layer (beige), with total separation exceeding 100 nm. The orange profile represents the electric field of the cavity mode, which is delocalised across all layers. The orange wavy arrow shows polariton-mediated energy transfer from the donor to the acceptor through this shared optical mode. Incident light enters the cavity at angle θ.

2.7.1 Strong coupling-induced hybridisation of different excitonic states

The discussion thus far has centred on the interaction between cavity photons and a single excitonic mode. This section delves into the coupling of a cavity photon with two excitonic modes, resulting in hybrid polariton states. These excitons can originate from the same molecule [15, 78, 186] or from different molecules [187–190]. The focus here is on excitons from distinct molecules, such as those in a donor-acceptor system depicted in Figure 2.12 (b).

The initial experimental evidence of hybridization between excitons from two distinct organic emitter within an optical microcavity was provided by Lidzey et al. [187] To ensure that the only interaction between the two exciton types was facilitated by a cavity photon, two cyanine dyes that support excitons were separated by a 100 nm polystyrene spacer layer within a microcavity. The optical cavity mode was engineered to be nearly resonant with both excitons, featuring nodes at the mirror surfaces and a peak at the spacer layer. By adjusting the angle at which white light was incident, the energy of the cavity mode could

be tuned to resonate with each exciton. Reflectance spectra revealed up to three minima, and when these were plotted against the angle of incidence, two avoided crossings were detected at energies corresponding to the unaltered excitons (see Figure 2.14 (a)). These results matched theoretical predictions and indicated that excitons from distinct molecular species could become indirectly coupled through their interaction with a shared cavity mode, leading to the formation of mixed light–matter states that involve both emitters.

The compound oscillator, which consists of two excitons and a single cavity mode, can be modelled using the CHO framework. The Hamiltonian for this system is expressed as:

$$H = \begin{bmatrix} E_c & V_D & V_A \\ V_D & E_d & 0 \\ V_A & 0 & E_A \end{bmatrix} \tag{2.30}$$

where E_c is the energy of the uncoupled optical resonance. E_D indicates the donor electronic excited state energy, while E_A represents the acceptor's excited state energy. The interaction between the resonant cavity mode and the excited electronic states of the donor and acceptor is characterised by the coupling constants V_D and V_A, respectively.

The hybridisation results in three polariton modes called UP, middle polariton (MP) and LP as shown in Figure 2.13, which are linear combinations of photon and both excitons, described as: [185]

$$|\psi\rangle = \alpha\,|D, A; n+1\rangle + \beta\,|D^*, A; n\rangle + \gamma\,|D, A^*; n\rangle \tag{2.31}$$

where the D^*, A^* are the excited donor and acceptor species, D, A are the ground state donor and acceptor species, $|D^*, A\rangle$ and $|D, A^*\rangle$ represent the states of matter, and n is the number of photons. $|D, A; n+1\rangle$ is the state where both D and A are in the ground state and there is a virtual photon present. The coefficients α, β, γ are found as solutions to the equation $H|\psi\rangle = E|\psi\rangle$.

Following the derivation approach outlined by Tibben et.al [185], the simplified assumption $E_A = E_D = E_c = E_0$ is applied to equation 2.31, leading to the following allowed energies of the interacting system:

$$E_{MP} = E_0, \quad E_{UP,LP} = E_0 \pm \sqrt{V_D + V_A} \tag{2.32}$$

which become new excited-state energies of the system as shown in Figure 2.13.

These have associated eigenvectors given by:

$$\begin{aligned} |MP\rangle &= \frac{1}{V^*}\left(-V_A|D^*, A; n\rangle + V_D|D, A^*; n\rangle\right), \\ |UP, LP\rangle &= \frac{1}{V^*\sqrt{2}}\left(V^*|D, A; n+1\rangle \pm \left(V_A|D^*, A; n\rangle + V_D|D, A^*; n\rangle\right)\right). \end{aligned} \tag{2.33}$$

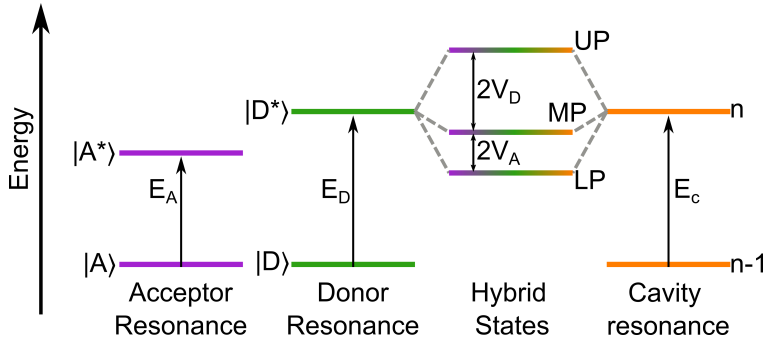

Figure 2.13. Schematic depiction of the coupling between the donor molecular transition, the acceptor molecular transition, and the cavity resonance. The interaction yields three hybrid light-matter states: LP, MP, and UP. Coupling strengths V_A and V_D are indicated.

where $V^* = \sqrt{V_D^2 + V_A^2}$

This shows that energy oscillates between donor and acceptor in the middle polariton state, independent of their separation distance. This results in long-range, coherent energy exchange between donor and acceptor molecules, enabling distance-independent energy transfer that surpasses the limitations of conventional dipole–dipole interactions. This oscillation is influenced by the interactions between each species and the cavity mode. For conditions of strong light-matter coupling, energy transfer is measured by assessing the projection of the state of the system onto the transfer target state, where the excited state energy is located in A ($|D, A^*; n\rangle$). The likelihood of the system being in this state fluctuates and peaks when the donor and acceptor are equally coupled to the cavity mode. If the system starts in the $|D, A; n + 1\rangle$ state, the probability of energy transfer nears one only when there is asymmetric coupling with $V_A > V_D$. [36]

The composition of polariton states is governed by the Hopfield coefficients (see figure 2.14 (b)), which depend on the coupling strengths between the cavity mode and each molecular species (V_D for the donor and V_A for the acceptor). These coupling strengths are determined by the transition dipole moments of the excited states and the amplitude of the cavity's electric field at the spatial position of each emitter. By precisely controlling the spatial placement of donor and acceptor molecules within the cavity, particularly relative to the electric field profile, one can tune the nature of the hybrid states and modulate the probability of energy transfer between them.

For non-resonant cases, $E_A \neq E_D \neq E_c$ excited-state energies show avoided crossings at E_A and E_D positions. Time evolution of Hopfield coefficients demonstrates oscillatory energy sharing among system constituents. [185] When acceptor-cavity coupling exceeds donor-cavity coupling, the probability of finding the system in the target state increases. Further, at zero cavity detuning, maximum hybridisation occurs with equal contributions from $|D^*, A; n\rangle$ and $|D, A^*; n\rangle$, leading to equal energy distribution between donors and ac-

ceptors upon photoexcitation.

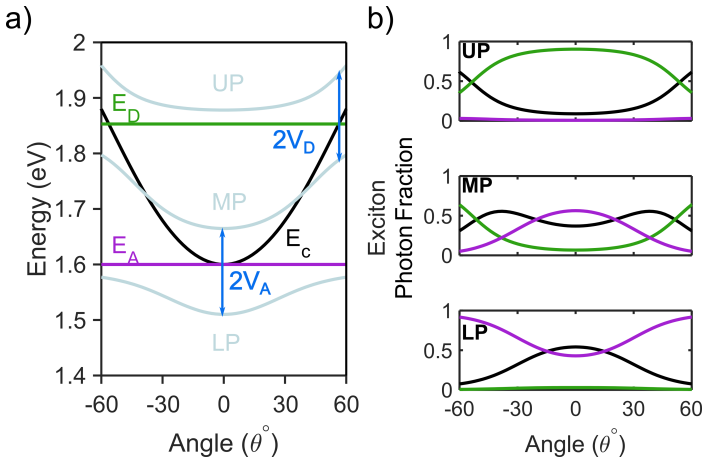

Figure 2.14. (a) Dispersion plot illustrating zero detuning with VA = 80 meV and VD = 40 meV. The plot displays LP, MP, and UP dispersions. Donor energy (E_D), acceptor energy (E_A), and dispersive cavity energy (E_c) are indicated. Coupling strengths between donor and cavity (V_D) and acceptor and cavity (V_A) are marked. (b) Corresponding Hopfield coefficients.

2.7.2 Energy transfer in spatially separated Donor-Acceptor pairs

Polariton-enhanced energy transfer has been demonstrated in various systems, including J-aggregated molecular dyes [191] and boron-dipyrromethene (BODIPY) core dyes. Zhong et al. [191] showed that energy transfer between donor and acceptor molecules becomes effectively distance-independent under strong light–matter coupling, provided both species are coupled to the same optical mode. They constructed a Fabry–Pérot microcavity with donor and acceptor layers positioned at the antinodes of a second-order cavity mode, achieving separation distances up to 100 nm. Despite this considerable spacing, excitation energy was funnelled efficiently to the system's lowest-energy excited state.

Building on this concept, Georgiou et al. [17] and Ściesiek et al. [192] extended the donor–acceptor separation to approximately 2 µm by leveraging strong coupling to cavity modes. Akulov et al. [193] explored a related mechanism involving hybrid states formed by coupling a surface plasmon mode with an optical cavity mode.

In a separate study, Georgiou et al. [194] investigated how molecular spatial arrangement influences energy transfer efficiency. By comparing an intermixed donor–acceptor blend with a layered structure where donors and acceptors were spatially separated, they found that energy transfer in the layered configuration was strongly dependent on cavity detuning, with negative detuning leading to enhanced transfer. However, they also observed that energy

transfer facilitated by strong coupling was generally less efficient than traditional Förster-type (dipole–dipole) energy transfer.

More recently, ultrafast two-dimensional white-light spectroscopy has shed light on the microscopic mechanisms underlying polariton-assisted energy transfer. Son et al. [195] revealed that intermediate manifold states play a central role in enabling long-range energy transfer between distinct molecular species under strong coupling conditions.

3. Materials and Methods

This chapter details the materials, fabrication methods, and characterisation techniques used to study strong light–matter coupling in organic microcavities.

3.1 Materials

3.1.1 Excitonic materials

The excitonic materials used in this thesis include both synthesised and commercially available compounds. The molecular structures of all emitters are shown in Figure 3.1, and their sources are summarised in Table 3.1.

Table 3.1. List of excitonic materials, corresponding matrix polymers and solvents used, along with their suppliers

Excitonic Material	Supplier
butyl-TFTAP	Synthesised by Dr. Tobias Wesp [78]
benzyl-TFTAP	Synthesised by Dr. Tobias Wesp [78]
PMB-TFTAP	Synthesised by Dr. Tobias Wesp [78]
TAC Trimer	Synthesised by Dr. Robert Eichelmann [144]
IR Dye	LI-COR Biosciences
ATTO680	ATTO-TEC GmbH
ATTO655	ATTO-TEC GmbH

Three functionalised tetraazaperylene derivatives with butyl, benzyl, and PMB substituents were synthesised by Dr. Tobias Wesp in the group of Prof. Lutz H. Gade, as reported in Ref. [78]. These compounds were used in Chapter 4 to investigate strong light–matter coupling and energetic tunability in single-layer microcavities. The TAC trimer, prepared by Dr. Robert Eichelmann [144], was employed in Chapter 5 to study polariton relaxation dynamics in a system that exhibits vibronic progression. All four compounds show good solubility in toluene, which allows for the formation of uniform thin films when processed with polystyrene as the matrix material.

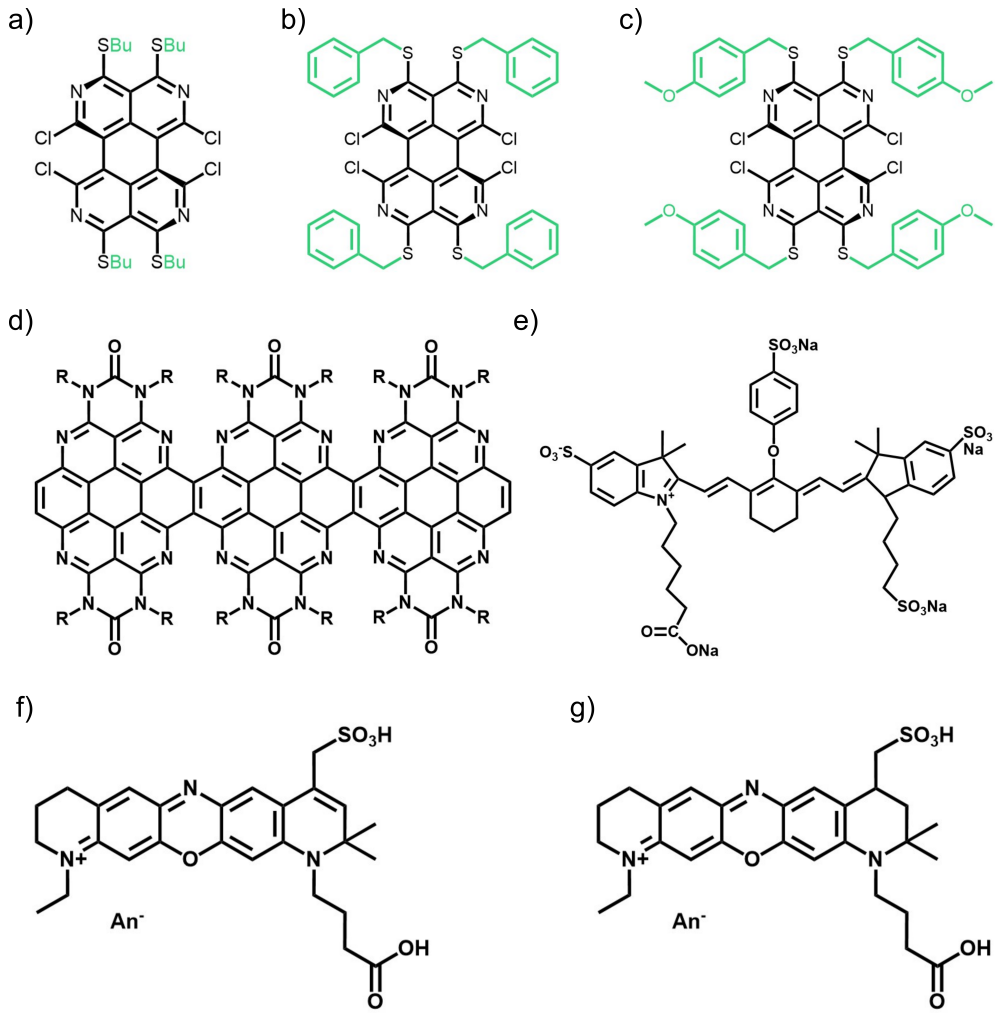

Figure 3.1. Molecular structure of a) butyl-, b) benzyl-, c) PMB-substituted tetraazaperylene d) Tetraazacoronene Trimer, e) IRDye 800CW carboxylate f) ATTO680 g) ATTO655

In Chapter 6, polariton-mediated energy transfer is studied using a donor–acceptor system. The acceptor is IR Dye (LI-COR), and ATTO655 and ATTO680 (ATTO-TEC) are the chosen donor dyes. These commercially available dyes were chosen for their water solubility and spectral compatibility with the cavity design. Their emission and absorption properties support spatially resolved energy transfer when incorporated into a multilayer cavity structure.

To prevent intermixing between donor and acceptor layers, an aluminium oxide (Al_2O_3) spacer was used. This layer was deposited by atomic layer deposition and selected for its smoothness and insolubility in subsequent processing steps. All emitters in this thesis absorb and emit in the visible spectral region. Consequently, silver was chosen for both top and bottom cavity mirrors due to its high reflectivity in this wavelength range.

3.1.2 Matrix polymers and solvents

The choice of matrix polymer and solvent was guided by the solubility and stability requirements of the respective emitters and the need to form homogeneous, uniform thin films suitable for optical microcavities. This thesis used two types of matrix polymers: polystyrene (PS) for toluene-soluble compounds, and polyvinyl alcohol (PVA) for water-soluble dyes.

Polystyrene (PS, atactic, Mn = 218 kg mol^{-1}, Mw = 222 kg mol^{-1}, Polymer Source Inc.) was selected as the matrix for TFTAP derivatives and the TAC trimer. These materials dissolve well into toluene, which allowed for reproducible film formation via spin coating. PS is optically inert in the visible region and exhibits good film-forming properties, making it a suitable host material for strongly coupled systems.

For the ATTO dyes and IRDye 800CW used in donor–acceptor experiments (Chapter 6), PVA (99+%, hydrolysed, Mw = 89,000–98,000 kg mol^{-1}, Sigma Aldrich) was chosen as the matrix polymer. These dyes are water-stable and can dissolve in polar solvents such as dichloromethane (DCM), dimethyl sulfoxide (DMSO), and acetonitrile. However, for multilayer film fabrication, aqueous solutions were preferred, and PVA provided a stable, water-soluble matrix compatible with these conditions.

3.2 Thin film deposition technique

3.2.1 Single-layer films

Single-layer films incorporating excitonic materials in a polymer matrix were used as the active medium in optical microcavities designed to probe polariton formation and relaxation pathways. Glass substrates (Schott AF32 eco, 0.3 mm thick) were cleaned by sequential ultrasonication in a 1% Helmanex solution (10 minutes), MilliQ water (30 minutes), acetone (20 minutes), and isopropanol (20 minutes), followed by nitrogen drying. A silver bottom mirror was then deposited via thermal evaporation. Depending on the experimental configuration, the thickness of this layer was either 35 nm (used in Chapter 4) or 100 nm (used in Chapters 5 and Chapter 6). The active layer was prepared by dissolving the polymer matrix, PS, in toluene, followed by adding the excitonic material. The solution was stirred at 90°C until fully dissolved and filtered through a 0.45 µm PTFE filter. The resulting solution was spin-coated onto the bottom mirror using optimised parameters to achieve the desired film thickness and uniformity. The films were annealed at 100–120 °C to remove residual solvent and improve morphology. A semi-transparent silver layer (35 nm thick) was then deposited on top of the active layer to complete the Fabry–Pérot microcavity. For each cavity device, a corresponding reference film was fabricated under identical conditions on a bare glass substrate, without any metal mirrors, to assess the photophysical behaviour of the excitonic

material in the absence of optical confinement. The complete set of spin-coating conditions, material concentrations, and resulting film thicknesses is summarised in Table 3.2.

Table 3.2. Spin-coating conditions, material concentrations, and film thicknesses for the active layers used in single-layer microcavities and their corresponding reference films.

Single-layer Devices			
Active Material, Concentration	Polymer Matrix, Concentration	Spin coating parameters, annealing temperatures	film thickness
butyl-TFTAP, 5 mg/ml	PS, 15 mg/ml	1000 rpm/ 60 s, 120°C/ 60 s	100-250 nm
benzyl-TFTAP, 5 mg/ml	PS, 15 mg/ml	1000 rpm/ 60 s, 120°C/ 60 s	100-250 nm
PMB-TFTAP, 5 mg/ml	PS, 20 mg/ml	1000 rpm/ 60 s, 120°C/ 60 s	100-250 nm
PMB-TFTAP, 10 mg/ml	PS, 14 mg/ml	2000 rpm/ 60 s, 120°C/ 60 s	100-250 nm
PMB-TFTAP, 20 mg/ml	PS, 10 mg/ml	2000 rpm/ 60 s, 120°C/ 60 s	100-250 nm
PMB-TFTAP, 30 mg/ml	PS, 5 mg/ml	2000 rpm/ 60 s, 120°C/ 60 s	100-250 nm
TAC Trimer, ≈ 0.44 µg/ml	PS, 50 mg/ml	5000 rpm/ 60 s, 100°C/ 60 s	350-450 nm

3.2.2 Multilayer films

Multilayer cavities differ from single-layer structures by incorporating two organic layers separated by a dielectric spacer. In the configuration used here, both organic layers are PVA-based and are separated by a 100 nm thick Al_2O_3 spacer.

The fabrication of multilayer cavity devices started with the thermal evaporation of a 100 nm silver bottom mirror onto cleaned glass substrates. A thin Al_2O_3 layer (20 nm) was then deposited to improve the wettability of the surface for subsequent deposition of water-based solutions. The first PVA layer—either undoped or containing the acceptor dye—was spin-coated from aqueous solution and annealed at 100°C. The Al_2O_3 spacer was then deposited by atomic layer deposition (ALD) to create a smooth, insoluble barrier between layers. On top of this, a second PVA layer—either undoped or containing the donor dye—was spin-coated and annealed under the same conditions. Finally, a 35 nm silver top mirror was deposited via thermal evaporation to complete the cavity.

Reference films with the same multilayer organic structure were prepared on glass substrates without metal mirrors. These samples were used to evaluate the optical response of the system in the absence of cavity effects. A summary of the multilayer fabrication process, including the concentrations of excitonic materials and polymers, spin-coating parameters, and the resulting film thicknesses for each layer, is provided in Table 3.3.

Table 3.3. Spin-coating conditions, material concentrations, and film thicknesses for the active layers used in multi-layer microcavities and their corresponding reference films.

Multilayer Devices				
Active Material, Concentration		Polymer Matrix, Concentration	Spin coating parameters, annealing temperatures	film thickness
Layer 1	IR Dye, ≈ 0.75 µg/ml	PVA, 32 mg/ml	5000 rpm/ 60 s, 100°C/ 60 s	130 - 210 nm
Layer 2	Al_2O_3	-	-	100 nm
Layer 3	PVA	PVA, 40 mg/ml	3500 rpm/ 60 s, 100°C/ 60 s	130 - 210 nm
Layer 1	PVA	PVA, 40 mg/ml	3500 rpm/ 60 s, 100°C/ 60 s	130 - 210 nm
Layer 2	Al_2O_3	-	-	100 nm
Layer 3	ATTO655, ≈ 0.54 µg/ml	PVA, 30 mg/ml	3500 rpm/ 60 s, 100°C/ 60 s	130 - 210 nm
Layer 1	PVA	PVA, 40 mg/ml	3500 rpm/ 60 s, 100°C/ 60 s	130 - 210 nm
Layer 2	Al_2O_3	-	-	100 nm
Layer 3	ATTO680, ≈ 0.49 µg/ml	PVA, 30 mg/ml	3500 rpm/ 60 s, 100°C/ 60 s	130 - 210 nm
Layer 1	IR Dye, ≈ 0.75 µg/ml	PVA, 32 mg/ml	5000 rpm/ 60 s, 100°C/ 60 s	130 - 210 nm
Layer 2	Al_2O_3	-	-	100 nm
Layer 3	ATTO655, ≈ 0.54 µg/ml	PVA, 30 mg/ml	3500 rpm/ 60 s, 100°C/ 60 s	130 - 210 nm
Layer 1	IR Dye, ≈ 0.75 µg/ml	PVA, 32 mg/ml	5000 rpm/ 60 s, 100°C/ 60 s	130 - 210 nm
Layer 2	Al_2O_3	-	-	100 nm
Layer 3	ATTO680, ≈ 0.49 µg/ml	PVA, 30 mg/ml	3500 rpm/ 60 s, 100°C/ 60 s	130 - 210 nm

3.3 Angle resolved reflection and PL spectroscopy

Angle-resolved reflection and PL spectra were recorded using a custom-built Fourier-plane spectroscopy setup, schematically illustrated in Figure 3.2. This system enables the simultaneous acquisition of wavelength- and angle-dependent data as shown in Figure 3.3, allowing direct observation of cavity and polariton dispersion.

For reflection measurements, the cavities were illuminated using a white light source (Ocean Optics HL-2000-HP), directed onto the sample via a non-polarising broadband plate beam splitter (Thorlabs BSW29R, 50:50 split ratio). The reflected light was collected through a 60x infinity-corrected microscope objective (Olympus MPLAPON60X, NA = 0.9), which defined an excitation spot of approximately 1 µm on the sample.

For PL measurements, excitation followed the same optical path as the reflection measurements, entering through the beam splitter and the objective before reaching the sample. Two excitation wavelengths were used: a 532 nm continuous-wave laser diode (OBIS) for shorter wavelength excitation (used in Chapter 4), and a 640 nm OBIS laser for longer wavelength excitation (used in Chapters 5 and Chapter 6). To suppress scattered laser light, appropriate optical filters were placed in the detection path: a 550 nm long-pass filter for 532 nm excitation, and a combination of a 650 nm short-pass filter (before the beam splitter) and a 650 nm long-pass filter (after the sample) for 640 nm excitation.

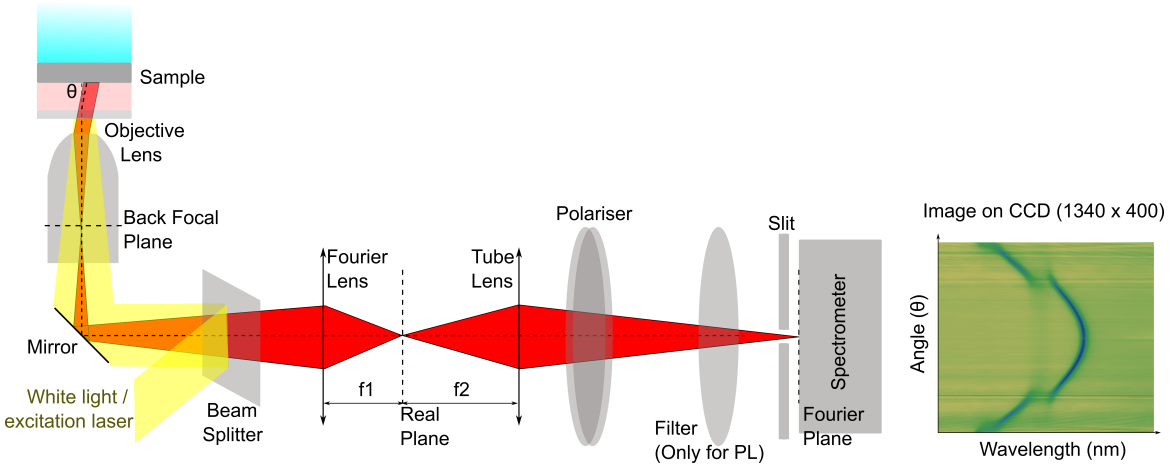

Figure 3.2. Schematic of the Fourier-plane spectroscopy setup used for angle-resolved reflection and PL measurements. The figure shows the excitation path in yellow and the detection path from the microcavity sample to the spectrometer in red.

The reflected or emitted light from the micorcavities were collected through the same objective and directed toward the spectrometer entrance slit (300 µm) via a 4f optical relay. This system comprised a Fourier lens (f_1 = 200 mm, AC254-200-A-ML, Thorlabs) and a tube lens (f_2 = 300 mm, AC508-300-A-ML, Thorlabs), which imaged the back focal plane of the objective onto the spectrometer slit. This imaging geometry maps emission angles onto lateral positions along the slit, enabling acquisition of angle-resolved spectra. A linear polariser (Thorlabs LPVIS100) was placed before the spectrometer to select between

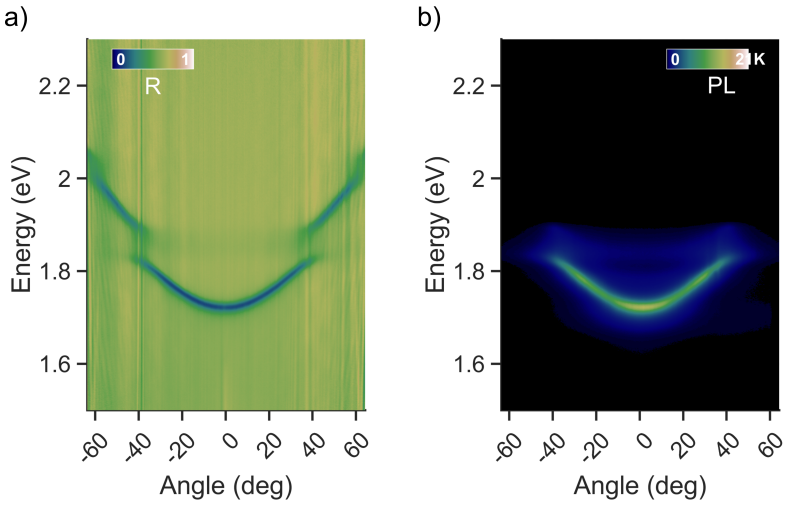

Figure 3.3. Processed angle-resolved spectra acquired using the Fourier-plane spectroscopy system. (a) The reflectivity spectrum shows the lower and upper polariton branches of a strongly coupled microcavity. (b) PL spectrum from the same cavity under off-resonant excitation. The raw CCD images were converted into angle–energy maps by assigning emission angles to pixel positions and applying spectral corrections as described in Section 3.5.2.

TE and TM polarisations; all measurements presented in this thesis were recorded in TE configuration. The spectra were recorded using a 1340 × 400 pixel silicon CCD camera (Princeton Instruments PIXIS:400). Figure 3.3 shows an example of background-corrected angle-resolved reflectivity and PL spectra acquired using the described setup, demonstrating the polariton dispersion features captured in energy–angle space.

PL measurements of the reference films were acquired using the same excitation and detection configuration as for the cavity samples. The recorded angle-resolved data were integrated across all emission angles during analysis to obtain the PL spectra. PL spectra of dye solutions were also recorded using the same configuration by placing a quartz cuvette filled with dye solution in the sample holder at the focal plane of the objective. Excitation followed the same optical path, and the collected emission was similarly integrated over all angles to yield solution-phase PL spectra of the respective dyes.

3.4 Other characterisation techniques

Profilometry- The thickness of single-layer and multilayer films was measured using a DektakXT Stylus Profiler from Bruker Corp. The single-layer films were prepared under the same conditions as those used for the microcavity and multilayer films. All thickness measurements were obtained by scanning across grooves that had been scratched into the films. Spin coating creates a gradient in film thickness; thus, thickness measurements were taken from various positions, from the centre to the corner of the substrate, to obtain the range of thicknesses shown in Table 3.2 and Table 3.3.

Absorption spectroscopy - Absorption spectra of both thin films and dye solutions were recorded using a Varian Cary 6000i UV-Vis-nIR spectrometer. Solution samples were measured in quartz cuvettes (Hellma Analytics, QS material) with a 1 cm optical path length. Baseline corrections were performed using the pure solvent. For thin films, the samples were deposited on optically cleaned Schott AF32 eco glass substrates (0.3 mm thick) and mounted in a custom-built holder for transmission measurements. Baseline correction for film spectra was carried out using the absorption spectrum of a clean glass substrate.

Time-correlated single-photon counting- The PL decay of spin-coated thin films and dye solution was measured using an in-house time-correlated single-photon counting (TCSPC) system. Samples containing the TFTAP derivatives (see Chapter 4) were excited at 535 nm using a picosecond-pulsed supercontinuum laser (NKT Photonics SuperK Extreme). A dichroic long-pass filter with a 550 nm cutoff was used to block scattered excitation light. For TAC trimer (Chapters 5), ATTO dye and IR dye samples (Chapter 6), excitation was performed at 640 nm with a 650 nm long-pass filter in the detection path.

The emitted PL was spectrally filtered using either a bandpass filter (BPF600-40) for the

TFTAP derivatives or a monochromator (Princeton Instruments Acton SpectraPro SP2358), which isolated a narrow spectral window centred around the peak emission wavelength of each material. This selected emission band was directed onto a silicon Single Photon Avalanche Diode (SPAD) detector equipped with integrated active quenching circuits (iAQC, Micro Photon Devices). The SPAD detects the arrival times of individual photons with high temporal resolution. These photon arrival events were recorded using a time-correlated single-photon counting module (PicoHarp 300, PicoQuant GmbH), and the resulting PL decay traces were analysed using bi-exponential fitting, through the convolution mode in the SymPhoTime64 software.

Raman spectroscopy- Raman spectroscopy was conducted using a Renishaw inVia Reflex confocal Raman microscope equipped with a 50x long working distance objective (Olympus, N.A. 0.50) and near-resonant excitation at 532 nm (grating: 2400 lines mm^1). The system was calibrated using a silicon standard (520.6 cm^1) prior to measurement. Raman spectra of drop-cast pristine TAC trimer films were obtained by mapping an area of approximately 100 × 100 μm^2 in Streamline mode, averaging over 1000 individual measurements.

3.5 Data analysis and simulation

Data analysis of the measured spectra was performed using OriginPro 2021 (OriginLab) or MATLAB R2024a (MathWorks). All CHO fits and TMM simulations were conducted in MATLAB.

3.5.1 Thickness determination and E-field intensity simulation using TMM

To determine the layer thickness and simulate the electric field intensity within the cavity stack for different detuning conditions of the TAC trimer cavity (see Chapter 5), TMM simulations were performed in MATLAB. The simulations were based on a modified version of an TMM code originally developed by T. Chervy. [57] This code was adapted to suit the cavity architectures used in this study, allowing flexible definition of layer thicknesses and optical constants.

The multilayer structure simulated for the TAC trimer cavity consisted of Ag (100 nm)/Al_2O_3 (20 nm)/PS: TAC trimer/Ag (35 nm) as shown in Figure 3.4 (a). Refractive indices for silver and Al_2O_3 were taken from Johnson and Christy [196] and Malitson [197], respectively. The optical constants of the PS: TAC trimer layer were calculated from measured absorption spectra using the Kramers–Kronig relation.

The code computes reflectivity and position-dependent electric field intensity across the multilayer structure as shown in Figure 3.4. To simulate the electric field distribution for an experimentally fabricated cavity, it was necessary to accurately reproduce the system parameters, particularly the cavity thickness and the optical constants of the active layer. Although the concentration of the TAC trimer was fixed during sample preparation, this value was not directly input into the simulation. Instead, the corresponding optical constants were determined from absorption spectra measured at the known concentration. The layer thickness was then refined by iteratively comparing the simulated reflectivity spectra with the experimental spectra. This matching was based on the overall spectral shape, including the positions of the UP and LP branches and their separation. Once a good agreement between simulated and measured spectra was achieved, the corresponding thickness value was used to compute the spatial distribution of the electric field intensity under the relevant detuning condition.

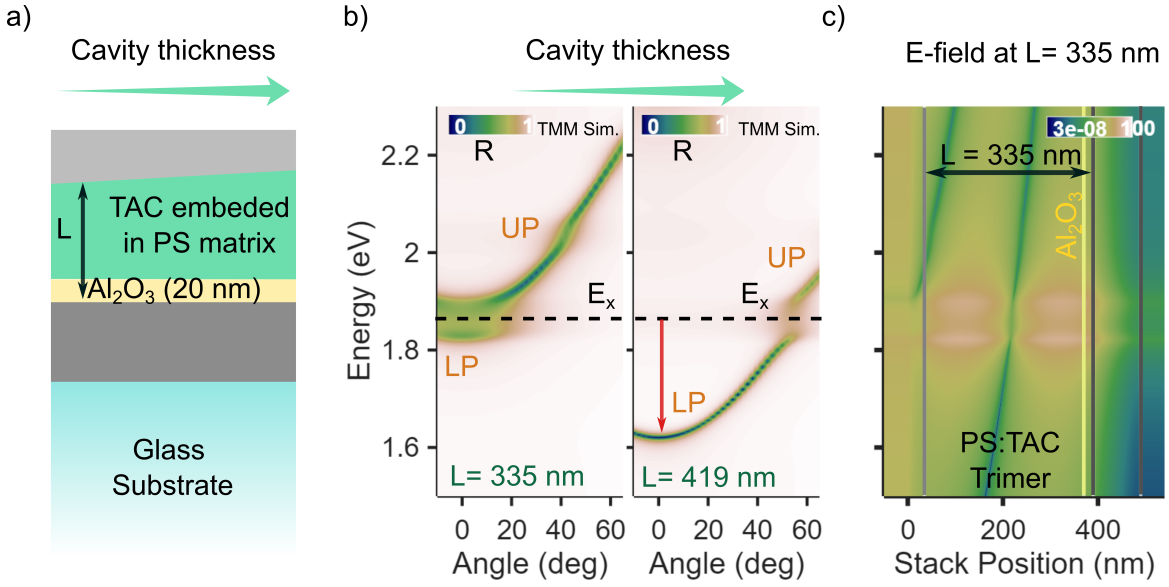

Figure 3.4. (a) Schematic of the simulated cavity stack: Ag (100 nm)/Al_2O_3 (20 nm)/PS: TAC trimer/Ag (35 nm) on glass substrate. The active layer thickness L varies due to spin-coating conditions. (b) Simulated angle-resolved reflectivity spectra for cavity thicknesses of L = 335 nm and L = 419 nm, showing the shift of the LP mode to lower energy as the thickness increases (indicated by red arrow). The exciton energy E_x is marked by a dashed line. (c) Simulated electric field intensity profile for the L = 335 nm configuration, highlighting the field distribution across the cavity stack and the spatial confinement within the PS: TAC trimer layer.

3.5.2 Analysis of angle-resolved spectra

Angle-resolved reflectivity and PL spectra acquired from the Fourier-plane spectroscopy setup were analysed using a MATLAB routine adapted from a script originally developed by Dr. Jan Lüttgens. [198] This script performed spectral corrections for reflectivity measurements. The background correction, however, was handled by the spectrometer control software (LightField 4.5, Teledyne Technologies). The code was modified to incorporate custom peak fitting, spectral corrections, and CHO model fitting for both two- and three-level systems. Angular coordinates were assigned based on the nominal numerical aperture (NA = 0.9) of the objective, and the wavelength axis was converted to energy (eV) for dispersion analysis.

For systems where two polariton branches were observed (e.g., the TAC trimer cavity in Chapter 5) as shown in Figure 3.5 (a), a 2x2 coupled oscillator Hamiltonian was used to describe the interaction between the cavity photon and a single excitonic transition:

$$H_{2x2} = \begin{bmatrix} E_c(\theta) & V \\ V & E_x \end{bmatrix} \tag{3.1}$$

The dispersion of the cavity mode $E_c(\theta)$ was calculated using the standard Fabry–Pérot dispersion relation (see equation 2.3). The exciton energy E_x was determined independently from the absorption spectrum of the corresponding reference film and treated as a fixed input. Experimental mode energies were extracted by fitting a two-peak Lorentzian function to each angle of the reflectivity spectrum (Figure 3.5 (a), right panel). The extracted UP and LP energies were then fitted to the eigenvalues of the Hamiltonian in equation 3.1. From this fit, the coupling strength V and the cavity mode energy at normal incidence $E_c(0)$ were obtained.

In samples where three polariton branches were observed (e.g., TFTAP and donor–acceptor systems in Chapters 4 and Chapter 5 as shown in Figure 3.5 (b), a 3x3 Hamiltonian was used to model the interaction between the cavity mode and two distinct excitonic transitions:

$$H_{3x3} = \begin{bmatrix} E_c(\theta) & V_1 & V_2 \\ V_1 & E_{x1} & 0 \\ V_2 & 0 & E_{x2} \end{bmatrix} \tag{3.2}$$

Experimental mode energies were obtained by fitting a three-peak Lorentzian function to each angle of the reflectivity spectrum (Figure 3.5 (b), right panel). The resulting peak positions correspond to the LP, MP, and UP branches. The exciton energies E_{x1} and E_{x2} were determined from the absorption spectra of the corresponding reference films and used

as fixed inputs in the model. The cavity mode dispersion $E_c(\theta)$ was calculated using the Fabry–Pérot relation (Equation 2.3), as in the 2x2 case.

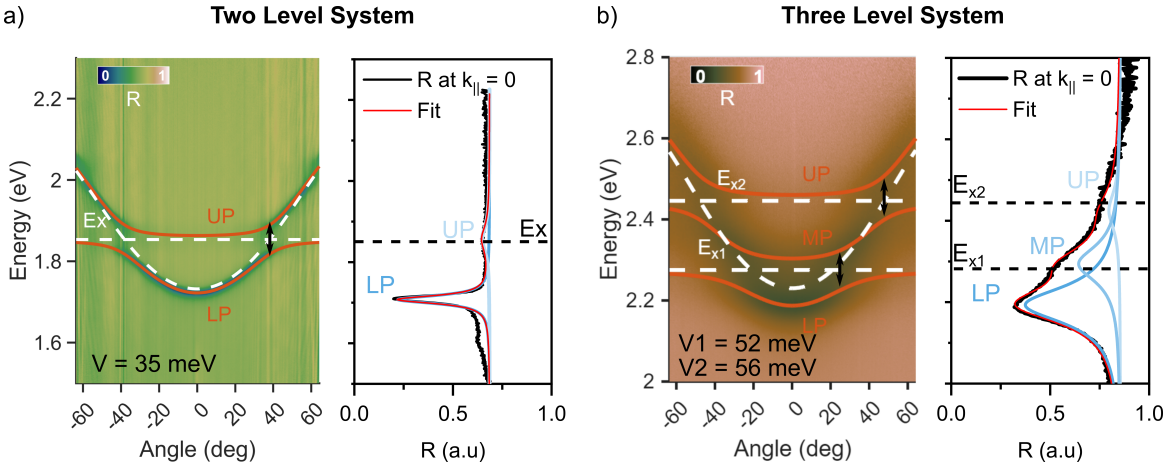

Figure 3.5. (a) Experimental angle-resolved reflectivity spectra (left) for the TAC trimer cavity, showing the UP and LP branches. The exciton energy (E_x) is indicated by a white dashed line. The red curves represent the polariton dispersion obtained from fitting a 2x2 CHO model. The coupling strength V is also indicated. Right panel: Reflectivity spectrum at normal incidence ($k_{||} = 0$) with the corresponding two-peak Lorentzian fit (red). (b) Experimental angle-resolved reflectivity spectra (left) for the butyl-TFTAP cavity, showing UP, MP and LP polariton branches. The two exciton energies (E_{x1} and E_{x2}) are shown as white dashed lines. Red curves indicate the polariton dispersion fitted using a 3x3 CHO model. The coupling strength V_1 and V_2 are also indicated. Right panel: Normal-incidence reflectivity spectrum with a three-peak Lorentzian fit (red), showing the individual polariton modes.

The extracted polariton energies were fitted to the eigenvalues of the 3x3 Hamiltonian (Equation 3.1) to determine the coupling strengths V_1 and V_2, as well as the cavity mode energy at normal incidence $E_c(0)$. These fitted parameters allowed quantification of the coupling strength between the cavity and each excitonic transition, and were used to verify the system's position in the strong coupling regime.

4. Strong light-matter coupling with peri-functionalised tetraazaperylenes

This chapter investigates the strong light-matter coupling of newly synthesised peri-functionalised tetraazaperylenes in a Fabry-Perot cavity, representing the first exploration of this material class for this application. These TFTAP derivatives are characterised by a central N-heteropolycycle, forming the basis for a new class of highly emissive dyes. Here, the formation of exciton-polaritons is demonstrated through angle-resolved reflection and PL measurements. The energy and linewidth of the polariton branches can be tuned by adjusting the thickness of the cavity and the concentration of the fluorophores.

Parts of this chapter were previously published as T. Wesp, P. Valsalan, A. Kochan, M. Hertzog, H. Wadepohl, J. Zaumseil, L. H. Gade, Chem. Eur. J. 2022, 28, e202202661. [78] The three thioether-functionalised tetraazaperylenes, including butyl-, benzyl-, and p-methoxybenzyl substituted derivatives, were synthesised and optically characterised in solution by Dr. Tobias Wesp.

4.1 Introduction

Strong light–matter coupling at room temperature has been demonstrated with various organic excitonic materials, including perylene diimides (PDI), which are widely studied for their high oscillator strength, tunable optical properties, and high PLQY. [107] These features make PDIs well-suited for achieving strong coupling in optical microcavities. However, in solid-state environments and at higher concentrations—conditions often required to enhance coupling strength—PDIs tend to aggregate. This aggregation leads to the formation of non-emissive H-aggregates and broadened exciton linewidths, which diminish their optical performance and limit their effectiveness in strong-coupling applications. [199] These limitations motivate the search for alternative materials that retain high oscillator strength and PLQY while reducing aggregation tendencies in the solid state.

Tetraazaperylenes are structurally similar to PDI but incorporate four nitrogen atoms within their aromatic framework [120]. Independent modification of both the peri (Y) and

bay (X) positions of the tetraazaperylene core (see Figure 4.1 (a)) through nucleophilic substitution and/or metal-catalysed coupling reactions is possible. This versatility in functionalisation enables fine-tuning of their optical and electronic properties, [131,200] potentially mitigating the aggregation issues observed in PDI and making them attractive for strong light-matter coupling applications. While tetraazaperylenes have demonstrated potential for their application as cellular fluorescent markers, [128] their potential for strong light-matter coupling remains unexplored to date.

This research represents the first demonstration of the strong coupling behaviour of newly synthesised TFTAP derivatives. Wesp et al. [131, 200] successfully synthesised a series of tetraazaperylene derivatives functionalised in the peri-position. This study focuses specifically on three TFTAP derivatives – butyl-, benzyl-, and PMB-substituted tetraazaperylenes (see figure 4.1 (b-d)) selected for their high PLQY, good solubility in polystyrene matrices, and compatibility with solution processing.

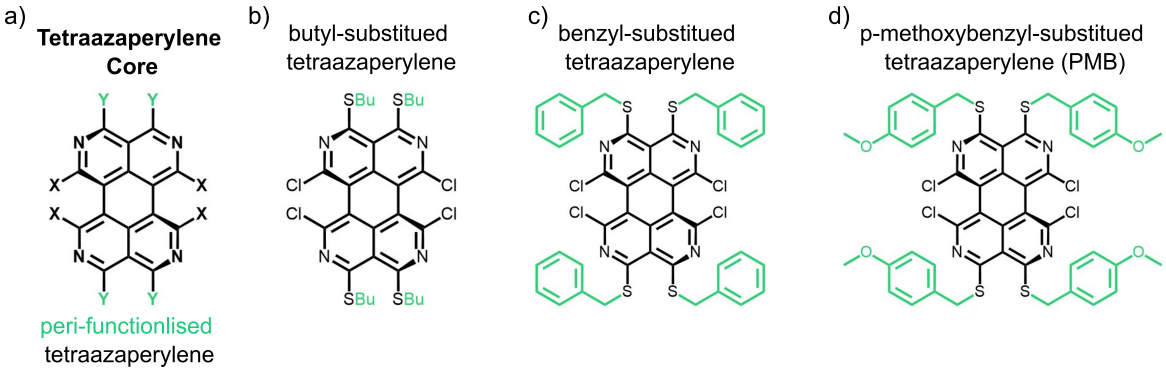

Figure 4.1. a) Generalised structure of tetraazaperylene derivatives. The molecular structures of the TFTAP derivatives: b) butyl-, c) benzyl-, and d) PMB-substituted tetraazaperylene are also shown.

This chapter investigates the strong coupling behaviour of these TFTAP derivatives in metal-clad optical microcavities at room temperature. First, their photophysical properties are characterised. Then, the formation of exciton-polaritons in TFTAP-based microcavities is demonstrated using angle-resolved reflectivity and PL spectroscopy. Finally, the influence of cavity thickness and emitter concentration on the energy and Hopfield coefficients of the resulting polariton branches is systematically explored. This analysis reveals the tunability of TFTAP-based systems and highlights the potential of the PMB-substituted derivative for achieving high coupling strengths.

4.2 Photophysical properties of the TFTAP derivatives in a polymer matrix

In toluene, all three derivatives- butyl-, benzyl-, and PMB-TFTAP exhibited two dominant absorption peaks in the green spectral region, a weaker shoulder around 2.6 eV, and a strong UV absorption band at 3.7 eV. These peaks correspond to the 0-0 and 0-1 vibronic transitions of the lowest singlet excited state ($S_0 \rightarrow S_1$), a 0-2 vibronic shoulder, and an $S_0 \rightarrow S_2$ transition, respectively. These spectral features were preserved upon embedding the molecules into a PS matrix, suggesting minimal perturbation of their electronic structure by the host polymer (Figure 4.2).

However, subtle differences were observed in the relative intensities of the vibronic transitions between solution and PS matrix. In particular, while the butyl-substituted TFTAP displayed approximately equal intensity for the 0-0 (Ex_1) and 0-1 (Ex_2) transitions in the PS matrix, both benzyl- and PMB-substituted derivatives showed a pronounced enhancement of the 0-1 transition.

Figure 4.2 presents the normalised absorption and PL spectra for each derivative in solution and in the PS matrix. The absorption spectra in the PS films remained well-resolved. Emission spectra exhibited broader lineshapes and reduced vibronic resolution compared to solution, reflecting an increase in inhomogeneous broadening in the PS matrix. All derivatives displayed modest Stokes shifts, ranging from 110 to 200 meV (Table 4.1), with the largest shift observed for the PMB-substituted TFTAP. The films were prepared by dissolving the 5 mg/ml fluorophores in a PS/toluene solution, followed by stirring at 90°C and filtration through a 0.45 µm PTFE membrane. Spin-coating onto glass substrates produced uniform films with thicknesses in the range of 100–250 nm.

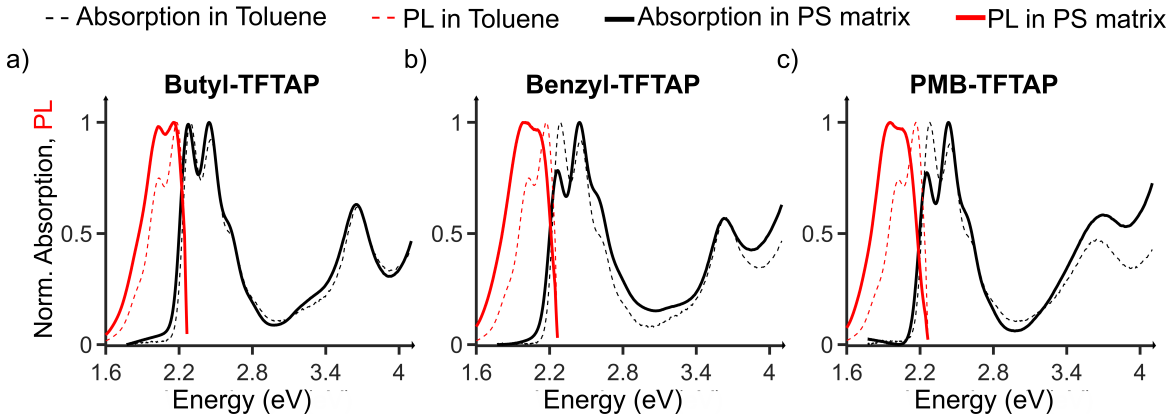

Figure 4.2. Normalised absorption and PL spectra of a) butyl-, b) benzyl-, and c) PMB-substituted TFTAP derivatives in both a PS matrix (solid lines, black for absorption and red for PL) and toluene solution (dashed lines, black for absorption and red for emission).

Table 4.1. Photophysical properties of TFTAP derivatives in PS matrix

Molecule	Ex_1 [eV]	Ex_2 [eV]	E_{em} [eV]	$\tau_{avg,amp}$ [ns]	Stokes Shift [meV]
butyl-	2.27	2.44	2.16	1.86	110
benzyl-	2.25	2.43	2.11	0.55	140
PMB-	2.25	2.42	2.05	0.60	200

Fluorescence decay profiles were collected using TCSPC and fitted with a bi-exponential model. The resulting amplitude-weighted average lifetimes are summarised in Table 4.1, and representative decay curves with residuals are shown in Figure 4.3. The butyl-substituted TFTAP exhibited the longest average lifetime (1.86 ns), whereas the benzyl- and PMB-substituted derivatives displayed shorter lifetimes of 0.55 ns and 0.60 ns, respectively. These differences are attributed to the nature of the substituents at the peri-position. The aliphatic butyl group is electronically decoupled from the conjugated core and thus does not significantly alter the excited-state landscape. In contrast, the aromatic benzyl and PMB substituents may introduce additional non-radiative decay pathways or influence the electronic density on the chromophore core, resulting in faster excited-state relaxation.

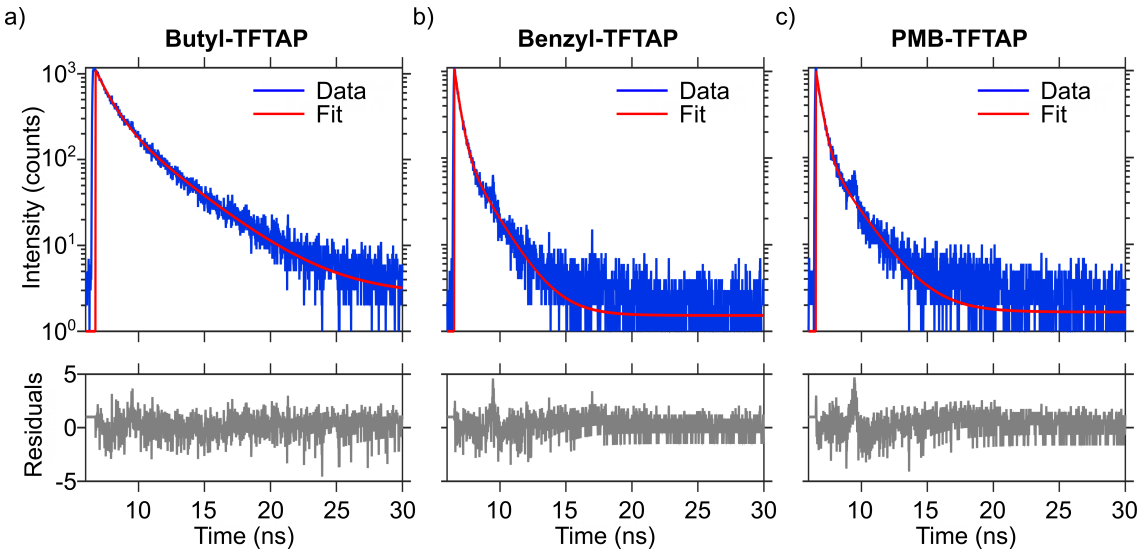

Figure 4.3. Time-resolved photoluminescence decay profiles of (a) butyl-, (b) benzyl-, and (c) PMB-substituted TFTAP derivatives in a polystyrene matrix. Blue lines represent experimental data; red lines show the corresponding bi-exponential fits. Residuals of the fits are shown below each decay curve. All measurements were performed on spin-coated films.

Wesp et al. had established that these TFTAP derivatives display high absorption coefficients, strong PLQY of up to 80%. [78] Collectively, the TFTAP derivatives demonstrate favourable optical characteristics for cavity integration. The retention of vibronic structure and spectral features upon incorporation into a polymer matrix confirms their compatibility

with solution processing. These properties, combined with excellent solubility and film-forming behaviour, establish TFTAPs as promising candidates for further investigation in strongly coupled optical microcavities.

4.3 Formation of exciton-polaritons in TFTAP-based microcavities

To investigate the potential of TFTAP derivatives for strong light–matter coupling, planar Fabry–Pérot microcavities were fabricated and characterised. Each cavity consisted of a spin-coated active layer composed of a PS matrix doped with 5 mg/mL of either butyl-, benzyl-, or PMB-substituted TFTAP derivatives. The active layer was positioned between two semi-transparent silver mirrors (35 nm thick), forming an optical resonator structure as illustrated in Figure 4.4 (a).

The use of PS as a host matrix enabled homogeneous film formation via spin coating, owing to its good solubility in toluene and compatibility with the TFTAP derivatives. Neat TFTAP films exhibited poor morphology and inhomogeneous optical properties, whereas dispersion in the PS matrix suppressed aggregation and produced uniform films with controlled thicknesses (100–250 nm, measured via profilometry). This control over thickness was essential for tuning the cavity resonance relative to the molecular excitonic transitions.

To facilitate strong coupling, the microcavity resonance was tuned to spectrally overlap with the dominant absorption bands of the TFTAP derivatives, specifically the vibronic 0-0 (Ex_1) and 0-1 (Ex_2) transitions around around 2.25–2.45 eV. When the optical cavity mode is brought into resonance with these excitonic transitions, hybridisation occurs, resulting in the formation of new hybrid eigenstates known as exciton-polaritons. As illustrated in Figure 4.4 (b), this interaction gives rise to three polariton branches: the UP, MP, and LP, emerging from the coupling of the cavity photon mode with two electronic transitions. The resulting energy splittings at the avoided crossings are quantified by coupling strengths V_1 and V_2, associated with Ex_1 and Ex_2, respectively.

The criterion for entering the strong coupling regime requires that the coupling strength exceeds the linewidths of the uncoupled exciton and photon modes. To assess this, the absorption spectra of the TFTAP derivatives embedded in PS matrix were fitted using a Pseudo-Voigt model, accounting for both homogeneous and inhomogeneous broadening (Figure 4.5 (a–c)). These fits provided precise estimates of the exciton peak positions and FWHM values for the Ex_1 and Ex_2 transitions.

In parallel, the reflectance spectrum of an uncoupled (dye-free) cavity was recorded and fitted with a Lorentzian function to determine the bare cavity mode energy and its corre-

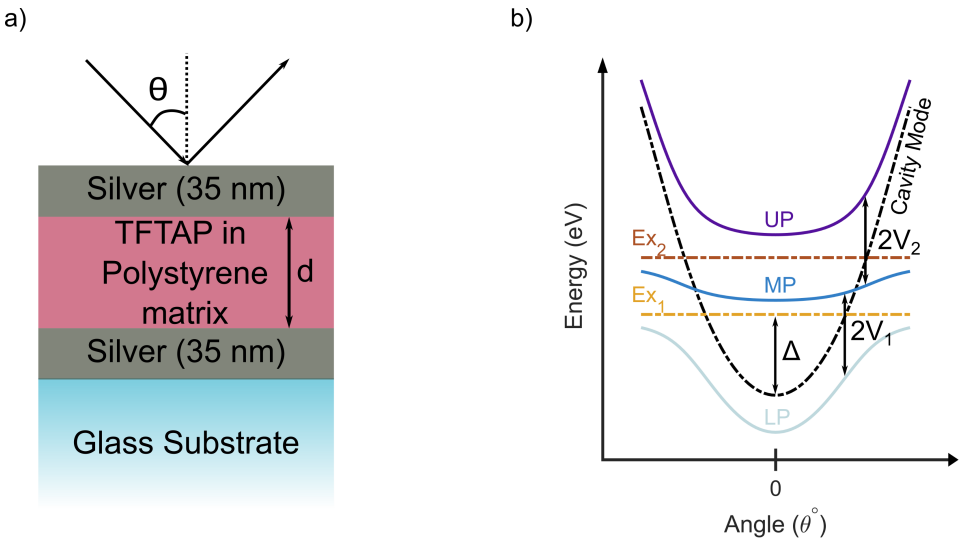

Figure 4.4. a) Schematic of a metal-clad microcavity with a thickness d and semi-transparent silver mirrors. b) Energy dispersion relations of uncoupled excitons and cavity photons in a strongly coupled system forming UP, MP and lower LP branches. The detuning Δ (depending on cavity thickness (d) and coupling strengths V_1 and V_2 at the avoided crossing points are shown.

sponding FWHM (Figure 4.5 (d)). The cavity resonance centred at 2.37 eV with a linewidth of 112 meV yields a quality factor (Q) of approximately 21, which is typical for silver-based microcavities. [12]

The extracted FWHM values are summarised in Table 4.2. Exciton linewidths ranged from 142 to 158 meV, values that are typical for organic semiconductors in solid-state environments. The cavity linewidth was consistently measured at 112 meV across all samples. These linewidths, when compared to the extracted coupling strengths, confirm that the system operates in the strong coupling regime.

Table 4.2. Extracted FWHM values of excitonic transitions (Ex_1, Ex_2) for the TFTAP derivatives and cavity mode (E_c)

	FWHM		
Molecule	Ex_1 [meV][a]	Ex_2 [meV][a]	E_c [meV][b]
butyl-	142	151	112
benzyl-	153	155	112
PMB-	158	156	112

Note: a) The molecular absorption spectrum is fitted using a Pseudo-Voigt model. b) Cavity mode has been fitted using a Lorentzian.

To experimentally observe exciton–polariton formation, angle-resolved reflectivity and PL measurements were conducted using a custom-built Fourier imaging setup (Section 3.4).

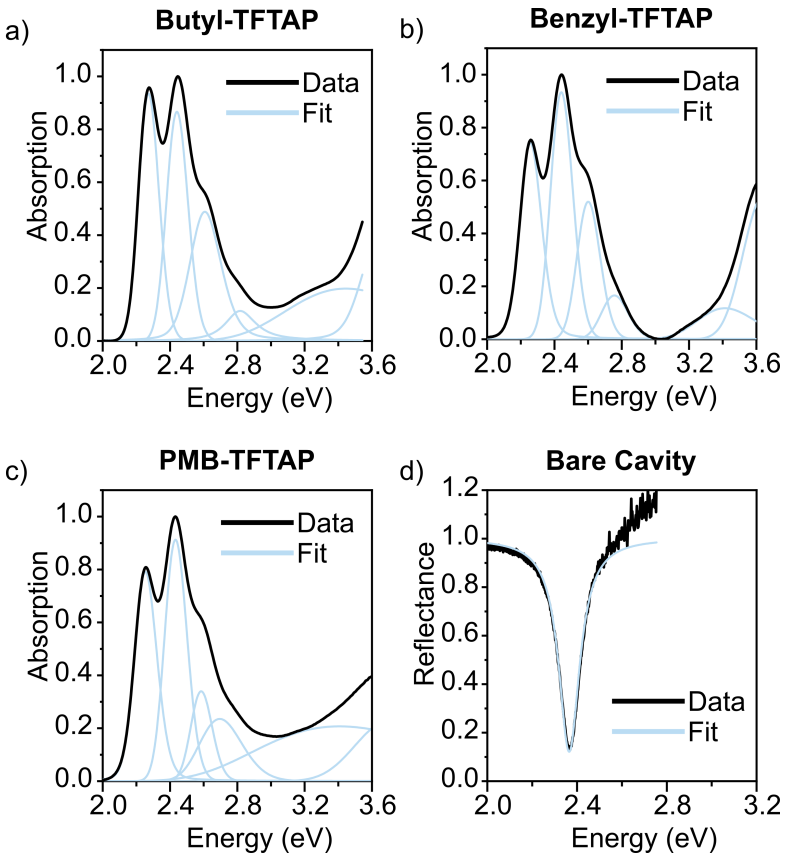

Figure 4.5. Normalised absorption spectra (black) and corresponding fits (blue) for (a) Butyl-, (b) Benzyl-, and (c) PMB-TFTAP embedded in PS matrix. The molecular absorption features were fitted using a Pseudo-Voigt model, with individual components shown in light blue. (d) Reflectance spectrum (black) of a bare cavity mode, fitted with a Lorentzian function (blue) to extract the cavity mode energy and linewidth.

The angle-resolved spectra were analysed using a CHO model based on a 3x3 matrix Hamiltonian, which describes the interaction between a single cavity photon mode and two molecular excitons. The model, implemented in MATLAB (Section 3.5.2), was fitted to both reflectivity and PL data to extract coupling strengths (V_1, V_2), and detuning (Δ).

Figure 4.6 (a–c) displays the angle-resolved reflectivity and PL spectra for microcavities incorporating the butyl-, benzyl-, and PMB-substituted TFTAP derivatives, respectively. The appearance of two avoided crossings, each corresponding to coupling between the cavity mode and one of the two vibronic excitonic transitions, confirms the formation of hybrid polariton modes. The experimental data align closely with the polariton dispersions predicted by the CHO model (solid lines), validating the extracted coupling parameters. A pronounced emission is exhibited by LP branches in the PL spectra (Figure 4.6 (a-c)). The extracted coupling strengths varied across the derivatives, with values of V_1 and V_2 ranging from 42 meV to 88 meV.

Figures 4.6 (d–f) present the corresponding Hopfield coefficients as a function of inci-

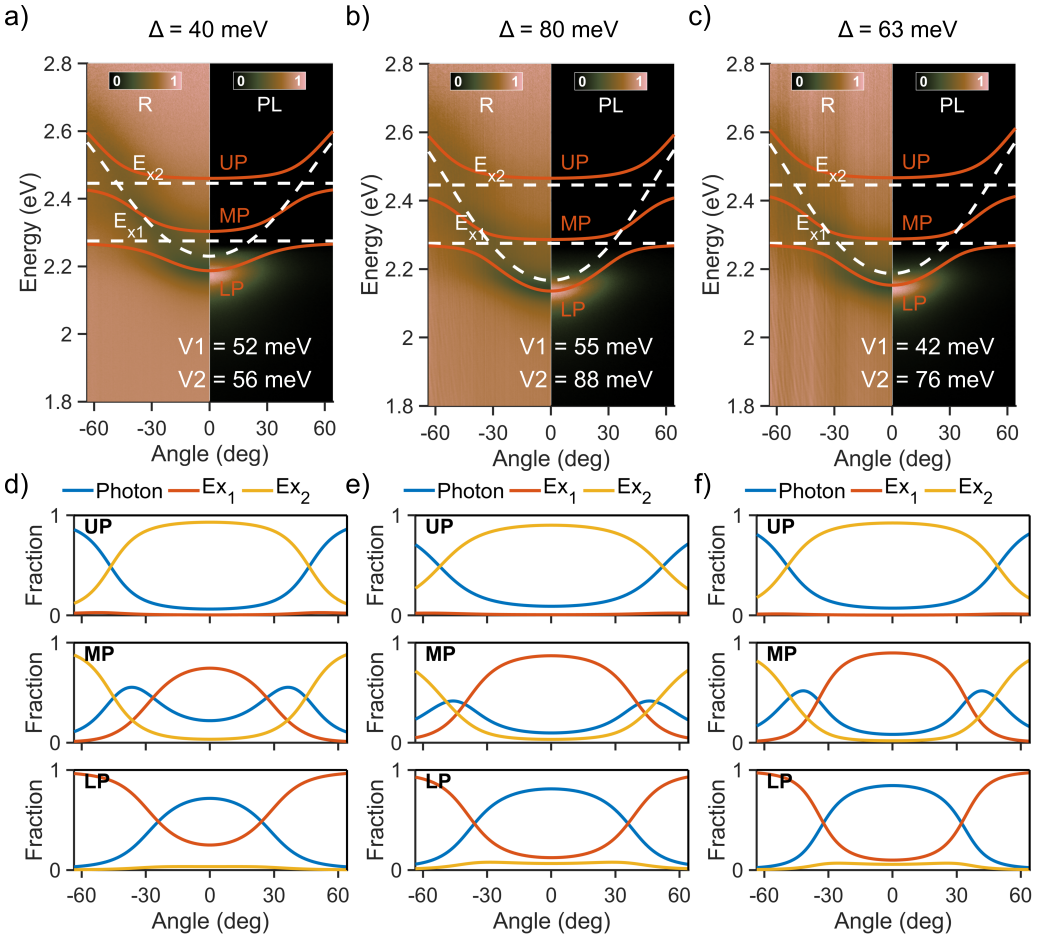

Figure 4.6. Angle-resolved (a-c) reflection and PL spectra of (a) butyl-, (b) benzyl-, and (c) PMB- substituted derivatives in a PS matrix in a metal-cladded microcavity. The polariton modes and cavity dispersion (white dashed lines), along with excitonic energies (Ex_1 and Ex_2 - white dashed lines), are displayed. The detuning (Δ) and coupling strengths (V_1 and V_2) are provided. (d-f) Hopfield coefficients of the respective systems with (d) butyl-, (e) benzyl-, and (f) PMB- substituted derivatives are displayed, along with the photon fraction (blue line) and the two exciton fractions (yellow and orange lines) of UP, MP, and UP.

dent angle. These coefficients quantify the fractional contributions of the cavity photon and the two excitons to each polariton state. As expected, the LP becomes increasingly photonic at larger angles, while the middle MP exhibits a mixed exciton–photon character, with a balanced contribution of Ex_1, especially near zero detuning. The UP remains more excitonic across the angular range.

Together, these results confirm that all three TFTAP derivatives, when embedded in PS matrix and integrated into metal-clad Fabry–Pérot microcavities, exhibit signatures of strong light–matter coupling forming three polariton branches whose energies and Hopfield coefficients are tunable via the molecular structure and cavity parameters. The variation in coupling strength among the TFTAP derivatives further highlights the role of chemical

substitution in modulating excitonic properties and cavity interactions.

4.4 Tuning exciton-polariton properties

The properties of exciton–polaritons in optical microcavities can be tailored by modifying key parameters that influence light–matter interactions. Two principal factors govern this tunability: the spectral detuning between the cavity mode and the molecular excitons, controlled by the optical path length of the cavity, and the concentration of emitters, which dictates the collective coupling strength. In this section, both parameters are systematically explored using microcavities incorporating PMB substituted TFTAP as the active material. This derivative was selected due to its high solubility in toluene and its compatibility with spin-coating, which enables controlled variation in both film thickness.

4.4.1 Effect of cavity thickness on detuning

To examine how changing the cavity thickness tunes the spectral position of the cavity mode relative to the excitonic transitions, thereby modifying the detuning Δ, a series of PMB-TFTAP based microcavities were fabricated with increasing active layer thicknesses, while maintaining the emitter concentration constant at 10 mg/ml.

Figure 4.7 presents the resulting angle-resolved reflectivity and PL spectra, along with the extracted Hopfield coefficients, for three representative cavity thicknesses: (a,d) ≈174 nm, (b,e) ≈182 nm, and (c,f) ≈212 nm. The corresponding Hopfield coefficients for the LP branch are also shown.

At a cavity thickness of 174 nm (Figure 4.7 (a)), the cavity mode is in resonance with the 0–0 excitonic transition (Ex_1) at normal incidence, yielding zero detuning (Δ=0 meV). Increasing the thickness to 182 nm and 212 nm redshifts the cavity mode, resulting in detunings of 23 meV and 73 meV, respectively. These shifts displace the LP branch further below the exciton energy and increase its photonic content near normal incidence.

The PL emission consistently originates from the LP branch across all samples, with the emission minimum shifting to lower energy with increasing positive detuning. The Hopfield coefficient plots (Figure 4.7 (d–f)) confirm that as the detuning becomes more positive, the LP branch exhibits a higher photon fraction near normal incidence. In contrast, the excitonic contributions dominate at larger angles. Notably, the coupling strengths V_1= 87 meV and V_2= 130 meV remain constant across all samples, indicating that cavity thickness modifies only the spectral alignment, not the fundamental light–matter interaction strength.

These results demonstrate that cavity detuning, controlled through film thickness, provides an effective means of tuning the energy and composition of exciton–polariton branches

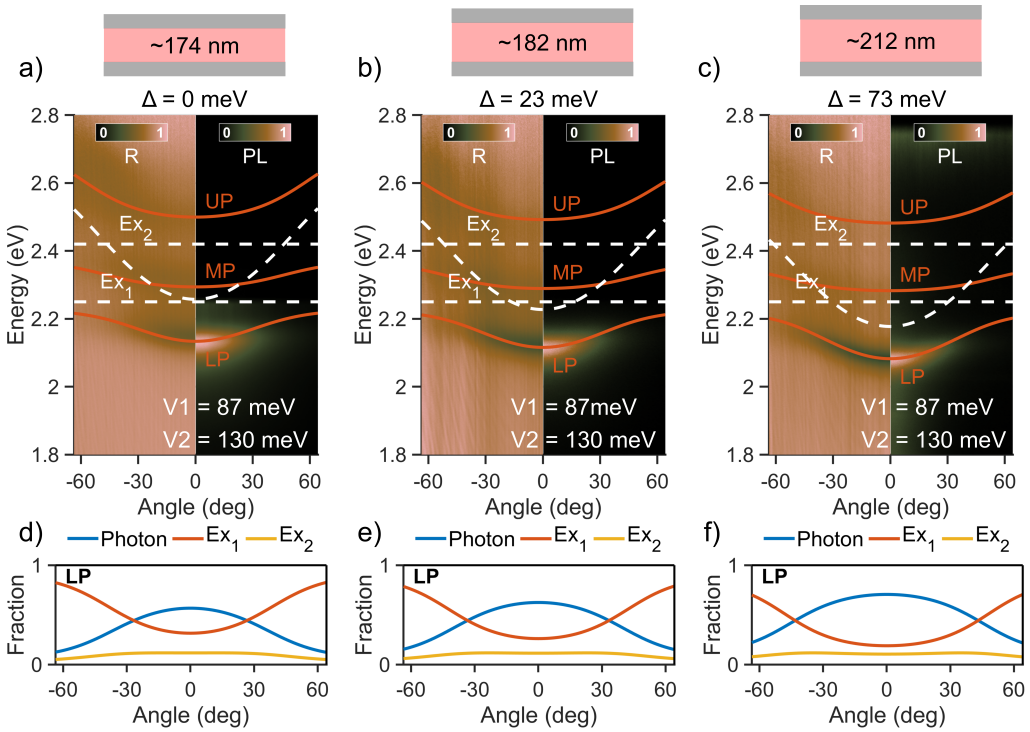

Figure 4.7. Angle-resolved reflectivity and PL) spectra of PMB- substituted derivatives (at 10 mg/ml concentration in solution) in PS matrix in metal-cladded microcavity for increasing cavity thickness d ≈ a) 174 nm, b) 182 nm and c) 212 nm are displayed from left to right. d) e) f) shows the respective Hopfield coefficients of the LP branch of the respective cavities.

without altering the coupling regime.

4.4.2 Effect of emitter concentration on coupling strength

To investigate how the strength of light–matter interaction can be tuned, the concentration of PMB-TFTAP in the PS matrix was varied. This is advantageous because higher emitter concentrations generally lead to stronger coupling strengths, as the collective light–matter interaction scales with the square root of the number of emitters. [12] In some systems, increasing concentration has even enabled access to the ultra-strong coupling regime, where the coupling strength exceeds 10% of the exciton energy, [201, 202]. The focus here is on exploring tunable strong coupling through controlled variation of emitter concentration.

To explore this effect, microcavities were fabricated with PMB-TFTAP concentrations of 10, 20, and 30 mg/ml in PS matrix. The cavity structure was fabricated by first depositing a 35 nm silver bottom mirror, followed by spin-coating a toluene-based PMB-TFTAP/PS solution to form uniform active layers with thicknesses between 100 and 250 nm. A second 35 nm silver mirror was then deposited on top to complete the microcavity. Angle-resolved reflectivity and PL spectra were recorded for each concentration using the Fourier imaging

setup and the data were analysed using the CHO model.

Figure 4.8 shows the angle-resolved reflectivity and PL spectra for PMB-TFTAP-based microcavities with increasing dye concentrations: (a,d) 10 mg/ml, (b,e) 20 mg/ml, and (c,f) 30 mg/ml, along with the corresponding Hopfield coefficients of the LP branch.

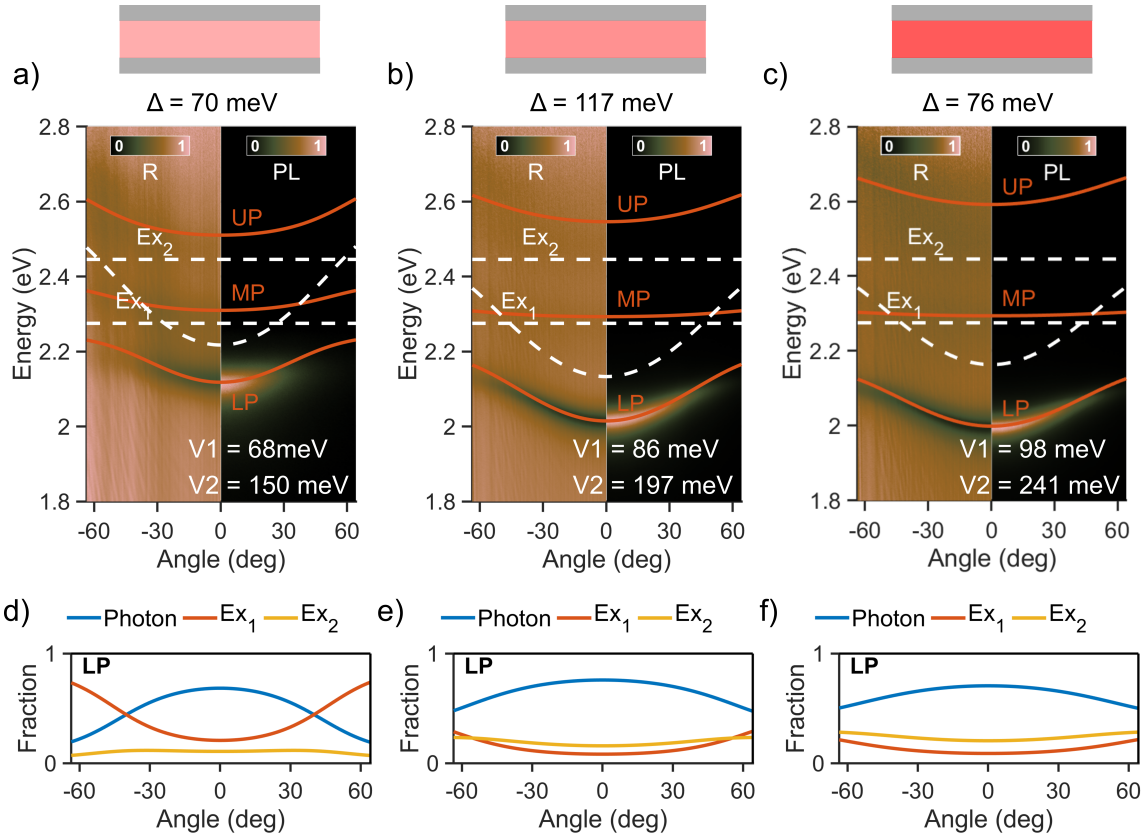

Figure 4.8. Angle-resolved reflectivity and PL spectra of PMB-substituted derivatives in a PS matrix within a metal-clad microcavity are shown for increasing PMB-substituted derivative concentrations: a) 10 mg/ml, b) 20 mg/ml, and c) 30 mg/ml in PS solution (from left to right). d) e) f) shows the respective Hopfield coefficients of the LP branch of the respective cavities.

As the dye concentration increases, the energy separation between polariton branches becomes larger as observed in the angle resolved reflectivity spectra (Figure 4.8 (a-c)). The fitted coupling strengths V_1 and V_2 increase from 68 meV / 150 meV at 10 mg/ml to 98 meV / 241 meV at 30 mg/ml. The detuning Δ also varies slightly across samples, due to minor changes in film thickness and refractive index, but remains within a range that preserves strong coupling. PL emission is consistently strongest from the LP branch.

The Hopfield coefficients (Figure 4.8 (d-f)) for the LP branch, indicating the relative contributions of the cavity photon and the two excitonic transitions across angles. The Hopfield coefficient analysis shows that the LP branch is predominantly photonic near normal incidence and becomes more excitonic at larger angles, consistent with positive detuning.

This angular trend remains similar across all concentrations. With increasing concentration, the coupling strength increases, which can enhance exciton-photon mixing and slightly raise the excitonic contribution to the LP branch. However, this trend is influenced by small variations in cavity detuning. At higher concentrations, the detuning becomes slightly more positive, which shifts the LP energy further from the exciton and increases its photonic character near normal incidence. As a result, the excitonic content of the LP branch does not vary monotonically with concentration but reflects a balance between stronger coupling and changes in detuning. These effects must be considered together when interpreting polariton composition across samples.

To confirm the expected square-root scaling of coupling strength with emitter density, the extracted values of V_1 and V_2 are plotted against the square root of the PMB-TFTAP concentration in Figure 4.9. Both values exhibit a linear dependence, confirming the expected scaling behaviour of strong light–matter coupling with emitter density. This trend reflects the collective nature of the coupling, where the interaction strength increases proportionally to $\sqrt{N}$, with N being the number of emitters. The coupling strength associated with the 0–1 vibronic transition (V_2) is consistently higher than that of the 0–0 transition (V_1), indicating a stronger interaction of the cavity mode with the higher-energy vibronic level. These results validate concentration as an effective tuning parameter for modulating coupling strength in organic microcavities.

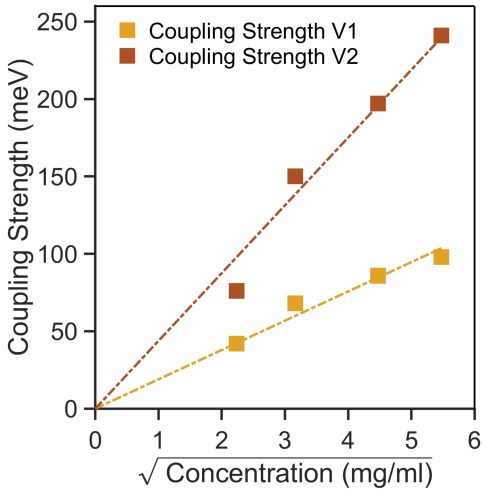

Figure 4.9. Coupling strengths V1 and V2 extracted from coupled oscillator fits versus the square root of the concentration of PMB in PS matrix, indicating the expected scaling behaviour for strong coupling with the number of emitters in the cavity.

4.5 Discussion and conclusion

This chapter presents the first demonstration of strong light–matter coupling with TFTAP derivatives in metal-clad microcavities. All three derivatives—Butyl-, Benzyl-, and PMB-TFTAP—exhibited clear polariton formation, with coupling strengths ranging from 40 to 241 meV.

The ability to systematically tune polariton properties was demonstrated by two complementary approaches. First, variation of the cavity thickness allowed control over the spectral detuning, which in turn modulated the energy and composition of the polariton branches without affecting the underlying coupling strengths. Second, adjustment of the PMB-TFTAP concentration in the PS matrix enabled direct modulation of the coupling strength, with extracted values showing the expected $\sqrt{N}$ scaling with emitter concentration.

Collectively, these results highlight the potential of TFTAP derivatives as a new class of solution-processable, highly emissive chromophores for strong coupling applications. Their structural tunability, excellent solubility, and well-defined excitonic transitions make them highly versatile candidates for organic photonic and polaritonic devices. The findings contribute to a growing body of work on molecular materials that support coherent light–matter interactions under ambient conditions and demonstrate how subtle variations in molecular structure and device architecture can be leveraged to manipulate hybrid states of light and matter.

5. Polariton population in tetraazacoronene-based cavities

This chapter focuses on polariton emission pathways following optical excitation for varying detuning in organic microcavities with a Tetraazacoronene (TAC) trimer, where the linewidths are exceptionally narrow, the Stokes shift is very small, and the vibronic progression is very well resolved. Such well-resolved energetic levels enable a detailed analysis of the relaxation mechanisms from the exciton reservoir to the LP mode. Specifically, the roles of RP and VAS in LP population were investigated through angle-resolved reflectivity and PL measurements were performed on microcavities with varying detuning.

The TAC trimers were synthesised and optically characterised in solution by Dr. Robert Eichelmann. [144]

5.1 Introduction

The LP population plays a central role in the optical response and functionality of strongly coupled organic microcavities, underpinning phenomena such as Bose–Einstein condensation, polariton lasing, and cavity-mediated long-range energy transfer. [14, 162] For example, efficient LP population is a prerequisite for achieving lasing in organic crystals like anthracene, [14], and it governs the spatial energy redistribution observed in donor–acceptor cavity systems. [162] Under non-resonant excitation schemes, relaxation from the exciton reservoir (ER) into LP states proceeds via multiple pathways, most notably radiative pumping (RP) and vibrationally assisted scattering (VAS). These mechanisms have been described in detail in section 2.6, which outlines how their efficiency depends on molecular properties such as Stokes shift, vibronic coupling strength, and PLQY, as well as cavity parameters like detuning and Rabi splitting.

This chapter explores polariton population pathways in a cavity system incorporating a TAC trimer, with particular focus on how RP and VAS manifest in systems with well-resolved vibronic structure. The TAC trimer was chosen due to its advantageous properties that align with the requirements for strong light–matter interaction, such as narrow excitonic

linewidths, distinct vibronic progression, high absorption coefficients, and a small Stokes shift, features that facilitate strong light–matter coupling and may allow systematic evaluation of the conditions under which RP and VAS contribute to LP population.

The TAC trimer was synthesised via Zr-mediated cyclisation and four-fold Suzuki-Miyaura cross-coupling of bay-functionalised tetraazaperylenes, as described by Eichelmann et al. [144]. The molecular structure is shown in Figure 5.1 (a). In toluene solution and within a PS matrix, the TAC trimer exhibits a clearly resolved vibronic structure, including a dominant 0-0 transition (S_{01}) and its 0–1 vibronic replica. The 0-2 transition is also observed at higher energy but is comparatively weak and excluded from further analysis. The emission spectra also retain this vibronic resolution, with small Stokes shifts of 2–3 meV in both media and high PLQY values (up to 80% in solution, [144] and 30% in PS). A summary of key photophysical properties is provided in Table 5.1, and spectral data are shown in Figure 5.1 (b).

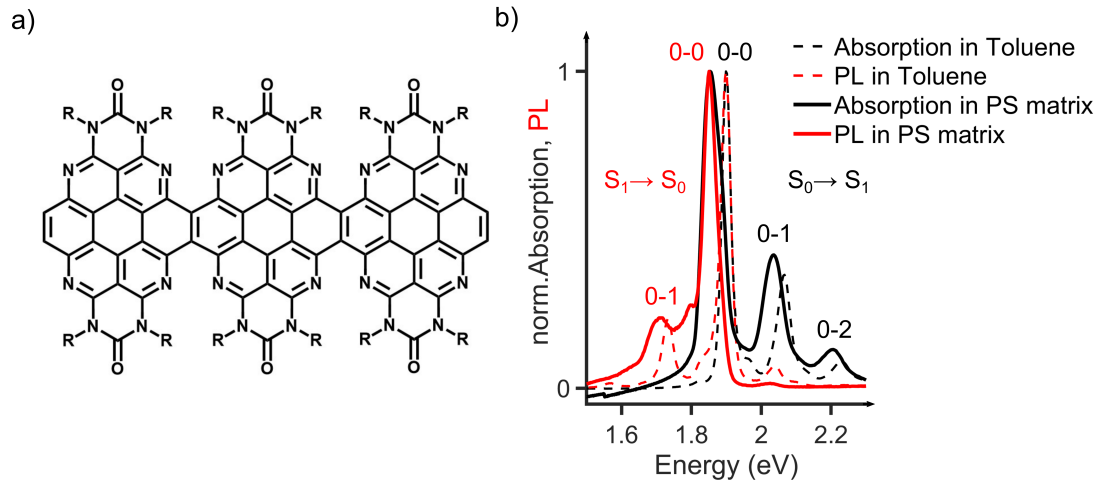

Figure 5.1. (a) The molecular structure of the TAC trimer. (b) Normalised absorption (black) and PL (red) spectra of the TAC trimer in toluene (dashed lines) and in a PS matrix (solid lines). The spectra reveal a well-resolved vibronic progression in both absorption (S_{01}) and PL (S_{10}), with the 0–0 and 0–1 transitions clearly visible.

Table 5.1. Comparative photophysical properties of TAC trimer in toluene and PS matrix

TAC trimer in	Absorption		Emission		Stokes Shift [meV]
	Ex_{00} [eV]	Ex_{01} [eV]	$E_{em,00}$ [eV]	$E_{em,01}$ [eV]	
Toluene	1.899	2.067	1.897	1.732	2
PS	1.854	2.036	1.851	1.708	3

Prior theoretical and experimental studies have highlighted the role of vibronic structure in shaping polariton emission. Mazza et al., through theoretical study and model analysis,

showed that vibronic replicas in molecular emitters could give rise to distinct features in the PL spectra of strongly coupled cavities. [167] Experimental observations in systems such as nanographene derivatives [15] and perylene diimides [107] have confirmed vibronic structure in polariton PL, with radiative pumping identified as a plausible population mechanism. Nevertheless, in many cases, the precise contribution of vibrationally assisted pathways has remained unclear. Polariton lasing in vibronically structured organic systems has also been widely reported, further underscoring the functional significance of vibrational structure in polaritonic devices. [8, 14–16] Notably, Kena-Cohen and Forrest demonstrated polariton lasing in anthracene single crystals, showing that lasing occurred only when the cavity detuning aligned the LP ground state with a molecular vibrational mode. [14] These findings strongly suggest that vibrational structure can mediate polariton population under specific spectral conditions, although the underlying relaxation mechanisms remain incompletely understood.

Polariton relaxation in organic microcavities can proceed via multiple competing pathways. [84, 203] The distinction between RP and VAS is illustrated schematically in Figure 5.2. In the RP mechanism, incoherent emission of photons from excitons in the uncoupled Stokes-shifted ER are absorbed by the photonic component of the LP mode. [84, 203] Because this process originates from spontaneous molecular emission, the resulting LP PL spectrum often closely mirrors the shape of the uncoupled molecular PL spectrum. The efficiency of RP is strongly influenced by the photonic Hopfield coefficient of the LP state and the spectral overlap between the LP dispersion and the molecular emission profile. [84, 164, 203] In contrast, VAS involves phonon-mediated relaxation processes, where excitons in the ER scatter into the LP manifold via the emission of low-energy vibrational quanta. [84] This mechanism arises through intermolecular exciton–phonon coupling, and can be particularly prominent when the energy difference between the ER and the LP matches the energy of a Raman-active vibrational modes of the molecule. [84, 162, 204] Both VAS and RP can contribute to exciton–polariton relaxation, with their relative importance depending on cavity detuning, [162] Rabi splitting energy, [204] Stokes shift, [203] and the strength of vibronic coupling. [84, 174] The complex vibronic structure inherent to many organic emitters gives rise to coexisting or competing population channels, with different relaxation pathways becoming active depending on how these variables are tuned. [84] Consequently, the TAC trimer represents a suitable model system for examining how vibrational structure shapes polariton population in a strongly coupled microcavity.

In this chapter, strong light–matter coupling in TAC trimer-based microcavity is demonstrated, with a coupling strength of up to 36 meV. Angle-resolved reflectivity and PL measurements are performed across a series of cavity detunings to examine the steady-state emission from the LP branch. This is followed by an analysis of the detuning-dependent

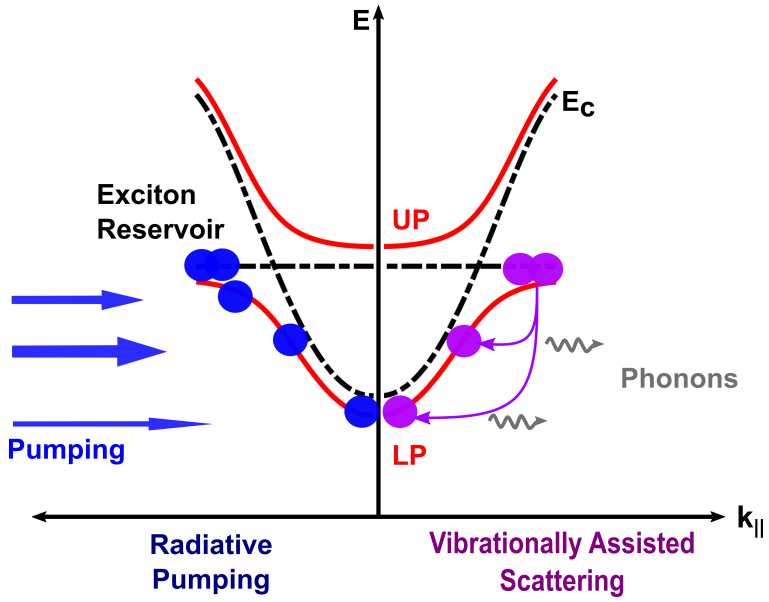

Figure 5.2. Schematic illustration of competing polariton relaxation pathways in an organic microcavity under non-resonant excitation. Excitons are generated in the ER (horizontal dashed line) and relax into the LP branch via two primary mechanisms: radiative pumping (left, blue), where photons emitted from the ER are absorbed into LP modes, and vibrationally assisted scattering (right, purple), where excitons transfer into the LP via phonon emission. The UP branch and the cavity photon mode (E_c) are shown for reference. The vertical axis denotes energy, while the horizontal axis corresponds to the in-plane wavevector ($k_{||}$).

LP population to investigate the role of RP in polariton relaxation. To further explore vibrationally assisted processes, the energies of Raman-active modes are compared with the energy differences between the exciton reservoir and the LP, providing insight into possible vibronically mediated scattering channels. While Raman peaks do not directly affect the LP emission, they help identify phonon energies that may participate in polariton relaxation. The combined analysis supports the conclusion that both RP and VAS contribute to the population of specific polariton modes in the TAC trimer system.

5.2 Strong coupling in TAC trimer-based microcavities

The microcavity structure was fabricated by first depositing a 100 nm silver bottom mirror via thermal evaporation onto an optically clean glass substrate. A 20 nm layer of Al_2O_3 was deposited by atomic layer deposition to improve the wettability of the silver surface. The active layer was prepared by spin-coating a solution of PS and TAC trimer in toluene, resulting in a film with a thickness of 350–450 nm, where the TAC trimer is embedded within the PS matrix. A 35 nm semi-transparent silver top mirror was then deposited to

complete the cavity. The optical properties of the TAC trimer film and the empty PS cavity were characterised prior to device assembly.

Figure 5.3 (a) shows the normalised absorption spectrum of the TAC trimer in the PS matrix (black), fitted with a sum of Voigt profiles (light blue). The 0–0 transition at 1.853 eV corresponds to the S_{01}, 0-0 transition and exhibits a FWHM of 52.65 meV. This is significantly narrower than that of the TFTAP derivatives discussed in Chapter 4. Angle-resolved reflectivity of the empty PS cavity (without emitters) is shown in Figure 5.3 (b), revealing the expected cavity dispersion. The normalised reflectivity spectrum at normal incidence ($k_{||} = 0$) is shown in Figure 5.3 (c), with a Lorentzian fit yielding a cavity photon linewidth of 18.3 meV. The minimum coupling strength required to achieve the strong coupling regime for this system is estimated as ($V = \frac{1}{4}(FWHM_{ex} + FWHM_c)$) 17.72 meV. The quality factor (Q) of the cavity is calculated to be 81, higher than that of the cavity used in Chapter 4, and within the typical range for metal-cladded cavities.

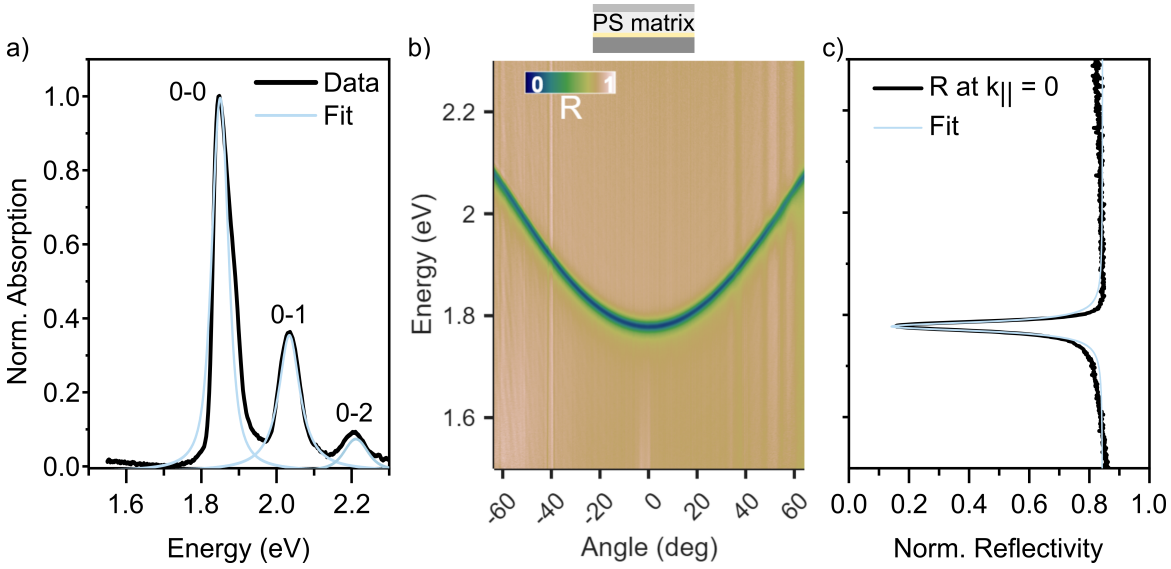

Figure 5.3. (a) Normalised absorption spectrum of the TAC trimer in a PS matrix (black line) fitted with a sum of Voigt functions (light blue). The 0–0, 0–1, and 0–2 vibronic transitions are clearly resolved. (b) Angle-resolved reflectivity spectrum of the empty PS cavity (no emitter), revealing the cavity dispersion as a function of incidence angle. The PS cavity structure is illustrated above the panel. (c) Normalised reflectivity at $k_{||} = 0$, fitted with a Lorentzian function (light blue), used to extract the cavity photon linewidth.

The schematic of the complete microcavity used in this study is shown in Figure 5.3 (a). Angle-resolved reflectivity and PL spectra in TE polarisation are presented in Figure 5.4 (b) for a detuning of 156 meV. The resulting spectra show distinct UP and LP branches with a clear anticrossing at the exciton energy, confirming that the system is in the strong coupling regime. A weak coupling between the cavity mode and the 0–1 vibronic transition of the

TAC trimer at 2.03 eV is also observed as a slight deviation in the dispersion; however, this interaction does not produce a resolvable anticrossing and does not meet the quantitative criterion for strong coupling. Consequently, this feature is not included in the CHO model, and the system is treated using a 2×2 Hamiltonian that includes only the 0–0 excitonic transition. The resulting coupling strength (V), extracted from the CHO fit (orange lines in Figure 5.3 (b)), is 36 meV. This value slightly exceeds the minimum threshold for strong coupling in this system, calculated as V > 17.72 meV based on the sum of the exciton and cavity mode linewidths. This confirms that the system is indeed in the strong coupling regime.

Hopfield coefficients obtained from the CHO model are shown in Figure 5.3 (c). These describe the exciton and photon fractions of the polariton states as a function of angle. At large angles, the LP is predominantly excitonic, while near $k_{||} = 0$ it becomes more photonic. At the resonance angle of 40°, where $E_x = E_c$, the LP and UP exhibit a balanced 50% exciton and 50% photon. The distribution of exciton and photon fractions along the polariton branches needs to be taken into account in order to calculate the population of polaritons from PL spectra, as will be demonstrated in the following section.

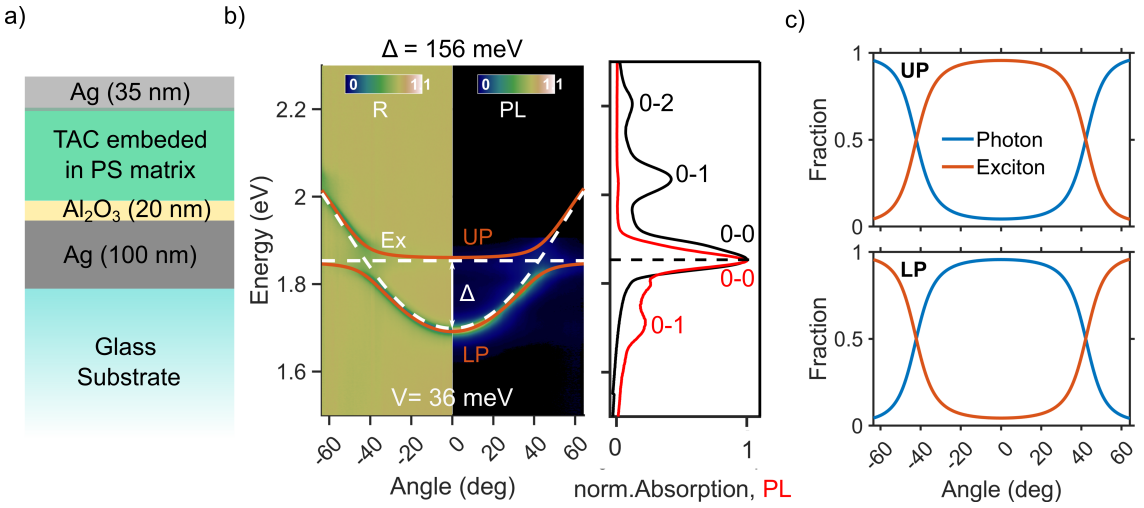

Figure 5.4. (a) Schematic of a metal-clad microcavity with TAC trimers embedded in PS matrix and semi-transparent (b) Angle-resolved reflectivity and PL spectra of TAC trimers in PS matrix in a metal-cladded microcavity. The polariton modes and cavity dispersion (white dashed lines), along with excitonic energies (E_x white dashed lines), are displayed. The detuning (Δ) and coupling strength (V) are provided. The right panel compares the normalised absorption (black) and PL (red) spectra, highlighting the vibronic transitions. (c) Hopfield coefficients for the UP (top) and LP (bottom) polariton branches, showing the angle-dependent exciton and photon fractions.

5.3 TAC trimer exciton-polariton PL as a function of detuning

To investigate how cavity detuning influences the emission characteristics of exciton-polaritons, angle-resolved reflectivity and PL measurements were performed across a series of detuned microcavities. The detuning was controlled via the natural thickness gradient of the spin-coated TAC trimer:PS film, which allowed sampling of 24 different cavity thicknesses ranging from 350 to 450 nm across the same substrate. Figure 5.5 presents representative angle-resolved reflectivity and PL spectra for eight selected cavity positions, selected to span a broad detuning range from –8 meV to 278 meV. These examples were chosen to illustrate changes in the polariton dispersion and PL intensity with increasing cavity thickness.

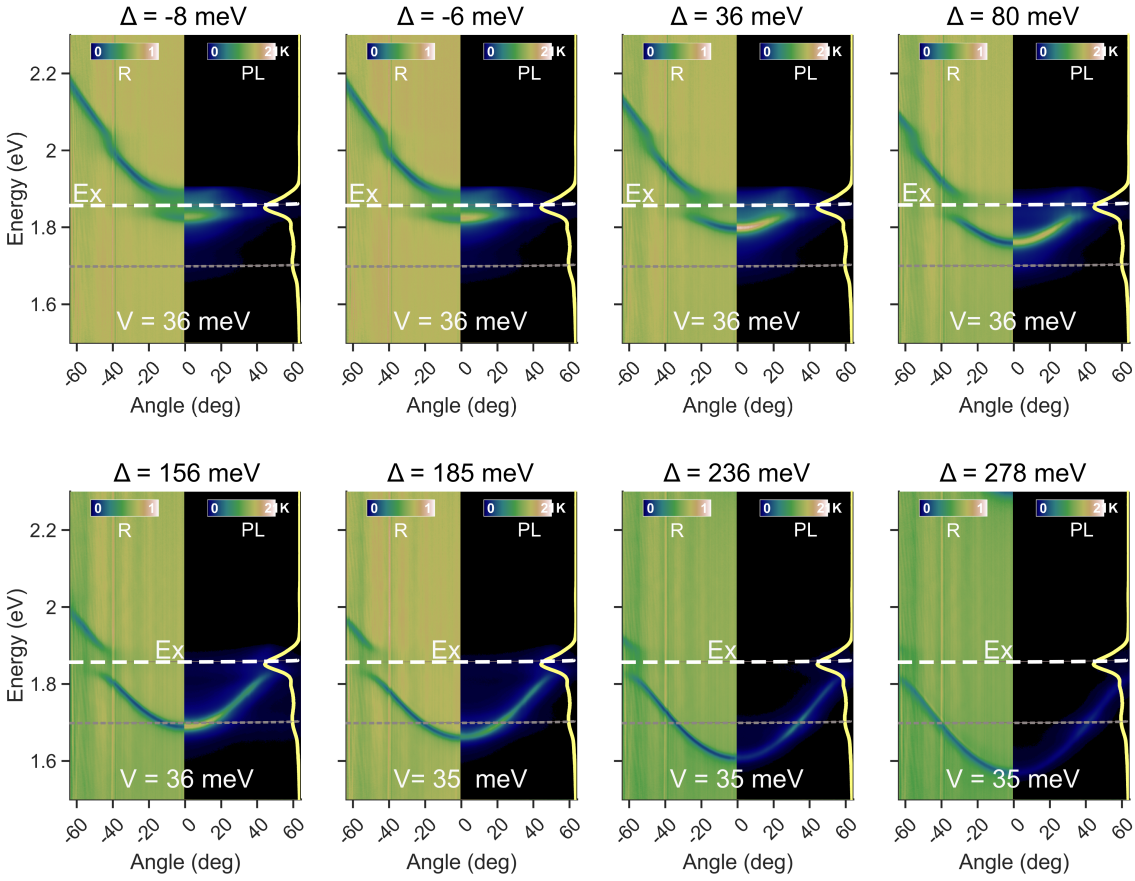

Figure 5.5. Angle resolved reflectivity and PL spectra of eight selected detunings of strongly coupled TAC trimer based cavity. The detuning Δ and excitonic energies (E_x, white dashed lines) are provided for each plot. The grey line is provided to guide the eye to the vibrational peak on the TAC trimer PL (yellow solid line).

A full set of angle-resolved reflectivity and PL spectra across all 24 detunings is shown in Figures 5.6 and 5.7. The white dashed lines mark the exciton energy (E_x), while the orange curves represent fits to the UP and LP dispersion using a 2x2 CHO model. The extracted

coupling strengths range from 35 to 36 meV and confirm that the system remains in the strong coupling regime throughout. At lower detunings (-8 to 36 meV), weak coupling spectral features near 2.03 eV, corresponding to the 0–1 vibronic transition, enter the reflectivity window, but, as noted earlier, the coupling is too weak to be included in the model.

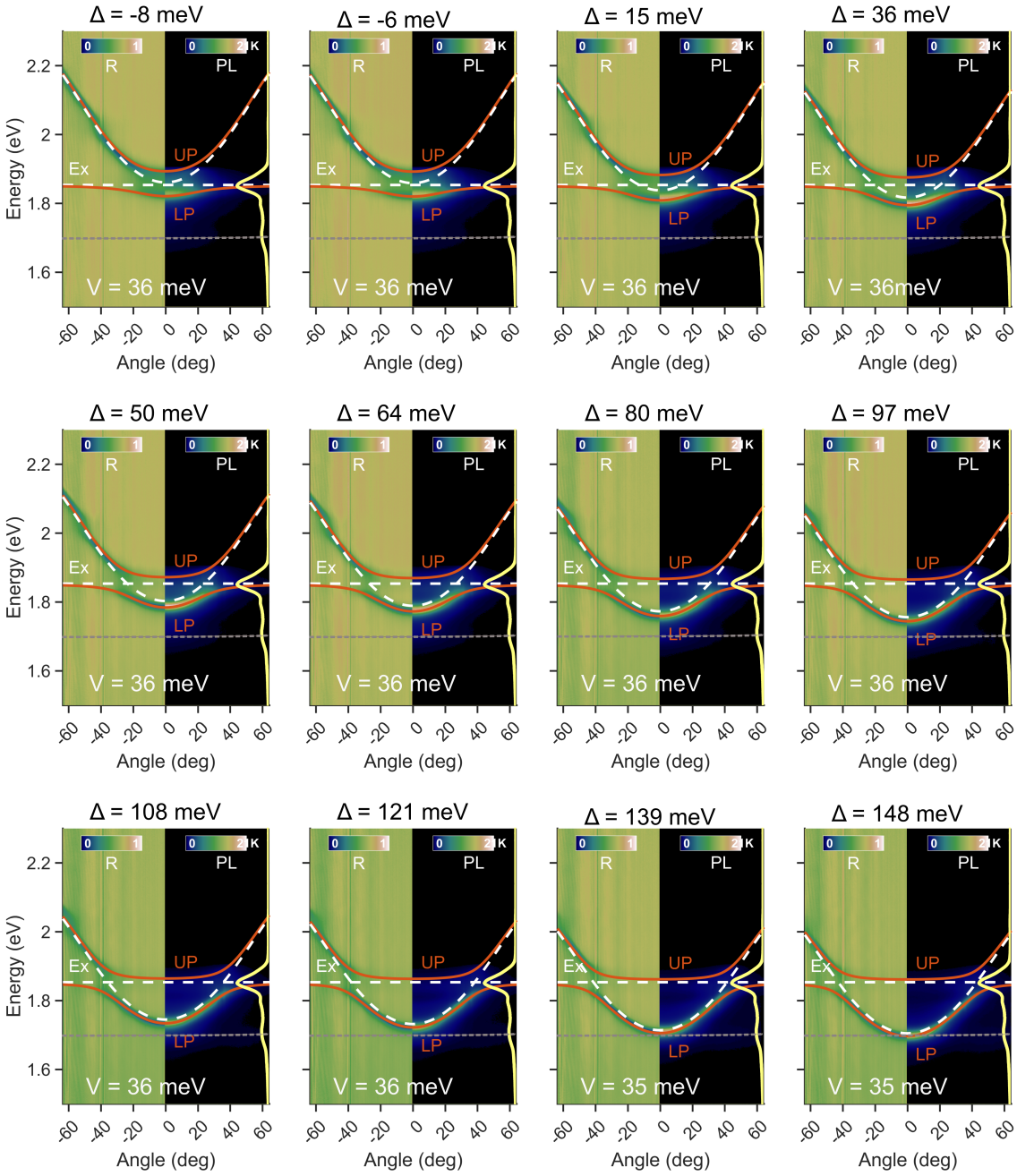

Figure 5.6. Angle resolved reflectivity and PL spectra of detunings in the range -8 eV to 148 meV of strongly coupled TAC trimer-based cavity. The polariton modes and cavity dispersion (white dashed lines), along with excitonic energies (E_x, white dashed lines), are displayed. The detuning (Δ) and coupling strength (V) are provided. The grey line guides the eye to different vibrational peaks on the TAC trimer PL (yellow solid line).

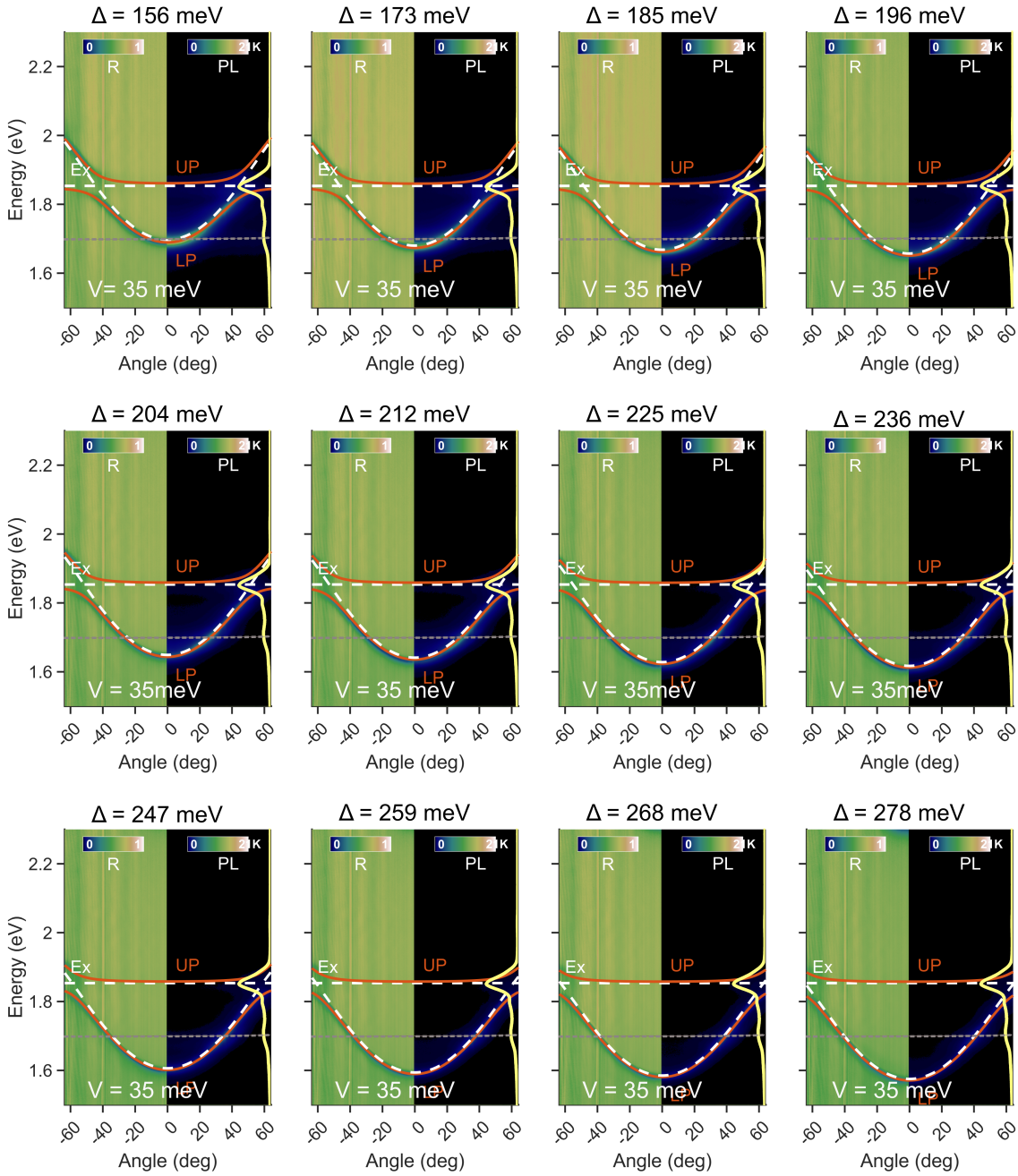

Figure 5.7. Angle resolved reflectivity and PL spectra of detunings in the range 156 meV to 278 meV of strongly coupled TAC trimer-based cavity. The polariton modes and cavity dispersion (white dashed lines), along with excitonic energies (E_x, white dashed lines), are displayed. The detuning (Δ) and coupling strength (V) are provided. The grey line guides the eye to different vibrational peaks on the TAC trimer PL (yellow solid line).

Emission is primarily observed from the LP branch. The angle-resolved PL spectra show intensity variations at different LP energies (see the grey line in Figure 5.5), with discrete maxima appearing at certain detunings. Figure 5.8 (a) shows the LP PL intensity at $k_{||} = 0$ as a function of LP energy and detuning. Each vertical column represents the LP PL spectrum at

a specific detuning, obtained by averaging the emission over ±1.5° around $k_{||} = 0$ for one of 24 cavity positions. The yellow line shows the PL spectrum of a TAC trimer reference film in a PS matrix, included for comparison. As detuning increases, the LP shifts to lower energies, and the PL intensity exhibits distinct variations, forming discrete maxima at specific energy values.

To better visualise these variations, Figure 5.8 (b) presents the measured LP PL intensity at $k_{||} = 0$ as a function of LP energy, shown in green. These values are not corrected for the photon content and represent the raw emission intensity from each LP state across the 24 detunings. The grey background shows the normalised PL spectrum of the uncoupled TAC trimer film. At normal incidence ($k_{||} = 0$), raw LP PL intensity varied with detuning and exhibited discrete maxima that partially align with the uncoupled TAC trimer PL spectrum. A more quantitative analysis of LP population, corrected using Hopfield coefficients at $k_{||} = 0$ for each detuning to account for the photonic component of the polariton, is presented in the following section.

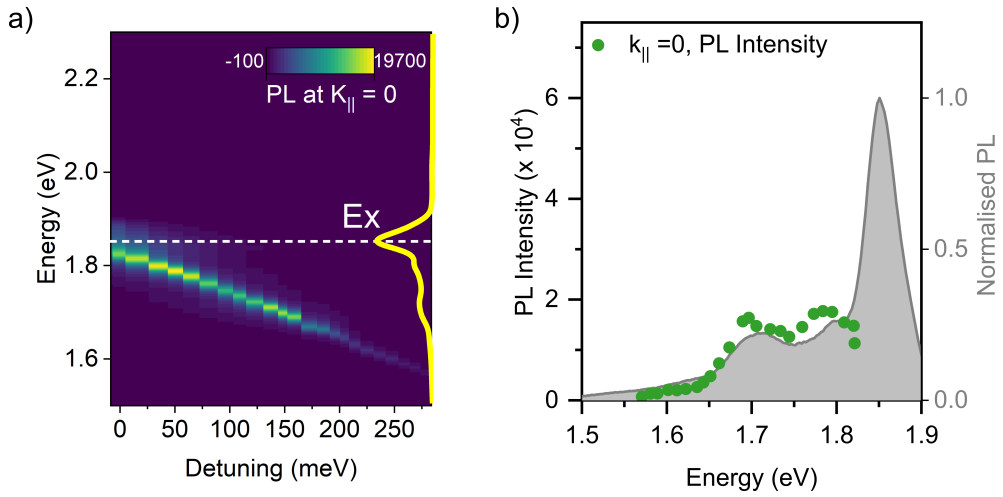

Figure 5.8. a) Change in LP PL intensity at $k_{||} = 0$ as a function of detuning for TAC trimer exciton-polaritons is presented. The yellow line represents the PL spectra from a TAC trimer embedded in a PS matrix reference film for comparison. (b) LP PL intensity as a function of LP position in the microcavity, compared to the TAC trimer reference film's PL spectrum.

5.4 Polariton population analysis across detuning

To evaluate the relaxation pathway responsible for populating the LP states, the observed PL intensities at $k_{||} = 0$ were corrected for two key factors: the photonic fraction of each polariton state and the variation in excitation efficiency across detunings. Since the measured PL intensity arises from the photonic component of the LP, the raw intensity values were

divided by the Hopfield coefficient at $k_{||} = 0$ for each detuning to estimate the relative LP population. Additionally, the excitation efficiency was corrected using the electric field distribution at the excitation energy $E_{pump} = 1.94$eV (640 nm), which corresponds to the energy of the laser used for non-resonant excitation of the TAC trimer microcavity in the experiment. The electric field intensity at this energy varies with detuning, and must be accounted for to compare LP populations across detunings accurately.

To quantify the excitation efficiency correction, the electric field intensity at the excitation energy ($E_{pump} = 1.94$eV) was calculated using TMM simulations. These simulations were first validated against experimental data: Figure 5.9 (a) compares the experimental (left) and TMM-simulated (right) angle-resolved reflectivity spectra of a TAC trimer microcavity with a detuning of 121 meV, showing excellent agreement. The corresponding electric field intensity at $k_{||} = 0$ is shown in Figure 5.9 (b), with individual cavity layers indicated by coloured lines and the excitation energy marked by a dashed black line.

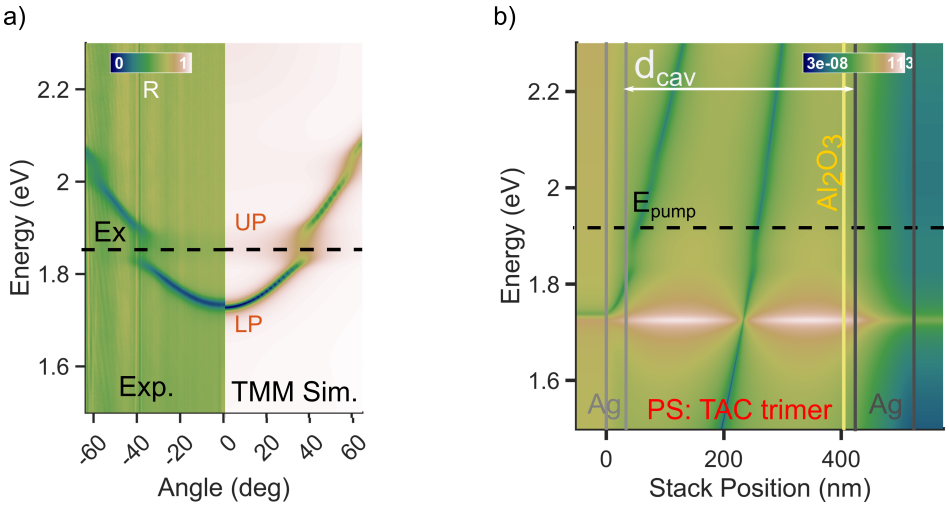

Figure 5.9. (a) Experimental and simulated angle-dependent reflectivity spectrum of the microcavity with a detuning of $\Delta = 121$ meV. The exciton energy ($E_x = 1.853$eV) of the TAC trimer is marked by the black dashed line. (b) Electric field intensity of the photonic component of the polariton at $k_{||} = 0$ in the microcavity ($\Delta = 121$ meV) from TMM calculations. The materials in the device stack are indicated by vertical lines, and the excitation energy ($E_{pump} = 1.94$eV) is marked by the black dashed line.

The PL spectra for all detunings were acquired with an excitation energy of 1.94 eV (640 nm) at a laser power of 10 mW and an integration time of 0.1 s. Figure 5.10 shows the TMM simulated electric field intensity at the excitation energy of 1.94 eV (640 nm) at $k_{||} = 0$ for 8 out of the 24 detunings from -8 meV to 278 meV. The electric field intensity at this excitation energy decreases as the detuning increases for the TAC trimer microcavity. The red shaded area highlights the E-field intensity within the TAC trimer layer across varying detunings.

To calculate the excitation efficiency correction factor, the electric field intensity at the

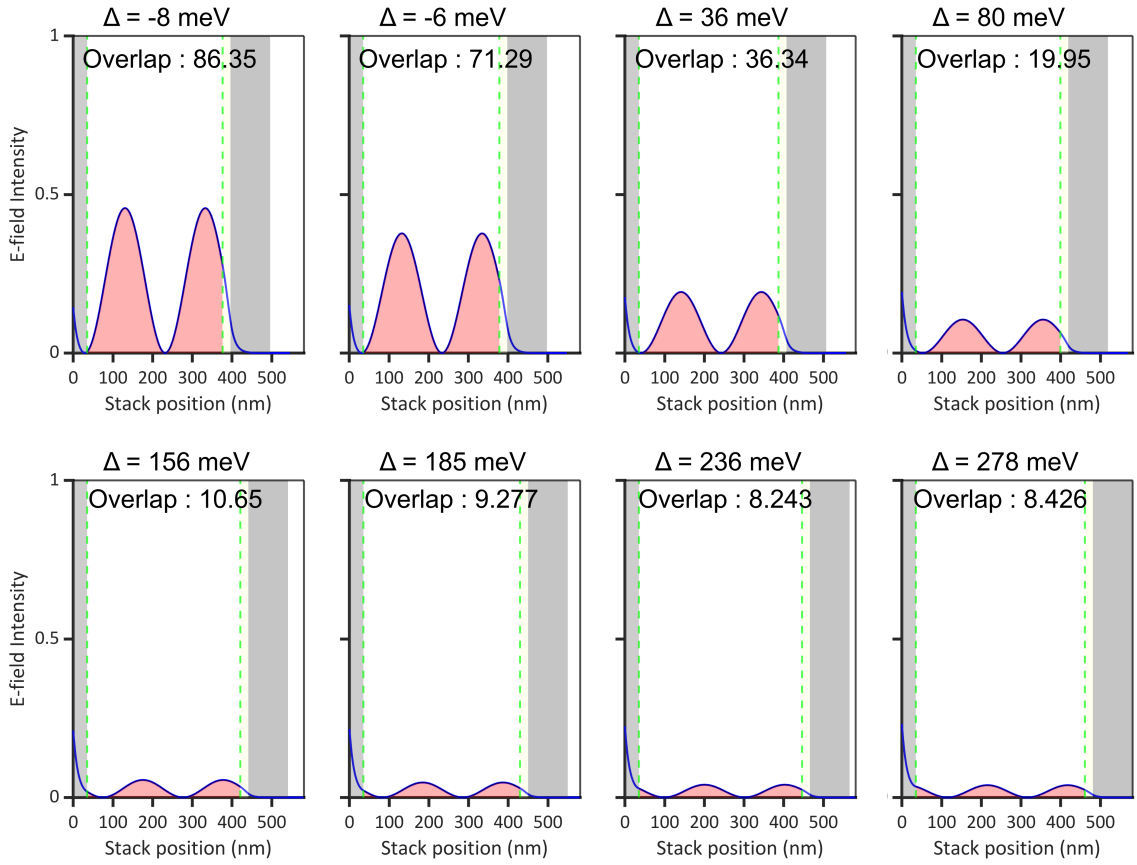

Figure 5.10. Simulated electric field intensity profiles at the excitation energy (E_{pump} = 1.94eV) and $k_{||}$ = 0 for 8 representative detunings ranging from –8 meV to 278 meV. The blue line shows the electric field intensity across the cavity stack, and the red shaded area indicates the integrated field overlap within the TAC trimer layer, bounded by green dashed lines. The overlap values are shown in each panel. The grey shaded regions mark the position of the silver mirror.

excitation energy of 1.94 eV (640 nm) was integrated over the TAC trimer layer for each cavity structure. This overlap quantifies how much of the incident excitation field interacts with the active layer, providing a relative measure of excitation efficiency across samples with different detunings, while accounting for intensity loss at the top mirror of each structure. Figure 5.10 shows the calculated electric field overlap for 8 representative detunings, with the different layers indicated by colored shading. The TAC layer thickness in each simulation was chosen to match the experimental reflectivity spectrum at the corresponding detuning. The correction factor was then determined by normalising each overlap value to the minimum observed in the series, allowing for consistent comparison of LP populations across detunings.

Figure 5.11 (a) shows the variation of Hopfield coefficients at $k_{||}$ = 0, extracted from the CHO fits to reflectivity data across the entire measured detuning range (–8 meV to 278

meV). The photon fraction (α^2, orange) and exciton fraction (blue) change with detuning. Since the measured LP PL intensity I_p originates from the radiative decay of the photon-like component, the true polariton population is proportional to I_p/α^2, where α^2 is the photon fraction of the LP state. [156] Figure 5.11 (b) presents the excitation efficiency correction factors discussed earlier, based on the overlap of the electric field intensity at the excitation energy with the TAC trimer layer (see Figure 5.10). Multiplying the population by this factor allows comparison across samples with different detunings under consistent excitation conditions.

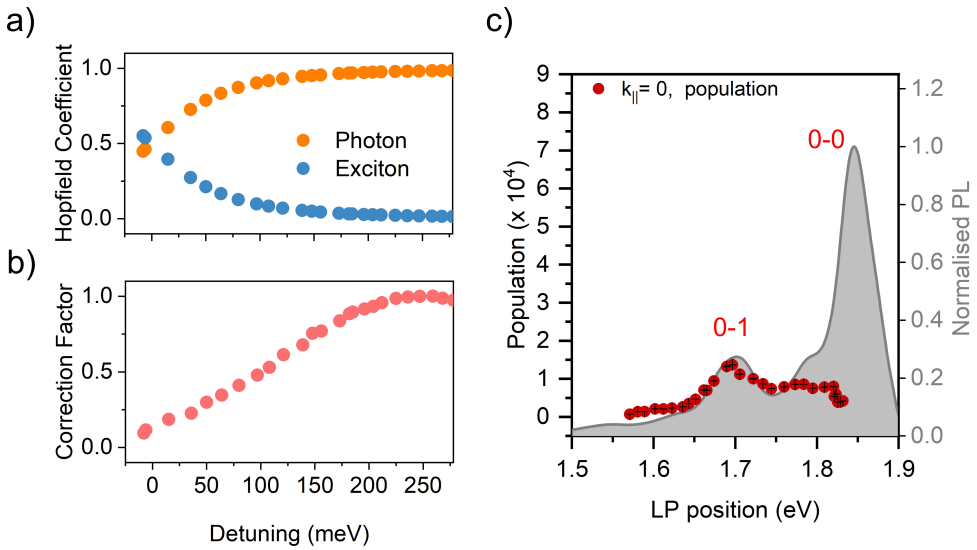

Figure 5.11. a) Hopfield coefficients at $k_{||} = 0$ ($\theta = 0°$) as a function of detuning. The orange dots represents the photon fraction, and the blue dots represents the exciton fraction b) xcitation efficiency correction factors calculated from electric field overlap at the pump energy (E_{pump} = 1.94eV) for each detuning. c) Calculated LP population at $k_{||} = 0$ as a function of LP energy (red circles), after applying photon fraction and excitation efficiency corrections. Error bars reflect averaging over ±1.5°. The normalised PL spectrum of the uncoupled TAC trimer film is overlaid in grey for comparison. The 0–0 and 0–1 vibronic emission features are indicated.

The corrected polariton population at $k_{||} = 0$ is shown in Figure 5.11 (c) as a function of LP energy, with error bars representing averaging over ±1.5° around normal incidence. The normalised PL spectrum of the uncoupled TAC trimer film is overlaid for comparison (grey shading). A clear dependence of the LP population on cavity detuning is revealed.

At higher detunings (> 50 meV) where the LP energy aligns with the Stokes-shifted 0–1 vibronic emission (≈1.708 eV) of the TAC trimer, the corrected LP population at $k_{||} = 0$ reaches a maximum. This is attributed to efficient RP, driven by strong spectral overlap between the LP band and the 0-1 emission peak of the uncoupled TAC trimer, in combination

with a favourable photonic Hopfield coefficient. In contrast, at lower detunings, the LP energy approaches the 0–0 emission peak (≈1.850 eV), where the uncoupled PL is strongest. However, the 0-0 transition state is energetically above the LP branch due to a small Stokes shift (3 meV). As a result, there is little to no overlap between the 0-0 transition of TAC trimer PL and the LP branch. This lack of overlap makes RP an inefficient decay pathway for polaritons formed at low detunings. This inefficiency is evident from the significantly reduced LP population at low detuning. This is consistent with the impact of Stokes shift of polariton relaxation reported by Hulkko et al. [203]

5.5 Vibrationally assisted scattering in TAC trimer

To examine the possibility of VAS as an alternative relaxation mechanism for populating LP states, the energy spacing between the LP and the ER is compared to the energies of molecular phonons of the TAC trimer. These phonon energies were identified using non-resonant Raman spectroscopy (excitation at 532 nm, 2.33 eV). As shown in Figure 5.12 (a), the Raman spectrum of the TAC trimer film displays multiple distinct Raman-active modes, with prominent peaks at 591 cm^{-1} (≈73 meV) and 1322 cm^{-1} (≈164 meV). These modes represent vibrations that may couple to the electronic transitions and thus could facilitate vibrationally assisted relaxation.

Figure 5.12 (b) plots the angle-integrated PL intensity from the LP states as a function of LP energy and cavity detuning. Where the emission is predominantly observed near the

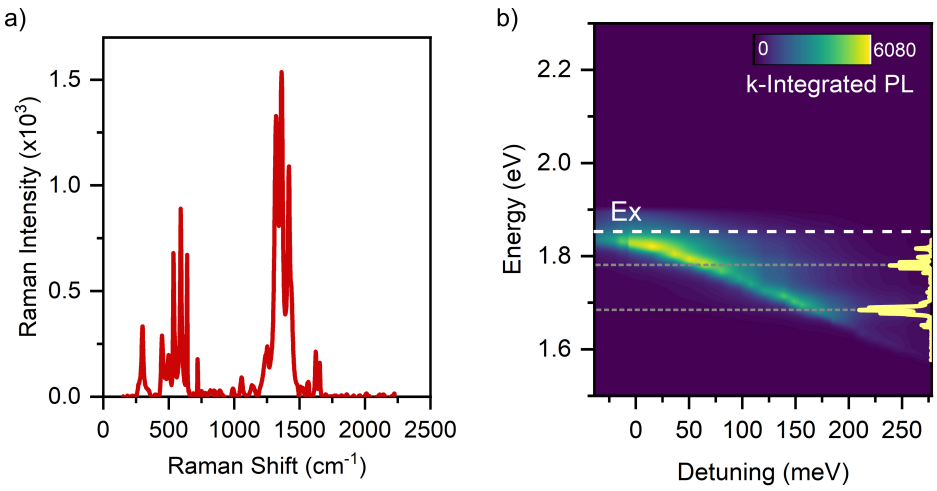

Figure 5.12. a) Raman spectrum of the TAC trimer film acquired under non-resonant excitation at 532 nm (2.33 eV), showing distinct Raman-active modes. b) Angle-integrated LP PL intensity plotted as a function of LP energy and detunings. The Raman spectrum of the drop-cast TAC trimer film (yellow line), the exciton energy (E_x) (white dashed line) and energy offsets of 73 meV and 164 meV (grey dashed line) below the exciton are indicated.

LP energy minimum. Grey dashed lines are included in Figure 5.12 (b) to indicate Raman-active vibrational modes at energy offsets of 73 meV and 164 meV below the exciton energy. While this figure does not provide conclusive evidence for resonant enhancement at specific phonon energies, the overall integrated PL profile may reflect the combined influence of multiple relaxation pathways. In particular, both RP and VAS could contribute to LP population under different detuning conditions. Although intrinsically weaker than RP, VAS can become significant when the LP energy aligns with strong Raman-active modes, especially in systems exhibiting strong vibronic coupling. [84]

A more detailed analysis of the detuning-dependent behavior of the LP PL is presented in Figure 5.13, which overlays the angle-integrated LP PL spectra (top panel) across all investigated detunings with the Raman spectrum and the photoluminescence of the uncoupled TAC trimer (bottom panel), plotted as a function of the energy separation $\Delta E = E_x - E_{LP}$. This representation provides a clearer view of how the LP PL modifies relative to both Raman active phonon modes and uncoupled molecular emission of the TAC trimer as the cavity detuning is varied.

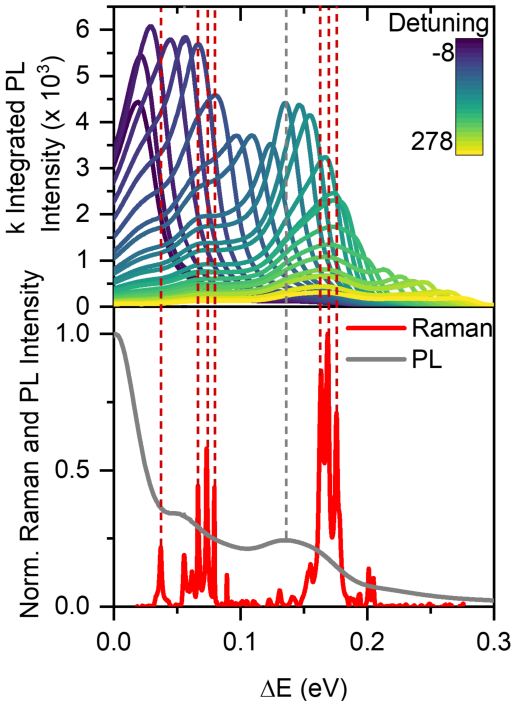

Figure 5.13. Comparison between the angle-integrated LP PL spectra across all detunings (top panel) and the Raman spectra and PL (grey curve) of the TAC trimer (red curve) (bottom panel), all plotted on a common energy axis, energy separation between the ER and the LP state ($\Delta E = E_x - E_{LP}$). The prominent Raman-active phonon modes (red dashed line) and the 0–1 vibronic emission peak (grey dashed lines) are indicated.

The angle-integrated LP PL intensity trend closely mirrors the behaviour observed in Figure 5.8 (b), with notable variations in LP PL intensity as the detuning is systematically increased. At a detuning of 139 meV, a pronounced PL peak emerges at an energy corresponding to the 0–1 vibronic emission of the uncoupled TAC trimer, suggesting that RP into the LP band occurs efficiently when the LP energy is resonant with this molecular transition. As the detuning is further increased to 173 meV, spectral broadening of the PL is observed, and the PL maximum shifts toward ΔE = 164 meV, a value that coincides with a prominent Raman-active vibrational mode. This spectral behaviour indicates a transition in the relaxation mechanism, wherein phonon-mediated processes begin to contribute more significantly to the population of LP states.

The broadening and shift of the PL peak at this detuning may be attributed to the onset of VAS, facilitated by energetic resonance between the LP states and Raman active phonon modes. At even larger detunings, particularly at 278 meV, the LP PL spectra exhibit marked enhancement in intensity at the 164 meV energy separation, further reinforcing the notion that phonon-mediated processes become increasingly efficient under higher detuning conditions.

To directly investigate the role of vibrationally assisted scattering, Figure 5.14 presents selected angle-integrated LP PL spectra at representative detunings (–8, 50, 139, and 278 meV), plotted as a function of energy separation ΔE and overlaid with the Raman spectrum. For small detunings (–8 and 50 meV; panels a and b), where the LP energy is not in resonance with any prominent Raman-active modes, the PL spectra remain relatively featureless, with no substantial enhancement observed. In contrast, at 139 meV detuning (panel c), the LP energy coincides with the 73 meV phonon mode, and a modest increase in PL intensity is detected, suggesting that phonon-mediated relaxation into the LP band is possible but not strongly favoured at this detuning.

The most compelling evidence for VAS arises at the 278 meV detuning (panel d), where the LP energy is simultaneously resonant with both the 73 meV and 164 meV Raman-active modes. In this regime, the PL spectrum displays two well-defined peaks that are spectrally aligned with the corresponding Raman active phonon modes. These peaks exhibit enhanced intensity and maintain consistent spectral positions across all the higher detunings (> 173 meV), providing strong evidence that VAS serves as an efficient population pathway at larger detunings when the LP states are energetically aligned with specific vibrational modes.

5.6 Discussion and conclusion

This study examined a strongly coupled microcavity system containing a TAC trimer, a molecule with well-defined vibronic structure. The TAC trimer was embedded in a polystyrene

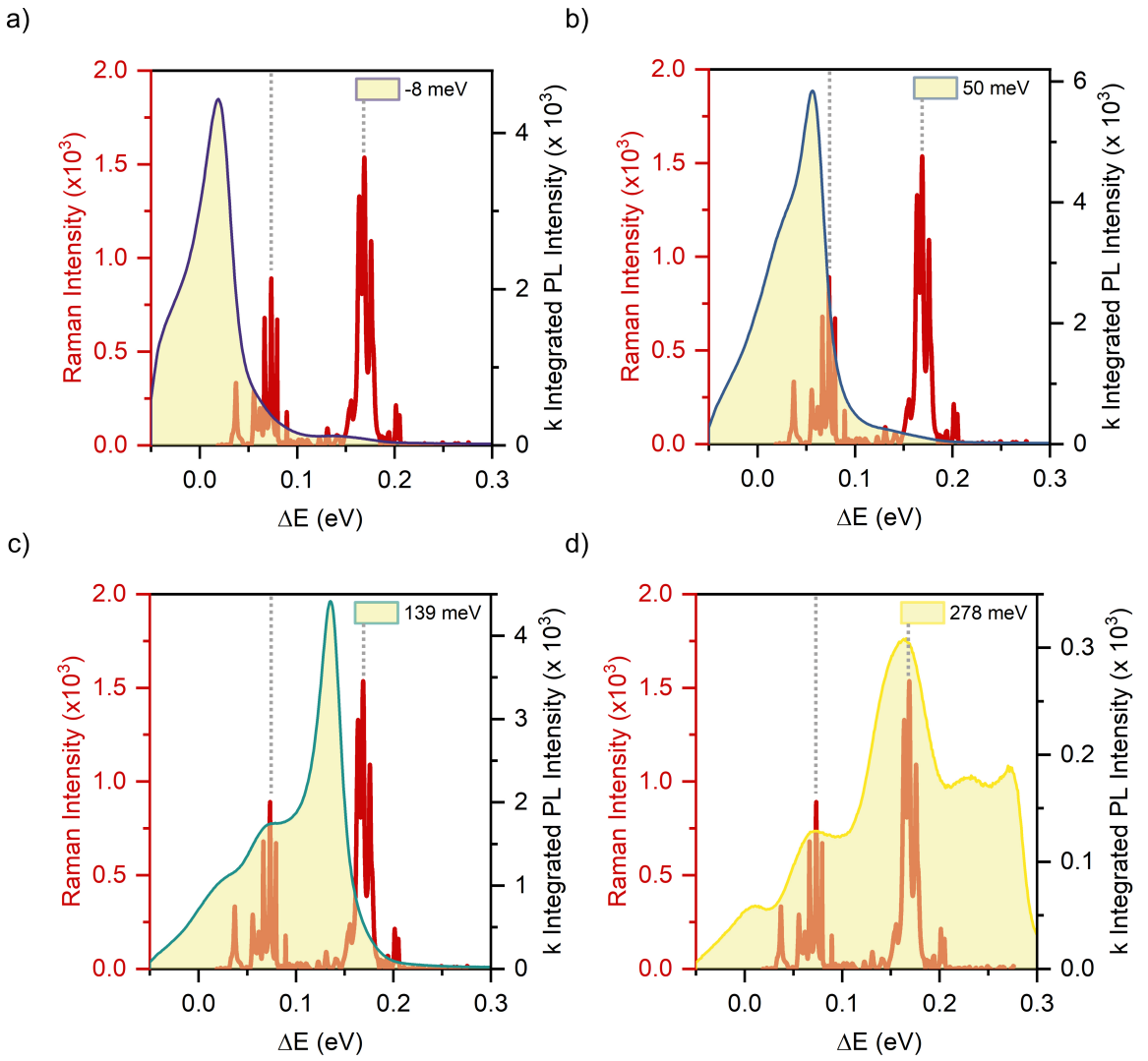

Figure 5.14. The shaded curve represents the angle-integrated photoluminescence (PL) emission intensity spectra measured at detuning levels of (a) -8 meV, (b) 50 meV, (c) 139 meV, and (d) 278 meV for the TAC trimer cavity. Small peaks, highlighted in all spectra, are presented as a function of the energy separation, ΔE, from the dark states at 1.835 eV. These peaks coincide precisely with the energy separations where the strongest vibrational energies of the TAC trimer match the dark states, as indicated by the Raman spectrum (red) of the TAC trimer.

matrix and placed between metal mirrors to form a cavity. The observed Rabi splitting of 36 meV confirms the system operates in the strong light–matter coupling regime, forming hybrid light–matter states.

Angle-resolved and angle-integrated photoluminescence spectra collected across a wide detuning range were analysed to reveal the influence of detuning on the relaxation pathways populating LP states. The detuning dependence of LP population mechanisms can be understood by considering three distinct detuning ranges: low, intermediate, and high detuning.

At low detuning (-8 to 50 meV), where the LP energy lies near the 0–0 emission peak of the uncoupled TAC trimer, the small Stokes shift (3 meV) results in poor spectral overlap between the LP modes and the 0–0 vibronic emission. As a result, RP is inefficient in this range, leading to a low LP population. Moreover, VAS does not contribute significantly in this regime, as the LP energy is not resonant with any Raman-active vibrational modes of the TAC trimer at low detuning. This is reflected in angle-integrated PL spectra at low detuning, where emission dominates at the minimum of the LP band and no additional spectral features are observed.

In the intermediate detuning range (64 to 156 meV), the LP energy becomes resonant with the 73 meV Raman active mode and 0–1 vibronic emission band (≈1.708 eV). The LP population reaches a clear maximum in this range when the LP states become resonant with 0-1 emission peak. This population maximum corresponds to the detuning range where RP is most effective. Notably, within this detuning region, the first signs of VAS also begin to emerge. Weak but reproducible spectral features appear in the angle-integrated PL at energy offsets of 73 meV below the exciton energy, coinciding with a prominent Raman-active phonon mode of the TAC trimer. At a detuning of approximately 97 meV, the LP energy becomes resonant with this vibrational mode, supporting the onset of VAS as a secondary relaxation pathway. However, as the detuning increases further to 156 meV, spectral overlap between the LP and the 0–1 vibronic emission improves, enhancing the efficiency of RP. Nonetheless, the persistence of sharp spectral features at fixed energy offsets at 73 meV below the exciton energy, in the angle-integrated PL spectra indicates that VAS remains active. These features, which do not vary with detuning and coincide with known Raman-active modes, provide clear spectroscopic signatures of phonon-mediated scattering into LP states, demonstrating that VAS continues to contribute alongside RP to populate LP.

At high detuning ($\Delta \geq 173$ meV), the energy minimum of the LP band at $k_{||} = 0$ becomes increasingly red-shifted relative to the 0–1 vibronic emission of the uncoupled TAC trimer. The overlap between the 0–1 emission and the high-angle LP states still persists. This gives rise to a continued, but diminished, RP contribution, which manifests in the angle-integrated PL as a broad emission feature centred near 164 meV below the exciton energy. This broadening reflects the population of higher-angle LP states through RP, but the efficiency of this process is suppressed due to the decreasing photonic character of LP states at larger angles, which reduces their emission efficiency. [14] Superimposed on this broad RP-related background, distinct narrow features emerge at fixed energy separations of approximately 73 meV and 164 meV below the exciton, consistent with known Raman-active vibrational modes of the TAC trimer.

The simultaneous presence of both broad RP features and sharp vibrational sidebands at high detuning suggests that both mechanisms contribute to LP population in this range,

the efficiency of RP decreases, particularly for high-angle LP states, due to their reduced photonic content. Taken together, these findings demonstrate that the relative efficiency of each pathway is thus determined by the detuning-dependent interplay between spectral overlap between LP states and the TAC trimer PL (0-1 emission), the angular distribution of LP photonic content, and the resonance conditions with specific molecular vibrational modes. This underscores the importance of detuning as a control parameter for selectively activating distinct relaxation channels in strongly coupled organic microcavities.

6. Towards Tuning Energy Transfer in Strongly coupled organic multilayer cavities

This chapter investigates the influence of donor-acceptor exciton energy offset on long-range energy-transfer efficiency in optical microcavities. The investigation utilises spectroscopic analysis to examine uncoupled systems and coupled systems within organic multilayer cavities. The research explores the formation of the polariton bands, the coupling strengths, and the Hopfield coefficients of two distinct donor-acceptor systems with varying energy offset is explored. Through a comparative analysis of cavity and non-cavity systems, the energy offset between donor and acceptor excitons as a tunable parameter for optimising energy transfer processes is investigated to improve polariton-mediated energy transfer in optoelectronic devices.

6.1 Introduction

Polaritons enable long-range energy transfer by combining light and matter properties, allowing energy to travel efficiently across large distances in materials. Long-range polariton-mediated energy transfer in multilayer microcavity systems has been a subject of extensive research, utilising both organic and inorganic materials. [17, 36, 182, 205–207] These systems typically consist of donor and acceptor layers separated by a spacer, all enclosed within an optical microcavity. Organic molecules, particularly J-aggregated cyanine dyes, have demonstrated ultralong-range energy transfer over distances up to 2 µm. [17] Inorganic materials, such as lead halide perovskite nanocrystals and transition metal dichalcogenides, have also shown promising results in polariton-assisted energy transfer. [208, 209] Various spacer materials, including polymeric layers, inorganic dielectrics, and transparent organic layers, have been employed to fine-tune cavity properties and transfer efficiency.

To date, the majority of polariton-mediated energy transfer studies have focused on systems where both donor and acceptor molecules emit within the visible spectrum. However,

the exploration of energy transfer to NIR emitting species remains limited, despite its significant potential in advanced photonic and optoelectronic applications. NIR emission offers several advantages, including reduced scattering and reabsorption losses, making it particularly suitable for biomedical imaging, night vision technologies, and solar energy harvesting. [210–214] Efficient long-range energy transfer to NIR emitters could therefore open new pathways for the development of high-performance polaritonic devices. Early demonstrations of strong coupling with NIR-active materials, such as single-walled carbon nanotubes (SWCNT) and narrow bandgap conjugated polymers, highlight the feasibility and promise of this approach. [34, 163, 215]

Recent work by Mischok et al. demonstrated that multilayer polaritonic structures can precisely control light emission, as shown by their high-efficiency, narrowband polariton OLEDs, exemplifying the potential of such systems in next-generation optoelectronic devices. [216] Central to the efficiency of these devices is the formation of polariton states and the associated relaxation pathway through which energy redistribution occurs. In strongly coupled systems where donor and acceptor species share a common optical mode, energy transfer can be facilitated by the formation of mixed polariton states, particularly the MP—which enables coherent energy oscillation between spatially separated molecules over micrometre scale distances.

A critical factor influencing the efficiency of polariton-mediated energy transfer is cavity detuning, defined as the energy difference between the uncoupled cavity mode and the excitonic resonance. When the cavity is resonant or red-detuned (i.e., at or below the exciton energy), polariton states exhibit increased mixing of donor and acceptor excitonic character, which enhances energy exchange. For instance, in MoS_2/WS_2 heterostructures, red-detuned cavities have demonstrated a 440-fold improvement in energy transfer efficiency compared to FRET. [217] Conversely, under blue-detuned conditions, polariton states tend to adopt predominantly acceptor-like character, leading to reduced overlap with donor states and diminished energy transfer.

The excitonic composition of polariton states, quantified by Hopfield coefficients, can be modulated independently via the tuning of cavity-donor and cavity-acceptor coupling strengths. This provides a powerful means to manipulate the energy transfer pathway within the system. [195, 218] Additionally, theoretical studies have proposed supplementary transfer pathways in strongly coupled systems, such as those mediated by vibrational relaxation mechanisms, which may play a key role in complex molecular environments. [219]

Despite these advancements, a systematic investigation into how donor-acceptor exciton energy offsets influence energy transfer efficiency, particularly in systems involving NIR acceptors, remains lacking. The aim of this chapter is to investigate the influence of donor-acceptor exciton energy offset on polariton-mediated long-range energy transfer efficiency.

The study utilises commercially available organic fluorescent dyes in two donor-acceptor configurations with different excitonic separations. In both systems, the donor emits in the visible region while the acceptor emits in the NIR, and both species are strongly coupled to the λ-mode of a planar microcavity. Angle-resolved reflectivity and PL spectroscopy are employed to confirm the formation of three polariton branches. Non-resonant excitation PL characterisation demonstrates that the energy offset affects the population of the LP states. Integrated PL measurements are used to quantify energy transfer efficiency.

6.2 Spectroscopic characterisation of donors and acceptor organic dyes

6.2.1 Isolated dye properties in solution and PVA matrix

This study used two different donor molecules: ATTO 680 carboxylate (ATTO 680, D1) and ATTO 655 carboxylate (ATTO 655, D2), and one acceptor molecule, IRDye CW800 carboxylate (IRDye, A_{nir}). The chemical structures of these compounds are illustrated in Figure 6.3 (a–c), respectively. Both ATTO dyes are widely used in super-resolution microscopy techniques such as STORM and STED, owing to their high photostability, narrow emission bandwidths, and excellent compatibility with aqueous environments. [147–149] In this study, these dyes were selected not only for their stable and well-characterised photophysical behaviour, but also for their different absorption and emission energies (or wavelength). Although they share similar chemical structures, fluorescence lifetimes, and quantum yields (see table 6.1), ATTO 680 exhibits a red-shifted absorption and emission spectrum compared to ATTO 655. This controlled variation in donor emission energy introduces a tunable energy offset relative to the acceptor molecule (IRDye), allowing systematic investigation into how donor-acceptor spectral alignment influences the efficiency of polariton-mediated long-range energy transfer. By employing two donors with well-defined but distinct optical properties, the study isolates the role of donor exciton energy in governing polariton population and energy transfer efficiency within the strongly coupled microcavity system.

The acceptor molecule, IRDye, exhibits optical transitions in the NIR region, with an absorption maximum at 1.602 eV (774 nm) and emission maximum at 1.572 eV (789 nm). It has a high molar extinction coefficient of 2.4 x 10^5 $M^{-1}cm^{-1}$, indicating strong light absorption capabilities, required for strong coupling. The molecule has a fluorescence lifetime of 0.64 ns and a relatively smaller Stokes shift of 30 meV compared to the donor molecules.

To assess the effect of the solid-state environment on dye behaviour, the optical properties of the donor and acceptor molecules were further examined in thin films. These films were fabricated by spin-coating aqueous solutions of the dye and PVA onto an optically clean glass

Table 6.1. Photophysical properties of donor and acceptor molecules in solution.

Donors	Ex [eV] (λ[nm])	Ex_{em} [eV] (λ_{em}[nm])	ϵ[$M^{-1}cm^{-1}$] *	PLQY[%] *	τ[ns]	Stokes Shift [meV]
ATTO655-carboxy	1.870 (663)	1.824 (680)	1.25 x 10^5	30	1.6	46
ATTO680-carboxy	1.821 (681)	1.776 (698)	1.25 x 10^5	30	1.7	45
Acceptor						
IRDye 800CW	1.602 (774)	1.572 (789)	2.4 x 10^5	-	0.42	30

Ex = *Absorption maximum;* Ex_{em} = *Emission maximum;* ϵ = *Molar extinction coefficient; PLQY = Photoluminescence quantum yield;* τ = *Fluorescence lifetime measured at the emission maximum. Absorption and emission spectra were recorded using UV–Vis absorption and steady-state photoluminescence spectroscopy in aqueous solution. Fluorescence lifetimes were determined using TCSPC. The Stokes shift was calculated as the energy difference between the absorption and emission maxima.*

* *Values marked with an asterisk were obtained from manufacturer datasheets (ATTO-TEC GmbH or LI-COR Biosciences) and were not independently measured in this study.*

substrate. PVA served as the host matrix, promoting uniform molecular dispersion and film stability. Solvent selection was based on a comparative study of dye solubility and stability in water, dimethylformamide (DMF), dimethyl sulfoxide (DMSO), tetrahydrofuran (THF), and acetonitrile. Water was ultimately chosen due to its compatibility with both the PVA matrix and the dye molecules, and for maintaining dye stability throughout film preparation.

Dye degradation in water was observed after 24 hours, prompting the use of freshly prepared dye-PVA solution for each deposition. Incorporation into the PVA matrix significantly improved dye stability relative to solution phase, as confirmed by long-term monitoring of absorption and PL spectra. The absorption and PL spectra of the dyes in both aqueous solution and PVA matrix are presented in Figure 6.1, which illustrates the effect of the solid-state environment on optical behaviour.

Figure 6.1 (d–f) reveals that both ATTO dyes display a prominent S_{01} 0–0 transition, and a 0–1 vibronic shoulder in both absorption and PL spectra, consistent across solution and PVA matrix. In contrast, IRDye CW800 displays both 0–0 and 0–1 features in its absorption spectrum in both media. In the PL spectra, the 0–1 transition is less distinct, particularly in solution, but becomes more noticeable in the solid-state PVA matrix. This partial resolution of the vibronic structure suggests that IRDye CW800 exhibits weaker vibrational coupling in the excited state compared to the ATTO dyes.

All three dyes exhibit slight red-shifts in their absorption and PL maxima upon incorporation into the PVA matrix compared to their aqueous spectra. These spectral shifts are attributed to matrix–dye interactions that perturb the local dielectric environment, thereby

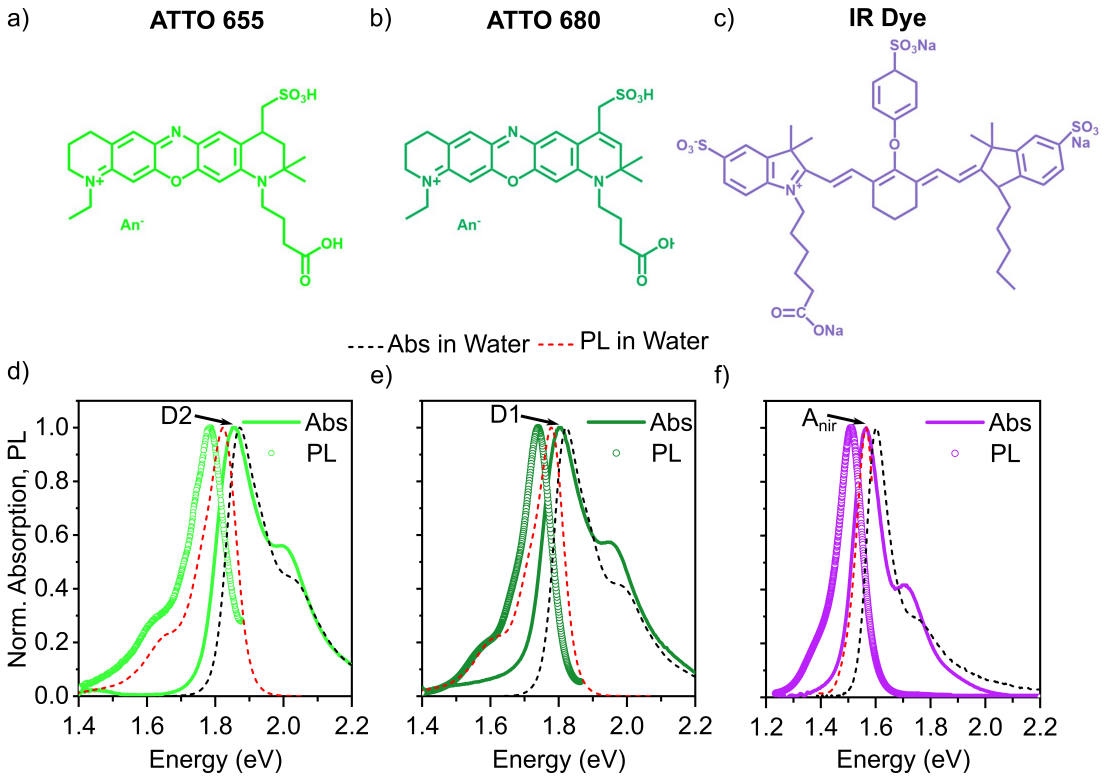

Figure 6.1. Molecular structures of (a) ATTO 655 (D2), (b) ATTO 680 (D1), and (c) IRDye CW800 (A_{nir}). Panels (d–f) show absorption (solid lines) and PL (scatter points) spectra of D2, D1, and A_{nir} in the PVA matrix. Dashed black and red lines represent the absorption and PL spectra in water, respectively. Excitonic 0–0 transition peaks are marked for each species.

modulating the energy levels of the electronic transitions. Despite the shifts, key spectral features are retained in the PVA matrix, suggesting minimal perturbation of their electronic structure upon transition from solution to the solid-state environment.

The corresponding photophysical parameters for the dyes in the PVA matrix are summarised in Table 6.2. Both ATTO 655 and ATTO 680 display absorption maxima at 1.856 eV (668 nm) and 1.805 eV (687 nm), respectively, and emission maxima at 1.784 eV (695 nm) and 1.740 eV (713 nm), with Stokes shifts of 72 meV and 65 meV. IRDye CW800 shows further red-shifted transitions with an absorption maximum at 1.566 eV (792 nm) and emission maximum at 1.511 eV (821 nm), yielding a Stokes shift of 55 meV.

In the PVA matrix, all dyes exhibit shorter fluorescence lifetimes and larger Stokes shifts compared to their behaviour in solution—observations that are typical for organic fluorophores embedded in solid-state environments. These changes are commonly attributed to increased non-radiative decay pathways, matrix-induced quenching, and restricted molecular motion. The data presented here establish that, despite these environmental changes, the dyes retain sufficiently sharp and structured optical transitions for strong coupling to

occur. Thus, this characterisation validates the use of PVA as a host matrix and provides a necessary foundation for interpreting the subsequent polaritonic behaviour in the multilayer microcavity systems.

Table 6.2. Photophysical properties of donor and acceptor molecules embedded in PVA matrix.

Donors	Ex [eV] ($\lambda[nm]$)	FWHM (meV)	Ex_{em} [eV] ($\lambda_{em}[nm]$)	τ[ns]	Stokes Shift [meV]
ATTO655-carboxy	1.856 (668)	110	1.784 (695)	0.10	72
ATTO680-carboxy	1.805 (687)	100	1.740 (713)	0.16	65
Acceptor					
IRDye 800CW	1.566 (792)	107	1.511 (821)	0.059	55

Ex = *Absorption maximum; FWHM = Full Width at Half Maximum of the absorption peak;* Ex_{em} = *Emission maximum;* τ = *Fluorescence lifetime measured at the emission maximum. Absorption and emission spectra were recorded using UV–Vis absorption and steady-state photoluminescence spectroscopy. Fluorescence lifetimes were measured using TCSPC. All measurements were conducted on thin films of the dye embedded in a PVA matrix deposited on glass substrates. The Stokes shift was calculated as the energy difference between the absorption and emission maxima.*

6.2.2 Reference microcavities: donor-based and acceptor-based systems

To evaluate the individual coupling characteristics of the donor and acceptor molecules, reference metal-clad microcavities were fabricated in which only one active dye species—either donor or acceptor—was embedded within a PVA matrix. The structure of the metal-clad multilayer microcavities used in this study is illustrated in Figures 6.2 (a-c). Figure 6.2 (a) illustrates the donor-based microcavity configuration with ATTO 655 (D2), Figure 6.2 (a) shows the cavity containing ATTO 655 (D2), Figure 6.2 (b) corresponds to the cavity with ATTO 680 (D1), and Figure 6.2 (c) depicts the acceptor-based cavity with IRDye CW800 (A_{nir}). In each case, the complementary layer in the multilayer microcavities is replaced with pure PVA to isolate the optical response of the individual emitter.

The corresponding angle-resolved reflectivity and PL spectra are presented in Figures 6.2 (d–f), revealing the characteristic dispersions for the ATTO 655, ATTO 680, and IRDye CW800 microcavities, respectively. A CHO model was employed to describe the observed polaritonic features and to extract the relevant coupling parameters.

Both donor-based systems exhibit clear UP and LP branches in their dispersion spectra (Figures 6.2 (d, e)), indicative of the strong coupling regime. The extracted coupling

strengths are 64 meV for ATTO 655 and 45 meV for ATTO 680. In both cases, the cavities operate under negative detuning conditions, with detuning values of 221 meV and 230 meV, respectively. Emission in both systems is predominantly localised on the LP branch.

The dispersion of the acceptor-based cavity, shown in Figure 6.2 (f), similarly reveals polaritonic splitting with a coupling strength of 42 meV and a detuning close to zero. As with the donor systems, PL primarily originates from the LP branch.

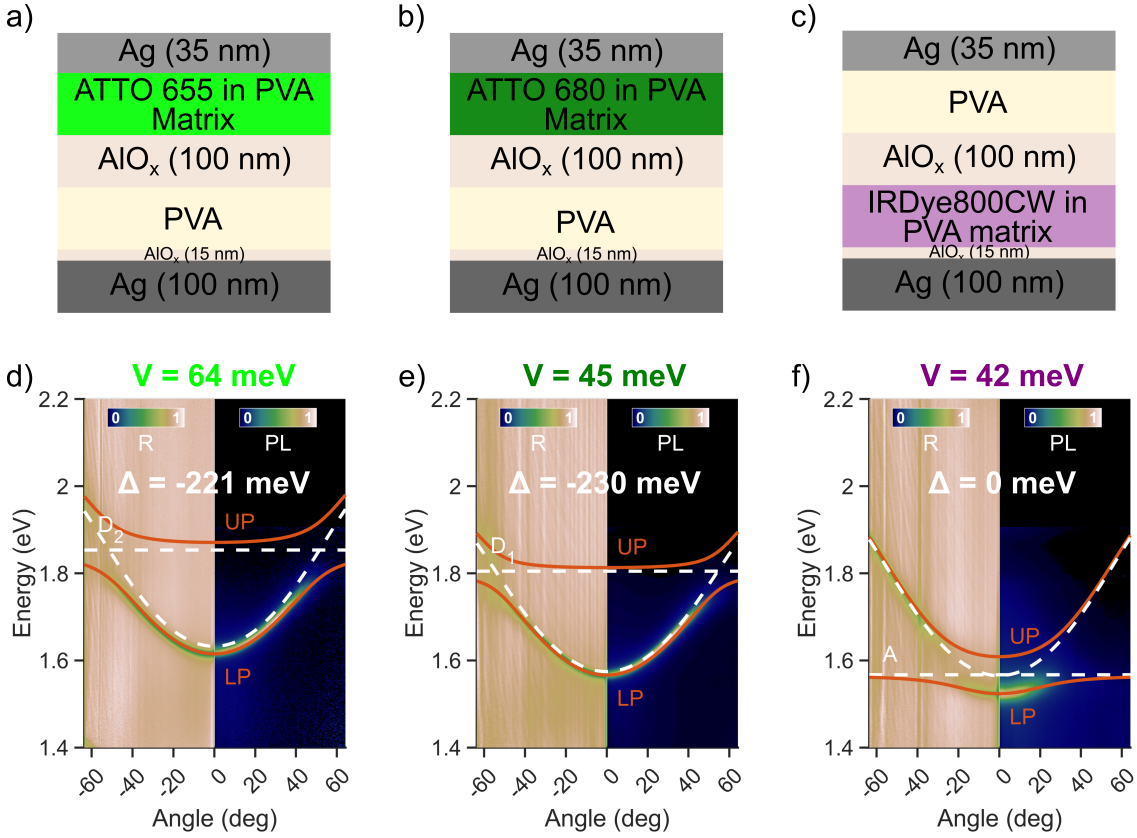

Figure 6.2. (a-c) Schematic of (a) D2- based multilayer microcavity containing ATTO 655 (b) D1- based multilayer microcavity containing ATTO 680. (c) A_{nir}- based multilayer microcavity containing IRDye. (d–f) Angle-resolved reflectivity and PL spectra of the D2-based, D1-based and A_{nir}-based microcavities, respectively, in a PVA matrix. The UP and LP modes (red lines), cavity dispersions (white dashed lines), and excitonic energies (D2 in (d), D1 in (e), and A_{nir}in (f)(white dashed lines)) are shown. Detuning (Δ) and coupling strength (V) are indicated.

Quality factors (Q) for the cavities were estimated, yielding values of approximately 73 for ATTO 655, 87 for ATTO 680, and 64 for IRDye CW800. These moderate Q-factors are typical for strongly coupled metal-clad microcavities. The criterion for strong coupling, given by $\frac{1}{4}(\mathrm{FWHM_{ex}} + \mathrm{FWHM_{cav}})$ was applied to verify the coupling regime. Using estimated linewidths of $\mathrm{FWHM_{ex}} \approx 110$ meV and $\mathrm{FWHM_{cav}} \approx 30$ meV, the threshold for strong coupling is approximately 35meV. As all three systems exceed this value, it is confirmed that

each dye species individually reaches the strong coupling regime when incorporated into a microcavity.

The optical properties extracted from the reference donor- and acceptor-based microcavities, such as coupling strengths and cavity layer thicknesses, serve as critical input parameters for subsequent modelling of more complex hybrid microcavities using TMM.

6.3 Modelling of donor-acceptor multilayer system using TMM

Modelling the optical response of donor-acceptor multilayer cavity systems incorporating spatially separated donor–acceptor ($D–A_{nir}$) pairs, as illustrated in Figure 6.3 (a), is a critical step in the design and interpretation of polariton-mediated long-range energy transfer. The TMM provides the computational framework for simulating the propagation of light through stratified media, accounting for interference effects, absorption, and internal field distributions. By tailoring the optical field profile, it is possible to optimise the spatial positioning of donor and acceptor layers within the cavity such that they coincide with the antinodes of the optical mode—regions of maximum electromagnetic field intensity. This spatial over-

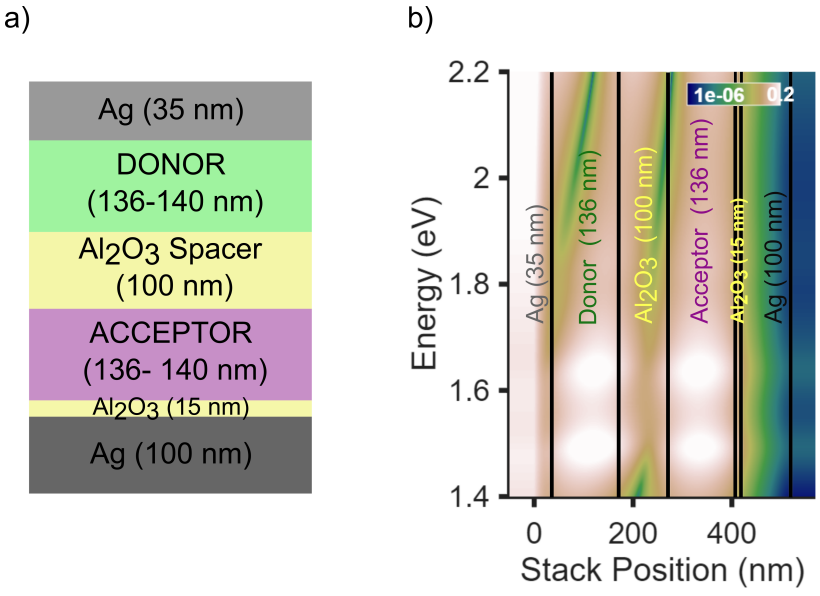

Figure 6.3. (a) Schematic of the multilayer cavity structure used for TMM simulations. The stack consists of Ag (35 nm)/Donor (136-140 nm)/Al_2O_3 (100 nm)/Acceptor (136-140 nm)/Al_2O_3 (15 nm)/Ag (100 nm). (b) Simulated electric field intensity profile across the structure at the cavity resonance. The donor and acceptor layers are located at or near the antinodes of the cavity mode, optimising light–matter interaction and enabling strong coupling.

lap enhances the exciton–photon coupling strength and thereby facilitates the formation of hybrid polariton states capable of mediating energy transfer over extended distances.

In this study, the thicknesses of the constituent layers were systematically tuned to fulfil two primary design criteria: (i) spectral resonance between the cavity mode and the excitonic transitions of both the donor and acceptor dyes, and (ii) separation between the donor and acceptor layers to allow the study of long-range energy transfer, while still maintaining strong coupling with the cavity mode. TMM simulations incorporated the wavelength-dependent complex refractive indices of all materials in the cavity stack. The resulting electric field intensity profiles confirmed that both the donor and acceptor layers were positioned near the antinodal planes of the λ-mode cavity field (Figure 6.3 (b)). The field distribution revealed the presence of two spatially distinct optical modes, indicative of strong light–matter coupling within the multilayer system. These results demonstrate that the spatial arrangement of the layers fulfils the necessary conditions for effective exciton–photon interaction and supports the formation of hybrid polariton states essential for long-range energy transfer.

To validate the simulated structure, angle-resolved reflectivity spectra were calculated and compared with experimental measurements obtained from angle-resolved spectroscopy. As shown in Figures 6.4 (a) and 6.4 (b), there is excellent agreement between the simulated and experimental data for both D2–A_{nir} and D1–A_{nir} cavity systems. The polariton dispersion, characterised by the formation of three hybrid light–matter branches—the UP, MP and LP—is well reproduced in the simulations.

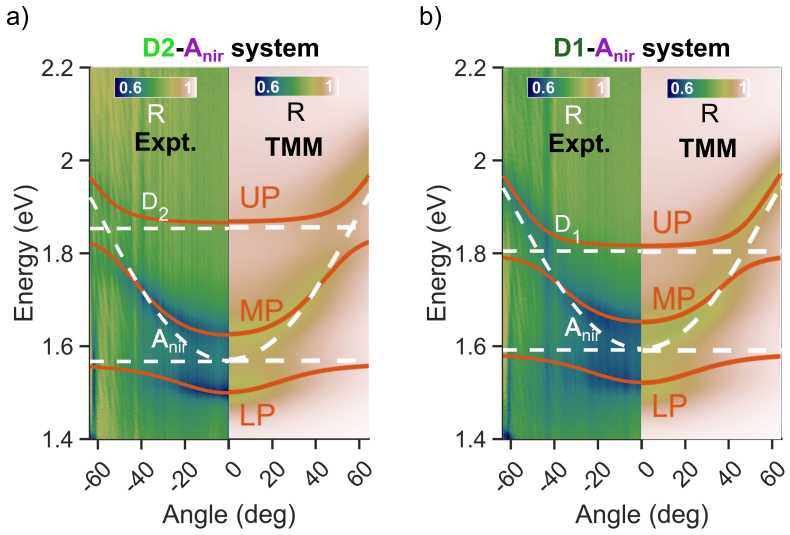

Figure 6.4. Comparison of experimental and simulated angle-resolved reflectivity spectra for the (b) D2–A_{nir} and (c) D1–A_{nir} cavity systems. The left halves show experimental spectra; the right halves show TMM simulations. Red curves represent the fitted polariton branches—UP, MP and LP—and white dashed lines mark the exciton energies of the donor (D_1, D_2) and acceptor (A_{nir}).

In the experimental spectra, the MP and LP branches exhibited well-defined spectral features and aligned closely with the predicted dispersion curves, confirming strong coupling of both donor and acceptor excitons to the cavity mode. The UP branch showed reduced visibility in the experimental data, although well defined in the TMM simulated dispersion and predicted by the CHO model. This limited visibility in the experimental angle-resolved reflection spectra can be attributed to decreased spectral signal-to-noise ratio in that region. Despite its weak visibility, the presence of the UP mode in the simulated spectra and its influence on the overall dispersion strongly support the interpretation that the system remains in the strong coupling regime.

Together, these results demonstrate the utility of TMM as a predictive tool for the design of multilayer microcavities supporting strong light–matter coupling. The TMM modelling provides essential insight into the spatial and spectral characteristics of the cavity, informing both device fabrication and the interpretation of subsequent measurements.

6.4 Spectroscopic characterisation of donor-acceptor multilayer systems

6.4.1 Properties of donor-acceptor multilayer film systems

To investigate long-range energy transfer in the absence of optical confinement, multilayer reference films were fabricated with a donor–acceptor configuration separated by an optically inert Al_2O_3 spacer. The structure consisted of glass/Al_2O_3 (15 nm)/Acceptor/Al_2O_3 Spacer (100 nm)/Donor, as illustrated in Figure 6.5 (a,d). The fabrication procedure is detailed in Chapter 3. All optical measurements were conducted under excitation from the donor side to mimic energy transfer conditions relevant to cavity-coupled systems.

The inclusion of a 100 nm thick Al_2O_3 dielectric spacer serves to suppress Förster resonance energy transfer (FRET) between the donor and acceptor molecules by exceeding the typical FRET interaction range. This design strategy, which physically separates the emissive layers while maintaining optical transparency, has been demonstrated in previous studies as an effective means to isolate long-range energy transfer pathways such as those mediated by polaritons or radiative coupling mechanisms. [191]

Figures 6.5 (b) and (e) present the absorption and PL spectra of the donors (ATTO 655, D2 and ATTO 680, D1, respectively) and the acceptor (IRDye, A_{nir}), measured individually. The yellow shaded regions indicate the spectral overlap between donor emission and acceptor absorption, which is critical for efficient energy transfer. Figures 6.4 (c) and (f) show the absorption and PL spectra of the multilayer reference film systems containing D2+A_{nir} and D1+A_{nir}, respectively. These spectra exhibit a combination of the individual donor and

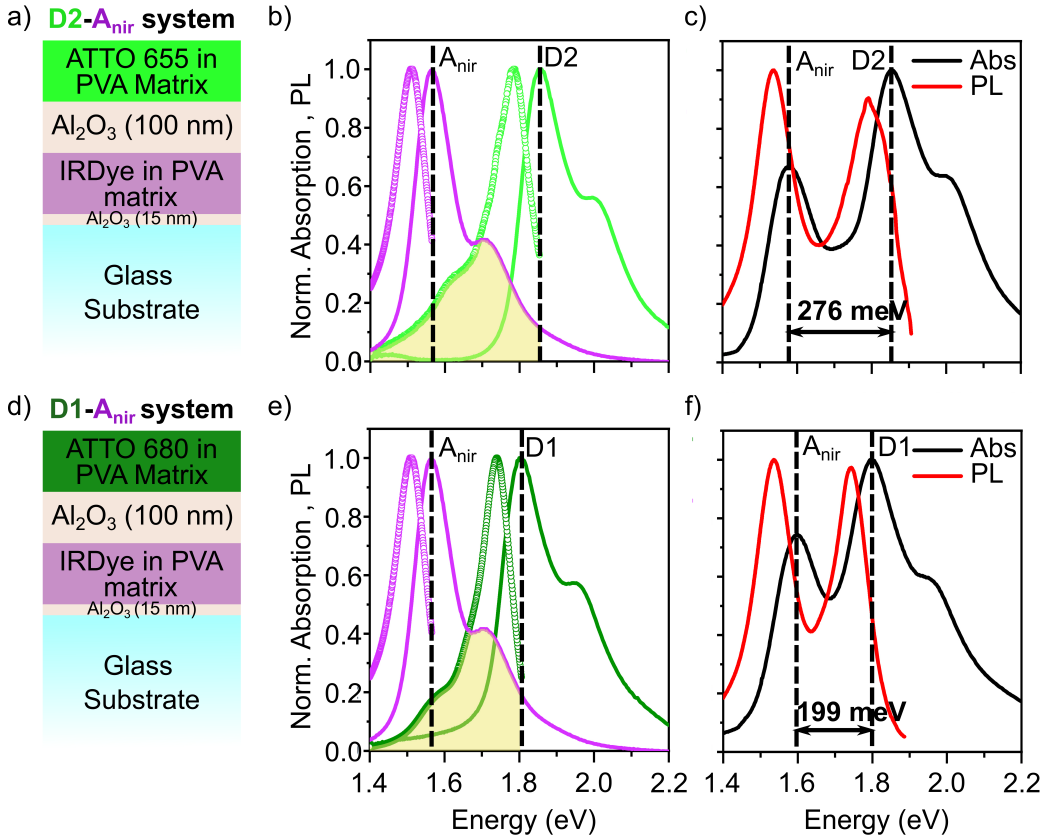

Figure 6.5. (a,d) Schematic representation of multilayer control film structures containing (a) ATTO 655 (D2) and IRDye (A_{nir}), and (d) ATTO 680 (D1) and IRDye (A_{nir}). The structure consists of glass/Al_2O_3(15 nm)/Acceptor/Al_2O_3 Spacer (100 nm)/Donor layers. (b,e) Absorption (solid lines) and PL (scatter points) spectra of individual D2 and A_{nir} (b), and D1 and A_{nir} (e). Spectral overlap regions are highlighted in yellow. (c,f) Absorption (black) and PL (red) spectra of D2–A_{nir} (c) and D1–A_{nir} (f) control films. Excitonic peak positions (E_{D1}, E_{D2}, and E_A) and donor–acceptor energy offsets are marked.

acceptor spectra, with both plots also highlighting the energy offset—the energy difference between the donor and acceptor excitons. Photoluminescence measurements of the D2–A_{nir} and D1–A_{nir} multilayer films revealed no quenching of donor emission and no enhancement of acceptor emission under donor excitation. This absence of donor–acceptor spectral cross-talk confirms that no significant energy transfer occurs across the 100 nm Al_2O_3 spacer. The result is consistent with the spatial separation exceeding the effective range of FRET, and establishes these multilayer configurations as appropriate reference systems for identifying long-range energy transfer under strong coupling conditions.

The optical characteristics of both donor–acceptor multilayer systems are summarised in Table 6.3. In the D2–A_{nir} system, ATTO 655 exhibits absorption and PL maxima at 1.854 eV (669 nm) and 1.791 eV (692 nm), respectively, whereas in the D1–A_{nir} system, ATTO 680 shows corresponding maxima at 1.797 eV (690 nm) and 1.744 eV (711 nm). Although the

acceptor molecule is identical in both systems, small variations are observed in its spectral features: in the D2-based film, IRDye absorbs at 1.578 eV and emits at 1.537 eV; in the D1-based film, absorption occurs at 1.598 eV and PL at 1.535 eV. These minor shifts may result from local variations in the dielectric environment or spectral superposition effects with the respective donor emission, which can influence the apparent peak positions.

Table 6.3. Optical properties of donor-acceptor reference films in a Al_2O_3 dielectric-separated multilayer structure

System	Ex_D [eV] ($\lambda[nm]$)	Ex_{Dem} [eV] ($\lambda[nm]$)	Ex_A [eV] ($\lambda[nm]$)	Ex_{Aem} [eV] ($\lambda[nm]$)	Spectral Overlap	Energy offset
D2-A_{nir}	1.854 (669)	1.791 (692)	1.578 (786)	1.537 (807)	0.098	276
D1-A_{nir}	1.797 (690)	1.744 (711)	1.598 (776)	1.535 (808)	0.085	199

D1 = ATTO680, D2 = ATTO655, A_{nir} *= IRDye. The multilayer structure consists of Glass /* Al_2O_3 *(15 nm) / Donor in PVA matrix /* Al_2O_3 *(100 nm) / Acceptor in PVA matrix (see Figure 6.4 (a, d).* Ex_D *= Absorption Maxima of the Donor,* Ex_Dem *= Emission Maxima of the Donor,*Ex_A *= Absorption Maxima of the Acceptor,* Ex_Aem *= Emission Maxima of the Acceptor. Spectral overlap refers to the degree of overlap between donor emission and acceptor absorption spectra. Energy offset is the difference between the donor emission maximum and the acceptor absorption maximum.*

The D2-A_{nir} system exhibits a higher spectral overlap (0.098) compared to D1-A_{nir} (0.085), suggesting potentially more efficient energy transfer. Additionally, the energy offset is larger for D2-A_{nir} (276 meV) than for D1-A_{nir} (199 meV). These optical characteristics establish the preconditions for energy transfer; however, the absence of experimental signatures of transfer confirms that these conditions alone are insufficient in the current geometry.

In summary, the optical characterisation of the dielectric-separated donor–acceptor multilayer films confirms that energy transfer does not occur in the absence of optical confinement. These reference structures therefore provide a critical control framework for assessing the role of strong light–matter coupling in enabling long-range energy transfer in subsequent cavity-integrated systems.

6.4.2 Strong coupling in the donor-acceptor multilayer Microcavities

The structural configurations of the donor-acceptor multilayer microcavities are shown in Figures 6.6 (a,c), which depict the D2-A_{nir} and D1-A_{nir} systems, respectively. The layer thicknesses were chosen based on TMM simulations to ensure that the donor and acceptor layers coincided with the cavity mode antinodes and that the spacer provided sufficient separation for long-range interaction studies. The corresponding angle-resolved reflectivity

and PL spectra are presented in Figures 6.6 (b,d), with the absorption and PL spectra of the reference (non-cavity) multilayer films included for reference.

To describe the light-matter interactions in these systems, a three-level CHO model was used. Diagonalisation of the Hamiltonian yields three polariton branches: UP, MP and LP. The MP is a mixed state containing contributions from both the donor and acceptor

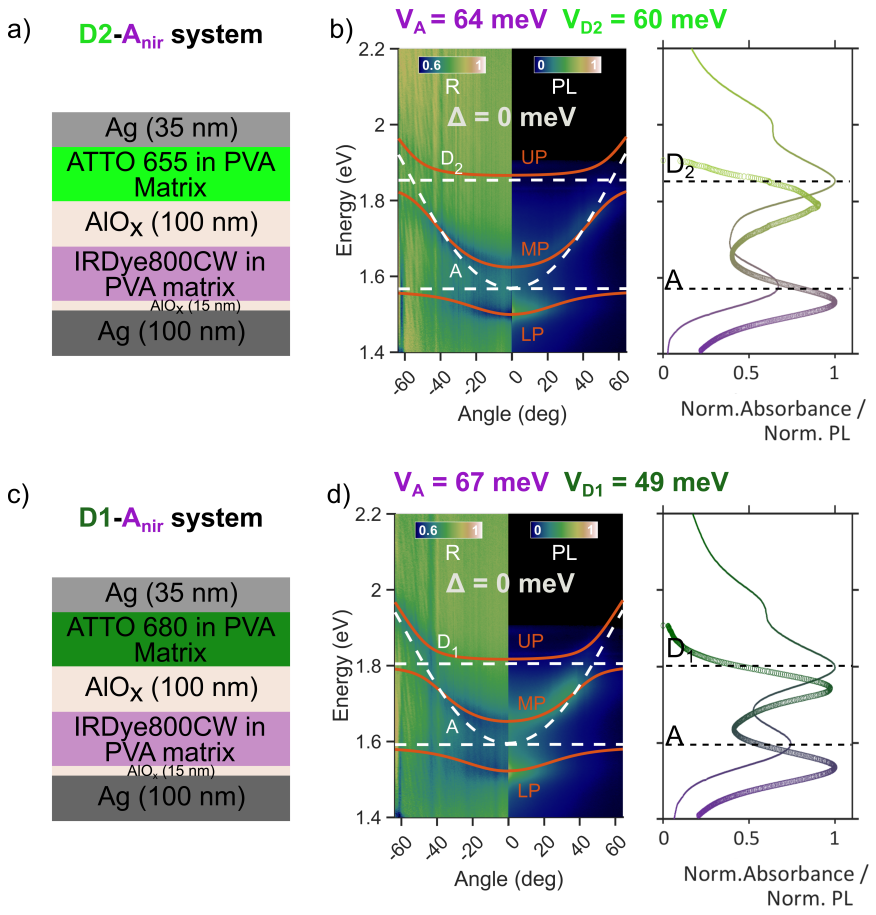

Figure 6.6. (a) schematic of a metal-clad multilayer microcavity containing ATTO 655 (donor 2, D2) and IRDye (acceptor, A_{nir}). (b) Angle-resolved reflection and PL spectra of the D2–A_{nir} multilayer microcavity; modes (red lines), cavity dispersions (white dashed lines), and excitonic energies (D2 and A_{nir}, white dashed lines) are shown. Detuning (Δ), coupling strengths (D2: V_{D2}, A_{nir}: V_A) are indicated. Right: absorption (line) and PL (scatter) spectra outside the microcavity, with excitonic energies (D2 and A_{nir}, black dashed lines) marked. (c) Schematic of a metal-clad multilayer microcavity with ATTO 680 (donor 1, D1) and IRDye (acceptor, A_{nir}). (d) Angle-resolved reflection and PL spectra of the D1–A_{nir} multilayer microcavity; modes (red lines), cavity dispersions (white dashed lines), and excitonic energies (D1 and A_{nir}, white dashed lines) are shown. Detuning (Δ), coupling strengths (D1: V_{D1}, A_{nir}: V_A) are indicated. Right: absorption (line) and PL (scatter) spectra outside the microcavity, with excitonic energies (D1 and A_{nir}, black dashed lines) marked.

excitons. The fitted dispersion curves align well with experimental observations, confirming the formation of hybrid polaritonic modes.

For the D2-A_{nir} cavity, the extracted coupling strengths are V_A = 64 meV and V_{D2} = 60 meV, while for the D1-A_{nir} system, the values are V_A = 67 meV and V_{D1} = 49 meV. Notably, in both systems, the acceptor shows a higher coupling strength despite the donor exhibiting stronger absorbance in the normalised absorption spectra. This is attributed to the inherently higher absorption coefficient of the IRDye acceptor. Both systems are tuned to zero detuning between the cavity mode and the acceptor exciton at normal incidence. PL emission arises predominantly from the MP and LP branches in both the systems.

While both microcavity systems are tuned to zero detuning and exhibit stronger coupling of the acceptor exciton, they differ in the choice of donor molecule, resulting in varying donor–acceptor energy offsets and donor coupling strengths. These variations lead to observable shifts in the polariton dispersion, particularly in the MP branch. As a result, they are expected to influence the distribution of excitonic character across the polariton branches. A more detailed analysis of the polariton composition will be presented in the following section.

6.5 Furhter discussion

To understand the role of donor-acceptor exciton energy offset on polariton composition and energy transfer, the donor–acceptor multilayer microcavity systems were modelled using a three-level CHO framework. The resulting eigenvectors yield Hopfield coefficients that quantify the exciton–photon fraction of each polariton branch. Figures 6.7 (a) and (c) illustrate the Hopfield coefficients for the LP, MP, and UP branches of the D2-A_{nir} and D1-A_{nir} multilayer microcavity systems, respectively. The photon fraction (α_γ) is shown in orange line, the donor fraction (α_{D2} or α_{D1}) by the green line, and the acceptor component (α_A) by the purple line. For both systems, which were tuned to zero detuning with respect to the acceptor exciton, the LP branch is predominantly composed of photon and acceptor fraction. At low angles, the LP has higher photonic content, while at higher angles, it becomes more excitonic, dominated by the acceptor. Conversely, the UP branch transitions from being more donor-like at low angles to increasingly photonic at higher angles.

The MP branch, a mixed state involving both excitons and the cavity photon, shows a notable dependence on the donor–acceptor energy offset. At the same cavity detuning, the D2–A_{nir} system, which features a larger energy offset (276 meV), exhibits reduced donor dominance and increased photonic content in the MP branch compared to the D1–A_{nir} system (offset of 199 meV), particularly at high angles. For example, at 0°, the MP in the D2–A_{nir} system consists of: 2.96% donor, 53.7% acceptor, 43.3% photon, while in the D1–A_{nir}

system it is: 4.5% donor, 52.2% acceptor, 43.3% photon. At 60°, the MP composition in D2–A_{nir} is: 69.8% donor, 1.9% acceptor, 28.9% photon, and in D1–A_{nir} it is: 88.9% donor, 1.15% acceptor, 9.9% photon. These results show that the MP in D1–A_{nir} becomes increasingly dominated by the donor exciton at high angles compaired to D2–A_{nir}. This reduced donor dominance in the D2-A_{nir} system could be correlated with the observed increase in acceptor-associated PL, suggesting that the MP composition, modulated by energy offset, affects energy transfer efficiency.

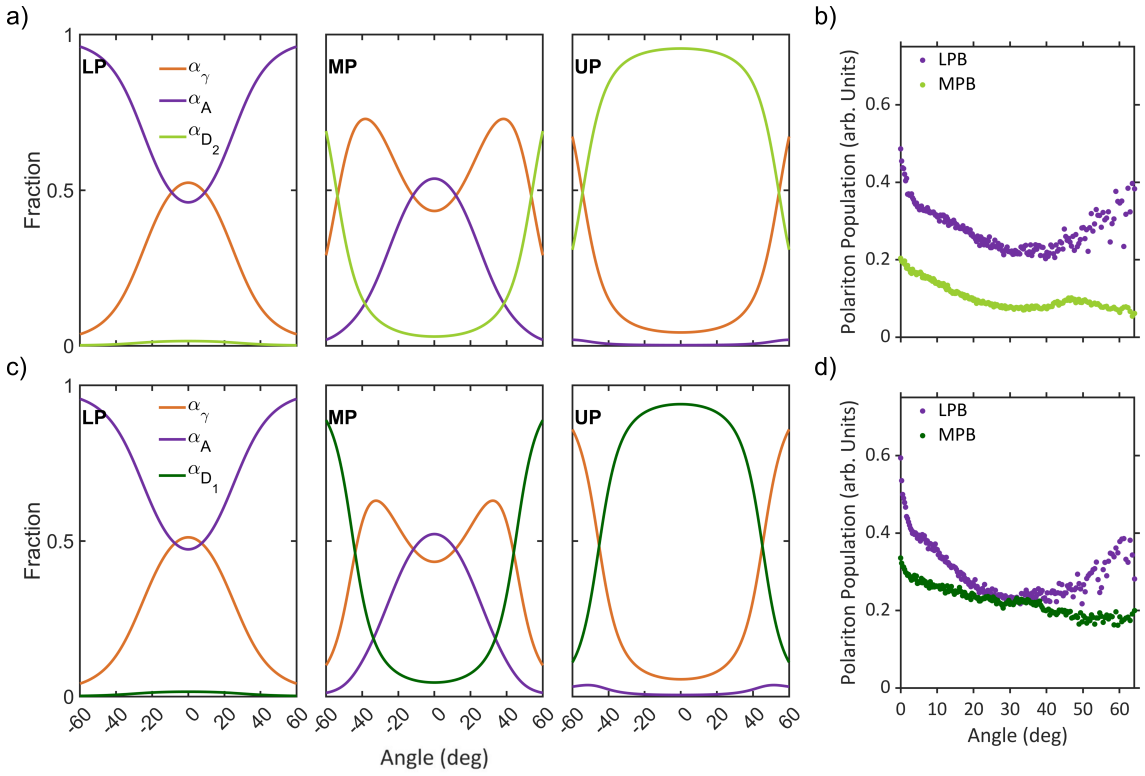

Figure 6.7. Hopfield coefficients and polariton populations in D2-A_{nir} and D1-A_{nir} multilayer microcavity systems. (a) Hopfield coefficients for the D2-A_{nir} system, showing the contributions of components to the polariton states. (b) Polariton populations of the LP and MP branches in the D2-A_{nir} system. (c) Hopfield coefficients for the D1-A_{nir} system, illustrating the mixing of excitons and photons in the polariton states. (d) Polariton populations of the LP andMP branches in the D1-A_{nir} system. All calculations were performed using a three-level coupled oscillator model for the multilayer cavity structure.

Figures 6.7 (b) and (d) show the angle-dependent relative polariton populations of the LP and MP branches in D2-A_{nir} and D1-A_{nir} microcavity systems, respectively. These were calculated by correcting the angle-resolved PL intensities for the photonic fraction at each angle. Briefly, the relative polariton population at an angle θ is calculated using the formula:

$$\text{Relative polariton population} = \frac{I(\theta)}{[\alpha_\gamma(\theta)]^2}$$

Where, I(θ) is the PL intensity at angle θ, $\alpha_\gamma(\theta)$ is the photon fraction at angle θ.

Emission is observed from both the LP and MP branches in the angle-resolved PL spectra for both D2–A_{nir} and D1–A_{nir} microcavities. From the relative polariton population plots, it is evident that the LP population increases as the polariton energy approaches the acceptor exciton energy at lower angles. This trend reflects the expected behaviour where polariton states close in energy to the exciton are more effectively populated via energy relaxation from the exciton reservoir. [36] A secondary rise in LP population beyond 30° in both systems is attributed to noise, as emission intensity is negligible in this region. In both systems, the LP population is consistently greater than that of the MP across all valid angles. This provides qualitative evidence for an efficient energy relaxation pathway that depopulates the MP and funnels excitations into the LP.

To further quantify overall energy transfer efficiency, angle-integrated PL spectra of the microcavities were compared to their respective uncoupled multilayer reference films. Figures 6.8 (a, c) show PL spectra of the D2–A_{nir} and D1–A_{nir} reference films, fitted using three Voigt profiles to extract the relative donor and acceptor contributions. The D2–A_{nir} film exhibited 51.3% donor and 48.7% acceptor PL contributions, while the D1–A_{nir} film showed equal contributions from both donor and acceptor. In contrast, the angle-integrated PL spectra of the strongly coupled microcavity systems, shown in Figures 6.8 (b) and 6.8 (d), show a clear increase in the proportion of acceptor-associated emission compared to the reference films. In the D2–A_{nir} cavity, the acceptor contribution increases from 48.7% to 55.7%, while in the D1–A_{nir} cavity, it increases from 50% to 51.8%. This redistribution is more pronounced in the D2–A_{nir} cavity with larger donor–acceptor energy offset.

The D2-A_{nir} system shows a shift towards higher acceptor-associated PL in the cavity system by 7% compared to the multilayer reference film PL, indicating enhanced energy transfer from donor to acceptor states within the strongly coupled cavity. In the D1-A_{nir} system, the cavity system shows a slight increase in acceptor-associated emission by 1.8%. This modest enhancement in energy transfer compared to the no-cavity system suggests a less pronounced effect of the cavity on the D1-A_{nir} system.

The D2-A_{nir} cavity system demonstrates a higher percentage of acceptor-associated emission (55.7%) than the D1-A_{nir} system (51.8%). This suggests a potentially more efficient energy transfer from donor to acceptor states in the D2-A_{nir} system. The difference between acceptor- and donor-component PL is more pronounced in the D2-A_{nir} cavity system (11.4%) compared to the D1-A_{nir} system (3.6%). This larger difference in the D2-A_{nir} system indicates more effective polariton-mediated energy transfer from the donor to the acceptor. These results suggest that the polariton states in D2–A_{nir} are more effective at redistributing energy, potentially due to more favourable mixing in the MP state arising from the larger donor-acceptor exciton energy offset.

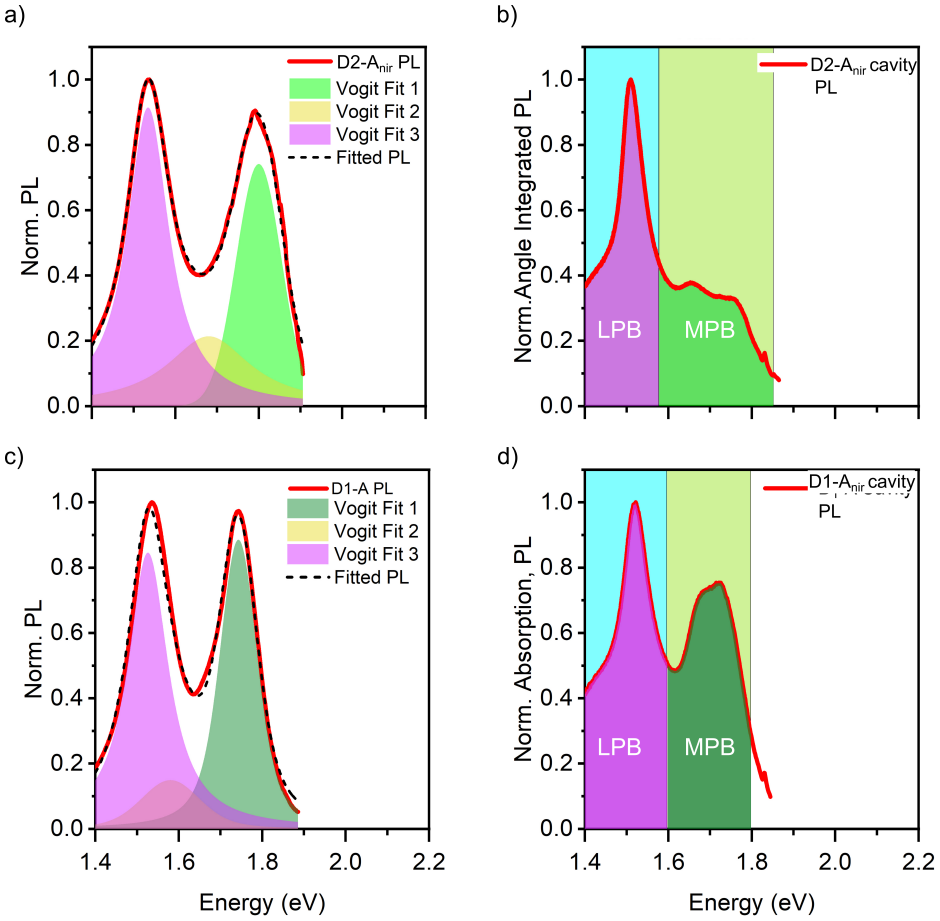

Figure 6.8. Angle integrated PL of (a) D2-A$_{nir}$ system (b) D2-A$_{nir}$ system outside the microcavity, (c) D1-A$_{nir}$ system (d) D1-A$_{nir}$ system in a microcavity, when excited at 640 nm using a laser diode. In (a) and (c), the experimental PL spectra are shown in red, PL are fitted with three Voigt profiles using Voigt fit where purple represents PL from the acceptor and green and yellow represent PL from the donor. The calculated fit is shown in a black dotted line. In (b) and (d), the shaded areas in purple and green are associated with polariton PL emission from the acceptor and donor, respectively. The cyan and yellow shaded area marks the energy range of LP and MP states, the vertical lines represent the two exciton energies of the donor and acceptor.

The analysis shows that a larger donor–acceptor exciton energy offset leads to reduced donor dominance and increased photonic fraction in the MP branch, especially at high angles. This shift in composition correlates with higher acceptor emission, indicating that MP character influences energy transfer efficiency. The LP population exceeds that of the MP across all measured angles, and the enhanced acceptor emission in the D2–A$_{nir}$ system supports a relaxation mechanism involving the MP state. These findings show that exciton energy offset is an effective parameter for tuning polariton composition and long-range energy transfer in organic microcavities.

6.6 Summary and conclusion

The influence of donor–acceptor exciton energy offset on long-range energy transfer efficiency was investigated in strongly coupled organic multilayer microcavities. Two donor–acceptor systems were selected for comparison: ATTO 655 (D2) with IRDye (A_{nir}), and ATTO 680 (D1) with IRDye (A_{nir}), differing in their donor exciton energies and resulting energy offsets relative to the common acceptor.

Spectroscopic characterisation of the isolated dyes, uncoupled multilayer reference films, and coupled microcavity structures confirmed that strong coupling was achieved in all cavity systems. The formation of three polariton branches—UP, MP and LP—was confirmed through angle-resolved reflectivity and PL measurements. A CHO model was used to extract coupling strengths and Hopfield coefficients, providing quantitative insight into the exciton–photon mixing of each polariton state.

Analysis of polariton composition and population showed that a larger donor–acceptor energy offset leads to reduced donor contribution and increased photonic character in the MP branch, especially at higher angles. In the D2–A_{nir} system, this change in composition coincided with a 7% increase in acceptor-associated emission compared to the reference film, indicating more efficient donor-to-acceptor energy transfer within the cavity.

Across both systems, the LP population consistently exceeded the MP population at all angles, supporting the presence of a relaxation pathway that preferentially populates the LP state. Comparison to uncoupled reference films showed that only under strong coupling did long-range donor-to-acceptor energy transfer become evident, as indicated by the enhanced acceptor emission.

Overall, the results demonstrate that donor–acceptor exciton energy offset is an effective tuning parameter for modulating polariton composition, particularly the degree of donor, acceptor, and photon mixing in the MP branch, without significantly affecting the LP energy. These findings establish a spectrally controllable mechanism for influencing polariton-mediated energy transfer in organic microcavities.

7. Conclusion and Outlook

This thesis has explored the potential of N-heteropolycycles as promising candidates for strong light–matter coupling in organic microcavities. These systems provide a versatile and tunable platform to investigate the formation, relaxation, and energy transfer mechanisms of exciton–polaritons, thereby contributing to the broader understanding of hybrid light–matter states in molecular materials.

The first objective of this work was to establish N-heteropolycycles as viable materials for strong light-matter coupling. Using a series of TFTAP derivatives—Butyl-, Benzyl-, and pmb TFTAP, dispersed in PS matrix and embedded in metal-clad optical microcavities, polariton formation was confirmed via angle-resolved reflectivity and PL spectroscopy. Rabi splitting energies between 40 and 241 meV were observed, values comparable to well-established organic systems such as TDBC and PDI derivatives. [3, 107, 220] Polariton properties were tuned using two complementary strategies: varying cavity thickness to control spectral detuning, and adjusting the emitter concentration to modulate the light–matter coupling strength. The observed $\sqrt{N}$ scaling of coupling strength with emitter concentration aligns with theoretical expectations [60, 221]and has been experimentally confirmed in a range of organic microcavity systems [3, 222], supporting the interpretation of collective and coherent light–matter coupling in these materials. These results demonstrate that the structural tunability, solubility, and well-defined excitonic transitions of TFTAP derivatives make them attractive, solution-processable chromophores for use in molecular polaritonics.

The second objective examined the dominant polariton relaxation pathways in systems with pronounced vibronic structure, focusing on TAC trimer systems. Strong coupling was achieved with a Rabi splitting of 36 meV in TAC–PS films embedded in a metal-clad optical microcavity. By systematically tuning the cavity resonance across a broad detuning range and analysing both angle-resolved and angle-integrated PL spectra, detuning-dependent spectral signatures were observed that suggest contributions from both RP and VAS to polariton relaxation, with their relative importance modulated by the cavity detuning. At low detuning (-8 to 50 meV), the limited spectral overlap between the LP states and the 0–0 vibronic emission band results in inefficient RP and negligible VAS contributions, leading to a low LP population. In the intermediate detuning range (64 to 156 meV), reso-

nance between the LP states and the 0–1 vibronic emission band or the 73 meV Raman-active mode enhances both RP and VAS, with the latter manifesting as sharp spectral features in PL spectra. At high detuning (above 173 meV), the interplay between broad RP-related emission and sharp VAS-related sidebands indicates that both mechanisms contribute to LP population, with reduced RP contribution due to the decreasing photonic character of high-angle LP states. These findings, interpreted using the theoretical framework of Pérez-Sánchez and Yuen-Zhou [84], underscore the critical role of vibronic coupling and detuning in controlling polariton relaxation processes in systems with rich vibrational structure. These findings support and help explain existing experimental observations in organic polariton lasing systems, where low lasing thresholds and efficient LP population are often observed under detuning conditions that favour vibronic resonance. [14, 162] In small Stokes-shifted molecules with pronounced vibronic progression, such as the TAC trimer, the LP can be populated through both RP and VAS. Unlike other small Stokes-shifted systems like TDBC, where VAS has been identified as the dominant relaxation pathway, [203] molecules exhibiting clear vibronic structure enable LP population via RP, particularly when the LP energy aligns with the 0–1 vibronic emission and via VAS when the LP states are resonant with Raman-active vibrational modes. This work establishes, through spectroscopic analysis, an understanding of how both RP and VAS are modulated by cavity detuning, offering insight into how polariton relaxation pathways might be selectively activated to support condensation and lasing in organic systems with pronounced vibrational structure.

The third objective explored how donor–acceptor (D–A) exciton energy offsets influence polariton-mediated energy transfer in multilayer organic microcavities. Two D-A configurations were investigated: ATTO 680–IRDye and ATTO 655–IRDye, using oxazine-based donor dyes with sharp absorption features and minimal Stokes shifts. While structurally similar, ATTO 655 exhibits a higher-energy excitonic transition than ATTO 680, resulting in a larger energy offset (276 meV) relative to the acceptor, compared to 199 meV for the ATTO 680–IRDye pair. The acceptor dye, IRDye (A_{nir}), is a cyanine-based molecule with strong near-infrared absorption and a narrow Stokes shift, making it well suited for strong coupling and energy transfer studies. By varying the donor exciton energy while maintaining zero detuning with respect to the acceptor, the polariton composition was systematically tuned, particularly within the MP branch. Hopfield analysis revealed that the larger D-A energy offset in the ATTO 655–IRDye system reduced donor contribution and increased the photonic content of the MP state, especially at higher angles. This shift in composition was accompanied by a greater enhancement in acceptor-associated emission: 7.0% in the ATTO 655–IRDye cavity compared to 1.8% in the ATTO 680–IRDye system, relative to their respective uncoupled reference films. Across both systems, the LP population consistently exceeded that of the MP at all measured angles, indicating a preferential relaxation path-

way into the LP state. These findings suggest that a larger exciton energy offset promotes more efficient polariton-mediated energy transfer, likely due to favourable MP-state mixing and improved redistribution of excitation energy toward the acceptor. These results highlight exciton energy offset as a versatile design parameter for modulating MP composition independently of LP energy, enabling targeted control over polariton-mediated energy transfer without altering cavity resonance. This insight offers new opportunities for developing tunable polaritonic platforms for sensing, photonic switching, and imaging applications.

While this work demonstrates the relevance of N-heteropolycycles in polaritonic applications, several promising avenues remain for future exploration. Further experimental discrimination between radiative pumping (RP) and vibrationally assisted scattering (VAS) could be achieved through dynamical techniques such as time-resolved or temperature- dependent spectroscopy, enabling a more direct assessment of the mechanisms underlying polariton relaxation. In the donor–acceptor microcavity systems, a full kinetic analysis incorporating quantum efficiency measurements or exciton diffusion modelling would offer a more quantitative understanding of energy transfer processes. Additionally, assessing the long-term operational stability, scalability, and integration of these solution-processed films into device architectures will be critical for translating these findings into practical polaritonic technologies.

In conclusion, this thesis establishes N-heteropolycycles as structurally tunable, solution-processable materials that support strong light–matter coupling and enable control over polariton relaxation and energy transfer processes. This work demonstrates that polariton behaviour in organic microcavities can be modulated through targeted molecular design (e.g., functional substitution on N-heteropolycycles), controlled emitter concentration, and precise tuning of cavity detuning. Specifically, the results show that vibronic structure enables detuning-dependent relaxation via both RP and VAS, and that donor–acceptor exciton energy offsets directly influence the composition and energy transfer efficiency of polariton states in multilayer architectures. Continued exploration of N-heteropolycycle-based systems could enable the development of tailored polaritonic materials for applications in low-threshold organic lasers, long-range exciton transport devices, and energy-harvesting platforms.

Bibliography

[1] Anthony Mark Fox. *Quantum optics: an introduction*, volume 15. Oxford university press, 2006.

[2] Lukas Novotny and Bert Hecht. *Principles of nano-optics*. Cambridge university press, 2012.

[3] David G Lidzey, DDC Bradley, MS Skolnick, T Virgili, S Walker, and DM Whittaker. Strong exciton–photon coupling in an organic semiconductor microcavity. *Nature*, 395(6697):53–55, 1998.

[4] Alexey Kavokin, Jeremy J Baumberg, Guillaume Malpuech, and Fabrice P Laussy. *Microcavities*. Oxford university press, 2017.

[5] Alexey Kavokin, Guillaume Malpuech, and Fabrice P Laussy. Polariton laser and polariton superfluidity in microcavities. *Physics Letters A*, 306(4):187–199, 2003.

[6] Bo Xiang, Raphael F Ribeiro, Yingmin Li, Adam D Dunkelberger, Blake B Simpkins, Joel Yuen-Zhou, and Wei Xiong. Manipulating optical nonlinearities of molecular polaritons by delocalization. *Science advances*, 5(9):eaax5196, 2019.

[7] Anton V Zasedatelev, Anton V Baranikov, Denis Sannikov, Darius Urbonas, Fabio Scafirimuto, Vladislav Yu Shishkov, Evgeny S Andrianov, Yurii E Lozovik, Ullrich Scherf, Thilo Stöferle, et al. Single-photon nonlinearity at room temperature. *Nature*, 597(7877):493–497, 2021.

[8] Johannes D Plumhof, Thilo Stöferle, Lijian Mai, Ullrich Scherf, and Rainer F Mahrt. Room-temperature bose–einstein condensation of cavity exciton–polaritons in a polymer. *Nature materials*, 13(3):247–252, 2014.

[9] Tim Byrnes, Na Young Kim, and Yoshihisa Yamamoto. Exciton–polariton condensates. *Nature Physics*, 10(11):803–813, 2014.

[10] Jacek Kasprzak, Murielle Richard, S Kundermann, A Baas, P Jeambrun, Jonathan Mark James Keeling, FM Marchetti, MH Szymańska, R André, JL a Staehli, et al. Bose–einstein condensation of exciton polaritons. *Nature*, 443(7110):409–414, 2006.

[11] DG Lidzey, DDC Bradley, T Virgili, A Armitage, MS Skolnick, and S Walker. Room temperature polariton emission from strongly coupled organic semiconductor microcavities. *Physical review letters*, 82(16):3316, 1999.

[12] Peter A Hobson, William L Barnes, DG Lidzey, GA Gehring, DM Whittaker, MS Skolnick, and S Walker. Strong exciton–photon coupling in a low-q all-metal mirror microcavity. *Applied Physics Letters*, 81(19):3519–3521, 2002.

[13] KS Daskalakis, SA Maier, Ray Murray, and Stéphane Kéna-Cohen. Nonlinear interactions in an organic polariton condensate. *Nature materials*, 13(3):271–278, 2014.

[14] Stéphane Kéna-Cohen and SR Forrest. Room-temperature polariton lasing in an organic single-crystal microcavity. *Nature Photonics*, 4(6):371–375, 2010.

[15] David M Coles, Qiang Chen, Lucas C Flatten, Jason M Smith, Klaus Müllen, Akimitsu Narita, and David G Lidzey. Strong exciton–photon coupling in a nanographene filled microcavity. *Nano Letters*, 17(9):5521–5525, 2017.

[16] Randy P Sabatini, Fatemeh Maasoumi, Shyamal KK Prasad, Bolong Zhang, Caspar Clark, Timothy W Schmidt, Wallace WH Wong, and Girish Lakhwani. Organic polariton lasing with molecularly isolated perylene diimides. *Applied Physics Letters*, 117(4), 2020.

[17] Kyriacos Georgiou, Rahul Jayaprakash, Andreas Othonos, and David G Lidzey. Ultralong-range polariton-assisted energy transfer in organic microcavities. *Angewandte Chemie*, 133(30):16797–16803, 2021.

[18] Heba Megahd, Davide Comoretto, and Paola Lova. Planar microcavities: Materials and processing for light control. *Optical Materials: X*, 13:100130, 2022.

[19] Alfred Pérot and Charles Fabry. On the application of interference phenomena to the solution of various problems of spectroscopy and metrology. *Astrophysical Journal, vol. 9, p. 87*, 9:87, 1899.

[20] Nur Ismail, Cristine Calil Kores, Dimitri Geskus, and Markus Pollnau. Fabry-pérot resonator: spectral line shapes, generic and related airy distributions, linewidths, finesses, and performance at low or frequency-dependent reflectivity. *Optics express*, 24(15):16366–16389, 2016.

[21] Bei Zhang, Yong Ma, Min Xu, Ke Wu, Chunhui Huang, Yilei Zhao, Dejiang Zhuo, Liming Yin, and Xinsheng Zhao. Planar organic microcavity of eu-chelate film with metal mirrors. *Solid state communications*, 104(10):593–596, 1997.

[22] Yong Lin, Bei-Wei Zhang, Guozhong Wang, Lu Sun, Shulin Zhang, Xinzhang Li, Yanyi Huang, and Chunhui Huang. Planar organic microcavity of rare-earth tb complex film with metal mirrors. In *Semiconductor Lasers III*, volume 3547, pages 186–190. SPIE, 1998.

[23] Yilei Zhao, Dejian Zhou, Chunhui Huang, Liangbing Gan, Liming Ying, Xinsheng Zhao, Bei Zhang, Yong Ma, Ming Xu, and Ke Wu. Langmuir- blodgett film of a europium complex and its application in a silver mirror planar microcavity. *Langmuir*, 14(2):417–422, 1998.

[24] H Becker, SE Burns, N Tessler, and RH Friend. Role of optical properties of metallic mirrors in microcavity structures. *Journal of Applied Physics*, 81(6):2825–2829, 1997.

[25] Andrew Strang, Victoria Quirós-Cordero, Pascal Grégoire, Sara Pla, Fernando Fernández-Lázaro, Ángela Sastre-Santos, Carlos Silva-Acuña, Paul N Stavrinou, and Natalie Stingelin. Simple and versatile platforms for manipulating light with matter: Strong light–matter coupling in fully solution-processed optical microcavities. *Advanced Materials*, 36(20):2212056, 2024.

[26] Yongsheng Hu, Fatima Bencheikh, Sébastien Chénais, Sébastien Forget, Xingyuan Liu, and Chihaya Adachi. High performance planar microcavity organic semiconductor lasers based on thermally evaporated top distributed bragg reflector. *Applied Physics Letters*, 117(15), 2020.

[27] H Benisty, Hans De Neve, and Cl Weisbuch. Impact of planar microcavity effects on light extraction-part i: Basic concepts and analytical trends. *IEEE Journal of quantum electronics*, 34(9):1612–1631, 1998.

[28] H Becker, RH Friend, and TD Wilkinson. Light emission from wavelength-tunable microcavities. *Applied physics letters*, 72(11):1266–1268, 1998.

[29] Ekraj Dahal, David Allemeier, Benjamin Isenhart, Karen Cianciulli, and Matthew S White. Characterization of higher harmonic modes in fabry–pérot microcavity organic light emitting diodes. *Scientific reports*, 11(1):8456, 2021.

[30] Jia Li, Qieni Lu, Haitao Dai, ZhenDa Chen, Yikai Fu, and Xiaopeng Chen. Tricolor narrowband planar perovskite photodetectors based on fp microcavity structure. *Optics Express*, 31(19):30578–30587, 2023.

[31] Giovanna Panzarini, Lucio Claudio Andreani, A Armitage, D Baxter, MS Skolnick, VN Astratov, JS Roberts, Alexey V Kavokin, Maria R Vladimirova, and MA Kaliteevski. Cavity-polariton dispersion and polarization splitting in single and coupled semiconductor microcavities. *Physics of the Solid State*, 41:1223–1238, 1999.

[32] T Virgili, DG Lidzey, DDC Bradley, and S Walker. Cavity mode polarisation splitting in organic semiconductor microcavities. *Synthetic metals*, 116(1-3):497–500, 2001.

[33] David G Lidzey and David M Coles. Strong coupling in organic and hybrid-semiconductor microcavity structures. *Organic and Hybrid Photonic Crystals*, pages 243–273, 2015.

[34] Arko Graf, Laura Tropf, Yuriy Zakharko, Jana Zaumseil, and Malte C Gather. Near-infrared exciton-polaritons in strongly coupled single-walled carbon nanotube microcavities. *Nature communications*, 7(1):13078, 2016.

[35] Bin Liu, Prabin Rai, John Grezmak, Robert J Twieg, and Kenneth D Singer. Coupling of exciton-polaritons in low-q coupled microcavities beyond the rotating wave approximation. *Physical Review B*, 92(15):155301, 2015.

[36] David M Coles, Niccolo Somaschi, Paolo Michetti, Caspar Clark, Pavlos G Lagoudakis, Pavlos G Savvidis, and David G Lidzey. Polariton-mediated energy transfer between organic dyes in a strongly coupled optical microcavity. *Nature materials*, 13(7):712–719, 2014.

[37] E Hulkko, S Pikker, V Tiainen, RH Tichauer, G Groenhof, and JJ Toppari. Effect of molecular stokes shift on polariton dynamics. *The Journal of Chemical Physics*, 154(15), 2021.

[38] R Coccioli, M Boroditsky, KW Kim, Y Rahmat-Samii, and E Yablonovitch. Smallest possible electromagnetic mode volume in a dielectric cavity. *IEE Proceedings-Optoelectronics*, 145(6):391–397, 1998.

[39] Davide Comoretto et al. *Organic and hybrid photonic crystals*, volume 21. Springer, 2015.

[40] Denis Sannikov, Timur Yagafarov, Kyriacos Georgiou, Anton Zasedatelev, Anton Baranikov, Lizhi Gai, Zhen Shen, David Lidzey, and Pavlos Lagoudakis. Room tem-

perature broadband polariton lasing from a dye-filled microcavity. *Advanced Optical Materials*, 7(17):1900163, 2019.

[41] LG Connolly, DG Lidzey, R Butte, AM Adawi, DM Whittaker, MS Skolnick, and R Airey. Strong coupling in high-finesse organic semiconductor microcavities. *Applied physics letters*, 83(26):5377–5379, 2003.

[42] Hassan A Qureshi, Michael A Papachatzakis, Ahmed Gaber Abdelmagid, Mikko Salomäki, Ermei Mäkilä, Olli Siltanen, and Konstantinos S Daskalakis. Giant rabi splitting and polariton photoluminescence in an all solution-deposited dielectric microcavity. *arXiv preprint arXiv:2410.19392*, 2024.

[43] Julia Benedikter, Thea Moosmayer, Matthias Mader, Thomas Hümmer, and David Hunger. Transverse-mode coupling effects in scanning cavity microscopy. *New Journal of Physics*, 21(10):103029, 2019.

[44] Arpan Dutta, Ville Tiainen, and J Jussi Toppari. Optimizing geometry of low-q all-metal fabry-pérot microcavity for fluorescence spectroscopy. *IOP SciNotes*, 2(1):015205, 2021.

[45] Leandro N Acquaroli. Matrix method for thin film optics. *arXiv preprint arXiv:1809.07708*, 2018.

[46] Karol Sajnok and MichaĹ Matuszewski. Modeling nonlinear optics with the transfer matrix method. *arXiv preprint arXiv:2502.06496*, 2025.

[47] RF Oulton, N Takada, J Koe, PN Stavrinou, and DDC Bradley. Strong coupling in organic semiconductor microcavities. *Semiconductor science and technology*, 18(10):S419, 2003.

[48] François Médard, Jesús Zúñiga-Pérez, Pierre Disseix, Martine Mihailovic, Joël Leymarie, Aime Vasson, Fabrice Semond, Eric Frayssinet, Jean-Christophe Moreno, Mathieu Leroux, et al. Experimental observation of strong light-matter coupling in zno microcavities: Influence of large excitonic absorption. *Physical Review B—Condensed Matter and Materials Physics*, 79(12):125302, 2009.

[49] D Keskar, S Survase, and M Thakurdesai. Reflectivity simulation by using transfer matrix method. In *Journal of Physics: Conference Series*, volume 1913, page 012051. IOP Publishing, 2021.

[50] M Claudia Troparevsky, Adrian S Sabau, Andrew R Lupini, and Zhenyu Zhang. Transfer-matrix formalism for the calculation of optical response in multilayer sys-

tems: from coherent to incoherent interference. *Optics express*, 18(24):24715–24721, 2010.

[51] Pooja Bhatt, Kuljeet Kaur, and Jino George. Enhanced charge transport in two-dimensional materials through light–matter strong coupling. *ACS nano*, 15(8):13616–13622, 2021.

[52] Arpan Dutta, Ville Tiainen, Luis Duarte, Nemanja Markesevic, Ilia Sokolovskii, Dmitry Morozov, Hassan A Qureshi, Siim Pikker, Gerrit Groenhof, and J Jussi Toppari. Ultra-fast photochemistry in the strong light-matter coupling regime. 2024.

[53] Valerio Lucarini, Jarkko J Saarinen, Kai-Erik Peiponen, and Erik M Vartiainen. *Kramers-Kronig relations in optical materials research*, volume 110. Springer, 2005.

[54] WRM Rocha and S Pilling. Determination of optical constants n and k of thin films from absorbance data using kramers–kronig relationship. *Spectrochimica Acta Part A: Molecular and Biomolecular Spectroscopy*, 123:436–446, 2014.

[55] Leif AA Pettersson, Lucimara S Roman, and Olle Inganäs. Modeling photocurrent action spectra of photovoltaic devices based on organic thin films. *Journal of Applied Physics*, 86(1):487–496, 1999.

[56] G Yin, C Merschjann, and Martina Schmid. The effect of surface roughness on the determination of optical constants of cuinse2 and cugase2 thin films. *Journal of Applied Physics*, 113(21), 2013.

[57] Thibault Chervy. *Strong coupling regime of cavity quantum electrodynamics and its consequences on molecules and materials*. PhD thesis, Université de Strasbourg, 2017.

[58] Chunxiu Zang, Shihao Liu, Mengxin Xu, Ruifang Wang, Chen Cao, Zelin Zhu, Jiaming Zhang, Hui Wang, Letian Zhang, Wenfa Xie, et al. Top-emitting thermally activated delayed fluorescence organic light-emitting devices with weak light-matter coupling. *Light: science & applications*, 10(1):116, 2021.

[59] Shovasis Kumar Biswas, Wihan Adi, Aidana Beisenova, Samir Rosas, Eduardo Romero Arvelo, and Filiz Yesilkoy. From weak to strong coupling: quasi-bic metasurfaces for mid-infrared light–matter interactions. *Nanophotonics*, 13(16):2937–2949, 2024.

[60] Päivi Törmä and William L Barnes. Strong coupling between surface plasmon polaritons and emitters: a review. *Reports on Progress in Physics*, 78(1):013901, 2014.

[61] Lukas Novotny. Strong coupling, energy splitting, and level crossings: A classical perspective. *American Journal of Physics*, 78(11):1199–1202, 2010.

[62] Edwin T Jaynes and Frederick W Cummings. Comparison of quantum and semiclassical radiation theories with application to the beam maser. *Proceedings of the IEEE*, 51(1):89–109, 1963.

[63] Bruce W Shore and Peter L Knight. The jaynes-cummings model. *Journal of Modern Optics*, 40(7):1195–1238, 1993.

[64] Bruce J West and Katja Lindenberg. On the rotating wave approximation. *Physics Letters A*, 102(4):189–193, 1984.

[65] Li Xiao-Hong, Wang Ke-Lin, and Liu Tao. Ground state of jaynes–cummings model: comparison of solutions with and without the rotating-wave approximation. *Chinese Physics Letters*, 26(4):044212, 2009.

[66] Jonas Larson and Themistoklis Mavrogordatos. *The Jaynes–Cummings model and its descendants: modern research directions*. IoP Publishing, 2021.

[67] D Meschede, Herbert Walther, and G Müller. One-atom maser. *Physical review letters*, 54(6):551, 1985.

[68] Martin Blaha, Aisling Johnson, Arno Rauschenbeutel, and Jürgen Volz. Beyond the tavis-cummings model: Revisiting cavity qed with ensembles of quantum emitters. *Physical Review A*, 105(1):013719, 2022.

[69] Michael Tavis and Frederick W Cummings. Exact solution for an n-molecule—radiation-field hamiltonian. *Physical Review*, 170(2):379, 1968.

[70] Robert H Dicke. Coherence in spontaneous radiation processes. *Physical review*, 93(1):99, 1954.

[71] Jonathan D Breeze, Enrico Salvadori, Juna Sathian, Neil McN Alford, and Christopher WM Kay. Room-temperature cavity quantum electrodynamics with strongly coupled dicke states. *npj Quantum Information*, 3(1):40, 2017.

[72] Paolo Michetti, Leonardo Mazza, and Giuseppe C La Rocca. Strongly coupled organic microcavities. In *Organic Nanophotonics: Fundamentals and Applications*, pages 39–68. Springer, 2014.

[73] D Meiser and P Meystre. Superstrong coupling regime of cavity quantum electrodynamics. *Physical Review A—Atomic, Molecular, and Optical Physics*, 74(6):065801, 2006.

[74] Aisling Johnson, Martin Blaha, Alexander E Ulanov, Arno Rauschenbeutel, Philipp Schneeweiss, and Jürgen Volz. Observation of collective superstrong coupling of cold atoms to a 30-m long optical resonator. *Physical review letters*, 123(24):243602, 2019.

[75] MS Skolnick, TA Fisher, and DM Whittaker. Strong coupling phenomena in quantum microcavity structures. *Semiconductor Science and Technology*, 13(7):645, 1998.

[76] Braden M Weight, Xinyang Li, and Yu Zhang. Theory and modeling of light-matter interactions in chemistry: current and future. *Physical Chemistry Chemical Physics*, 25(46):31554–31577, 2023.

[77] RJ Holmes and SR Forrest. Strong exciton-photon coupling and exciton hybridization in a thermally evaporated polycrystalline film of an organic small molecule. *Physical review letters*, 93(18):186404, 2004.

[78] Tobias Wesp, Parvathi Valsalan, Alexander Kochan, Manuel Hertzog, Hubert Wadepohl, Jana Zaumseil, and Lutz H. Gade. Peri-functionalized tetraazaperylenes: Strong emitters for molecular polaritonics. *Chemistry – A European Journal*, 28(71):e202202661, 2022.

[79] Thomas W Ebbesen. Hybrid light–matter states in a molecular and material science perspective. *Accounts of chemical research*, 49(11):2403–2412, 2016.

[80] Galina Khitrova, HM Gibbs, M Kira, Stephan W Koch, and Axel Scherer. Vacuum rabi splitting in semiconductors. *Nature physics*, 2(2):81–90, 2006.

[81] Michael R Philpott. Theory of vibronic coupling in the polariton states of molecular crystals. *The Journal of Chemical Physics*, 52(11):5842–5850, 1970.

[82] Wenxiang Ying and Pengfei Huo. Resonance theory of vibrational strong coupling enhanced polariton chemistry and the role of photonic mode lifetime. *Communications Materials*, 5(1):110, 2024.

[83] Andreas Maser, Benjamin Gmeiner, Tobias Utikal, Stephan Götzinger, and Vahid Sandoghdar. Few-photon coherent nonlinear optics with a single molecule. *Nature Photonics*, 10(7):450–453, 2016.

[84] Juan B Pérez-Sánchez and Joel Yuen-Zhou. Radiative pumping vs vibrational relaxation of molecular polaritons: A bosonic mapping approach. *Nature Communications*, 16(1):3151, 2025.

[85] R Houdré, RP Stanley, and M Ilegems. Vacuum-field rabi splitting in the presence of inhomogeneous broadening: Resolution of a homogeneous linewidth in an inhomogeneously broadened system. *Physical Review A*, 53(4):2711, 1996.

[86] Shaojun Wang, Thibault Chervy, Jino George, James A Hutchison, Cyriaque Genet, and Thomas W Ebbesen. Quantum yield of polariton emission from hybrid light-matter states. *The journal of physical chemistry letters*, 5(8):1433–1439, 2014.

[87] Wonmi Ahn, Igor Vurgaftman, Adam D Dunkelberger, Jeffrey C Owrutsky, and Blake S Simpkins. Vibrational strong coupling controlled by spatial distribution of molecules within the optical cavity. *ACS Photonics*, 5(1):158–166, 2018.

[88] Franziska Wall, Oliver Mey, Lorenz Maximilian Schneider, and Arash Rahimi-Iman. Continuously-tunable light–matter coupling in optical microcavities with 2d semiconductors. *Scientific Reports*, 10(1):8303, 2020.

[89] M Litinskaya, P Reineker, and VM Agranovich. Exciton–polaritons in organic microcavities. *Journal of luminescence*, 119:277–282, 2006.

[90] Gerhard Rempe, Herbert Walther, and Norbert Klein. Observation of quantum collapse and revival in a one-atom maser. *Physical review letters*, 58(4):353, 1987.

[91] Claude Weisbuch, Mr Nishioka, A Ishikawa, and Y Arakawa. Observation of the coupled exciton-photon mode splitting in a semiconductor quantum microcavity. *Physical review letters*, 69(23):3314, 1992.

[92] WY Liang. Excitons. *Physics Education*, 5(4):226, 1970.

[93] Galina Khitrova, HM Gibbs, Frank Jahnke, Mackillo Kira, and Stephan W Koch. Nonlinear optics of normal-mode-coupling semiconductor microcavities. *Reviews of Modern Physics*, 71(5):1591, 1999.

[94] E Yablonovitch, TJ Gmitter, and R Bhat. Inhibited and enhanced spontaneous emission from optically thin algaas/gaas double heterostructures. *Physical review letters*, 61(22):2546, 1988.

[95] R Huang, Y Yamamoto, Régis André, J Bleuse, M Muller, and H Ulmer-Tuffigo. Exciton-polariton lasing and amplification based on exciton-exciton scattering in cdte microcavity quantum wells. *Physical Review B*, 65(16):165314, 2002.

[96] J-G Rousset, Barbara Piętka, Mateusz Król, Rafał Mirek, Katarzyna Lekenta, Jacek Szczytko, Jolanta Borysiuk, J Suffczyński, Tomasz Kazimierczuk, Mateusz Goryca,

et al. Strong coupling and polariton lasing in te based microcavities embedding (cd, zn) te quantum wells. *Applied Physics Letters*, 107(20), 2015.

[97] Guillaume Malpuech, Aldo Di Carlo, Alexey Kavokin, Jeremy J Baumberg, Marian Zamfirescu, and Paolo Lugli. Room-temperature polariton lasers based on gan microcavities. *Applied physics letters*, 81(3):412–414, 2002.

[98] E Feltin, G Christmann, R Butté, J-F Carlin, M Mosca, and N Grandjean. Room temperature polariton luminescence from a gan/ algan quantum well microcavity. *Applied physics letters*, 89(7), 2006.

[99] S Christopoulos, G Baldassarri Höger Von Högersthal, AJD Grundy, <? format?> PG Lagoudakis, AV Kavokin, JJ Baumberg, G Christmann, R Butté, E Feltin, J-F Carlin, et al. Room-temperature polariton lasing in semiconductor microcavities. *Physical review letters*, 98(12):126405, 2007.

[100] Gabriel Christmann, Raphaël Butté, Eric Feltin, Anas Mouti, Pierre A Stadelmann, Antonino Castiglia, Jean-François Carlin, and Nicolas Grandjean. Large vacuum rabi splitting in a multiple quantum well gan-based microcavity in the strong-coupling regime. *Physical Review B—Condensed Matter and Materials Physics*, 77(8):085310, 2008.

[101] Aurélien Trichet, François Médard, J Zúñiga-Pérez, B Alloing, and Maxime Richard. From strong to weak coupling regime in a single gan microwire up to room temperature. *New Journal of Physics*, 14(7):073004, 2012.

[102] Jun-Rong Chen, Tien-Chang Lu, Yung-Chi Wu, Shiang-Chi Lin, Wen-Feng Hsieh, Shing-Chung Wang, and Hui Deng. Characteristics of exciton-polaritons in zno-based hybrid microcavities. *Optics express*, 19(5):4101–4112, 2011.

[103] Tien-Chang Lu, Ying-Yu Lai, Yu-Pin Lan, Si-Wei Huang, Jun-Rong Chen, Yung-Chi Wu, Wen-Feng Hsieh, and Hui Deng. Room temperature polariton lasing vs. photon lasing in a zno-based hybrid microcavity. *Optics express*, 20(5):5530–5537, 2012.

[104] P Schouwink, H Von Berlepsch, L Dähne, and RF Mahrt. Observation of strong exciton–photon coupling in an organic microcavity in transmission and photoluminescence. *Journal of luminescence*, 94:821–826, 2001.

[105] Noriyuki Takada, Toshihide Kamata, and Donal DC Bradley. Polariton emission from polysilane-based organic microcavities. *Applied physics letters*, 82(12):1812–1814, 2003.

[106] Tal Schwartz, James A Hutchison, Cyriaque Genet, and Thomas W Ebbesen. Reversible switching of ultrastrong light-molecule coupling. *Physical review letters*, 106(19):196405, 2011.

[107] Randy P Sabatini, Bolong Zhang, Akhil Gupta, Julien Leoni, Wallace WH Wong, and Girish Lakhwani. Molecularly isolated perylene diimides enable both strong exciton–photon coupling and high photoluminescence quantum yield. *Journal of Materials Chemistry C*, 7(10):2954–2960, 2019.

[108] Stéphane Kéna-Cohen, Stefan A Maier, and Donal DC Bradley. Ultrastrongly coupled exciton–polaritons in metal-clad organic semiconductor microcavities. *Advanced Optical Materials*, 1(11):827–833, 2013.

[109] Ahmed Dkhissi. Excitons in organic semiconductors. *Synthetic metals*, 161(13-14):1441–1443, 2011.

[110] Anna Köhler and Heinz Bässler. *Electronic processes in organic semiconductors: An introduction*. John Wiley & Sons, 2015.

[111] Peter William Atkins, Julio De Paula, and James Keeler. *Atkins' physical chemistry*. Oxford university press, 2023.

[112] Nicholas J Turro. *Modern molecular photochemistry*. University science books, 1991.

[113] Gerhard Herzberg. Molecular spectra and molecular structure. vol. 1: Spectra of diatomic molecules. *New York: Van Nostrand Reinhold*, 1950.

[114] Martin Pope and Charlese E Swenberg. *Electronic processes in organic crystals and polymers*. Oxford University Press, 1999.

[115] Heinz Bässler. Charge transport in disordered organic photoconductors. a monte carlo simulation study. *Physica Status Solidi B (Basic Research);(Germany)*, 175(1), 1993.

[116] Hung-Sen Wei, Cheng-Chung Jaing, Yan-Ting Chen, Chen-Chih Lin, Ching-Wei Cheng, Chia-Hua Chan, Cheng-Chung Lee, and Jui-Fen Chang. Adjustable exciton-photon coupling with giant rabi-splitting using layer-by-layer j-aggregate thin films in all-metal mirror microcavities. *Optics express*, 21(18):21365–21373, 2013.

[117] Andrea Camposeo, Luana Persano, Pompilio Del Carro, Tersilla Virgili, Roberto Cingolani, and Dario Pisignano. Polarization splitting in organic-based microcavities working in the strong coupling regime. *Organic electronics*, 8(2-3):114–119, 2007.

[118] Robert Eichelmann, Pierre Jeudy, Lars Schneider, Jonathan Zerhoch, Paula R Mayer, Joachim Ballmann, Felix Deschler, and Lutz H Gade. Chiral bay-alkynylated tetraazaperylenes: Photophysics and chiroptical properties. *Organic Letters*, 26(6):1172–1177, 2024.

[119] Sonja Geib, Susanne C Martens, Michaela Märken, Arina Rybina, Hubert Wadepohl, and Lutz H Gade. Tuning redox chemistry and photophysics in core-substituted tetraazaperopyrenes (tapps). *Chemistry–A European Journal*, 19(41):13811–13822, 2013.

[120] Till Riehm, Gabriele De Paoli, Asgeir E Konradsson, Luisa De Cola, Hubert Wadepohl, and Lutz H Gade. Tetraazaperopyrenes: a new class of multifunctional chromophores. *Chemistry–A European Journal*, 13(26):7317–7329, 2007.

[121] Manuel Hertzog, Robert Eichelmann, Pierre Jeudy, Tobias Wesp, Joachim Ballmann, Simon Settele, Finn L Sebastian, Andreas Mischok, Florian Le Roux, Francisco Tenopala-Carmona, et al. Bay-substituted octaazaperopyrenedioxides as solid-state emitters for strong light-matter coupling. *Journal of Materials Chemistry C*, 12(8):2745–2755, 2024.

[122] Robert Eichelmann, Joël Monti, Li-Yun Hsu, Finn Kröger, Joachim Ballmann, Eva Blasco, and Lutz H Gade. Two-photon microprinting of 3d emissive structures using tetraazaperylene-derived fluorophores. *Molecular Systems Design & Engineering*, 8(12):1470–1476, 2023.

[123] Yuezeng Su, Wei Xu, Feng Qiu, Dongqing Wu, Ping Liu, Minzhao Xue, and Fan Zhang. Synthesis and physical properties of benzopyridazine-based conjugated molecules. *Chinese Journal of Chemistry*, 31(11):1397–1403, 2013.

[124] Stefan Durben and Thomas Baumgartner. Azadibenzophospholes: Functional building blocks with pronounced electron-acceptor character. *Inorganic Chemistry*, 50(14):6823–6836, 2011.

[125] Zhongyi Zeng, Hongming Jin, Kohei Sekine, Matthias Rudolph, Frank Rominger, and A Stephen K Hashmi. Gold-catalyzed regiospecific c- h annulation of o-ethynylbiaryls with anthranils: π-extension by ring-expansion en route to n-doped pahs. *Angewandte Chemie International Edition*, 57(23):6935–6939, 2018.

[126] Christopher Hüßler, Justin Kahle, Martin C Dietl, Petra Krämer, Frank Rominger, Matthias Rudolph, and A Stephen K Hashmi. Facile two-step synthesis of paradithienopyrazines. *Organic Chemistry Frontiers*, 10(15):3726–3731, 2023.

[127] Reza Dabestani and Ilia N Ivanov. A compilation of physical, spectroscopic and photophysical properties of polycyclic aromatic hydrocarbons. *Photochemistry and photobiology*, 70(1):10–34, 1999.

[128] Lena Hahn, Simin Öz, Hubert Wadepohl, and Lutz H Gade. Highly emissive water-soluble tetraazaperopyrenes as fluorescent markers. *Chemical Communications*, 50(38):4941–4943, 2014.

[129] Wei Wang, Xiaodan Miao, Guilong Cai, Li Ding, Yawen Li, Tengfei Li, Yufan Zhu, Liting Tao, Yixiao Jia, Yuanxin Liang, et al. Enhancing transition dipole moments of heterocyclic semiconductors via rational nitrogen-substitution for sensitive near infrared detection. *Advanced Materials*, 34(28):2201600, 2022.

[130] Lutz H Gade, Christian H Galka, René M Williams, Luisa De Cola, Mary McPartlin, Bin Dong, Lifeng Chi, et al. Synthesis, photophysical properties, and nanocrystal formation of a new class of tetra-n-substituted perylenes. *ANGEWANDTE CHEMIE. INTERNATIONAL EDITION*, 42(23):2677–2681, 2003.

[131] Tobias Wesp, Tim Bruckhoff, Hubert Wadepohl, and Lutz H Gade. Peri-decoration of a tetraazaperylene with urea units: Chiral octaazaperopyrenedioxides (oappdos) and their optical and chiroptical properties. *Chemistry–A European Journal*, 28(53):e202201706, 2022.

[132] Lutz H Gade, Christian H Galka, Konrad W Hellmann, René M Williams, Luisa De Cola, Ian J Scowen, and Mary McPartlin. Tetraaminoperylenes: their efficient synthesis and physical properties. *Chemistry–A European Journal*, 8(16):3732–3746, 2002.

[133] Robert Eichelmann, Daniel Rippel, Joachim Ballmann, and Lutz H Gade. Zipping up tetraazaperylene: synthesis of tetraazacoronenes via double coupling in the bay positions. *Chemical Communications*, 59(81):12136–12139, 2023.

[134] Pernille A Jensen, Mirko Leccese, Frederik DS Simonsen, Anders W Skov, Matteo Bonfanti, John D Thrower, Rocco Martinazzo, and Liv Hornekær. Identification of stable configurations in the superhydrogenation sequence of polycyclic aromatic hydrocarbon molecules. *Monthly Notices of the Royal Astronomical Society*, 486(4):5492–5498, 2019.

[135] Alexander H Endres, Manuel Schaffroth, Fabian Paulus, Hilmar Reiss, Hubert Wadepohl, Frank Rominger, Roland Krämer, and Uwe HF Bunz. Coronene-containing n-heteroarenes: 13 rings in a row. *Journal of the American Chemical Society*, 138(6):1792–1795, 2016.

[136] Xuan Yang, Frank Rominger, and Michael Mastalerz. Contorted heteroannulated tetraareno [a, d, j, m] coronenes. *Chemistry–A European Journal*, 27(57):14345–14352, 2021.

[137] Agnieszka Nowak-Król and Frank Würthner. Progress in the synthesis of perylene bisimide dyes. *Organic Chemistry Frontiers*, 6(8):1272–1318, 2019.

[138] Thomas Brietzke, Wulfhard Mickler, Alexandra Kelling, and Hans-Jürgen Holdt. Mono-and dinuclear ruthenium (ii) 1, 6, 7, 12-tetraazaperylene complexes. *Dalton Transactions*, 41(9):2788–2797, 2012.

[139] Denis S Baranov, Mikhail N Uvarov, Evgeni M Glebov, Danil A Nevostruev, Maxim S Kazantsev, Evgeny A Mostovich, Dmitry S Fadeev, Olga V Antonova, Dmitriy E Utkin, Polina A Kuchinskaya, et al. 1, 3, 7, 9-tetraazaperylene frameworks: Synthesis, photoluminescence properties, and thin film morphology. *Dyes and Pigments*, 150:252–260, 2018.

[140] Masayoshi Takase, Tomoyuki Narita, Wataru Fujita, Motoko S Asano, Tohru Nishinaga, Hiroaki Benten, Kenji Yoza, and Klaus Müllen. Pyrrole-fused azacoronene family: the influence of replacement with dialkoxybenzenes on the optical and electronic properties in neutral and oxidized states. *Journal of the American Chemical Society*, 135(21):8031–8040, 2013.

[141] Bo He, Andrew B Pun, Liana M Klivansky, Alexandra M McGough, Yifan Ye, Junfa Zhu, Jinghua Guo, Simon J Teat, and Yi Liu. Thiophene fused azacoronenes: regioselective synthesis, self-organization, charge transport and its incorporation in conjugated polymers. *Chemistry of Materials*, 26(13):3920–3927, 2014.

[142] Bo He, Jing Dai, Danylo Zherebetskyy, Teresa L Chen, Benjamin A Zhang, Simon J Teat, Qichun Zhang, Linwang Wang, and Yi Liu. A divergent route to core-and peripherally functionalized diazacoronenes that act as colorimetric and fluorescence proton sensors. *Chemical Science*, 6(5):3180–3186, 2015.

[143] Marika Żyła-Karwowska, Halina Zhylitskaya, Joanna Cybińska, Tadeusz Lis, Piotr J Chmielewski, and Marcin Stępień. An electron-deficient azacoronene obtained by radial π extension. *Angewandte Chemie*, 128(47):14878–14882, 2016.

[144] Robert Eichelmann, Joachim Ballmann, and Lutz H Gade. Tetraazacoronenes and their dimers, trimers and tetramers. *Angewandte Chemie International Edition*, 62(35):e202309198, 2023.

[145] Scott Fleming, Andrew Mills, and Tell Tuttle. Predicting the uv–vis spectra of oxazine dyes. *Beilstein journal of organic chemistry*, 7(1):432–441, 2011.

[146] Xi Chen, Xiangyu Wang, Fang Huang, and Donghan Ma. Multicolor single-molecule localization microscopy: review and prospect. *PhotoniX*, 5(1):29, 2024.

[147] Sebastian van de Linde, Mike Heilemann, and Markus Sauer. Live-cell super-resolution imaging with synthetic fluorophores. *Annual review of physical chemistry*, 63(1):519–540, 2012.

[148] Sebastian van de Linde, Robert Kasper, Mike Heilemann, and Markus Sauer. Photoswitching microscopy with standard fluorophores. *Applied Physics B*, 93:725–731, 2008.

[149] Graham T Dempsey, Joshua C Vaughan, Kok Hao Chen, Mark Bates, and Xiaowei Zhuang. Evaluation of fluorophores for optimal performance in localization-based super-resolution imaging. *Nature methods*, 8(12):1027–1036, 2011.

[150] Volker Buschmann, Kenneth D Weston, and Markus Sauer. Spectroscopic study and evaluation of red-absorbing fluorescent dyes. *Bioconjugate chemistry*, 14(1):195–204, 2003.

[151] Nicole Marmé, Jens-Peter Knemeyer, Markus Sauer, and Jürgen Wolfrum. Inter-and intramolecular fluorescence quenching of organic dyes by tryptophan. *Bioconjugate chemistry*, 14(6):1133–1139, 2003.

[152] Lucjan Strekowski. *Heterocyclic polymethine dyes: synthesis, properties and applications*, volume 14. Springer, 2008.

[153] Monserrat Llaguno-Munive, Wilberto Villalba-Abascal, Alejandro Avilés-Salas, and Patricia Garcia-Lopez. Near-infrared fluorescence imaging in preclinical models of glioblastoma. *Journal of Imaging*, 9(10):212, 2023.

[154] Jessica A Carr, Daniel Franke, Justin R Caram, Collin F Perkinson, Mari Saif, Vasileios Askoxylakis, Meenal Datta, Dai Fukumura, Rakesh K Jain, Moungi G Bawendi, et al. Shortwave infrared fluorescence imaging with the clinically approved near-infrared dye indocyanine green. *Proceedings of the National Academy of Sciences*, 115(17):4465–4470, 2018.

[155] Jonathan R Tischler, M Scott Bradley, Vladimir Bulović, Jung Hoon Song, and Arto Nurmikko. Strong coupling in a microcavity led. *Physical review letters*, 95(3):036401, 2005.

[156] DG Lidzey, AM Fox, MD Rahn, MS Skolnick, VM Agranovich, and S Walker. Experimental study of light emission from strongly coupled organic semiconductor microcavities following nonresonant laser excitation. *Physical Review B*, 65(19):195312, 2002.

[157] Hui Deng, Gregor Weihs, Charles Santori, Jacqueline Bloch, and Yoshihisa Yamamoto. Condensation of semiconductor microcavity exciton polaritons. *Science*, 298(5591):199–202, 2002.

[158] Tersilla Virgili, D Coles, AM Adawi, C Clark, P Michetti, SK Rajendran, Daniele Brida, Dario Polli, G Cerullo, and DG Lidzey. Ultrafast polariton relaxation dynamics in an organic semiconductor microcavity. *Physical Review B—Condensed Matter and Materials Physics*, 83(24):245309, 2011.

[159] David M Coles, Paolo Michetti, Caspar Clark, Ali M Adawi, and David G Lidzey. Temperature dependence of the upper-branch polariton population in an organic semiconductor microcavity. *Physical Review B—Condensed Matter and Materials Physics*, 84(20):205214, 2011.

[160] J Chovan, IE Perakis, S Ceccarelli, and DG Lidzey. Controlling the interactions between polaritons and molecular vibrations in strongly coupled organic semiconductor microcavities. *Physical Review B—Condensed Matter and Materials Physics*, 78(4):045320, 2008.

[161] David M Coles, Paolo Michetti, Caspar Clark, Wing Chung Tsoi, Ali M Adawi, Ji-Seon Kim, and David G Lidzey. Vibrationally assisted polariton-relaxation processes in strongly coupled organic-semiconductor microcavities. *Advanced Functional Materials*, 21(19):3691–3696, 2011.

[162] Richard T Grant, Paolo Michetti, Andrew J Musser, Pascal Gregoire, Tersilla Virgili, Eleonora Vella, Marco Cavazzini, Kyriacos Georgiou, Francesco Galeotti, Caspar Clark, et al. Efficient radiative pumping of polaritons in a strongly coupled microcavity by a fluorescent molecular dye. *Advanced Optical Materials*, 4(10):1615–1623, 2016.

[163] Jan M Lüttgens, Felix J Berger, and Jana Zaumseil. Population of exciton–polaritons via luminescent sp3 defects in single-walled carbon nanotubes. *ACS photonics*, 8(1):182–193, 2020.

[164] Yoichi Sasaki, Kyriacos Georgiou, Shuangqing Wang, David G Bossanyi, Rahul Jayaprakash, Nobuhiro Yanai, Nobuo Kimizuka, David G Lidzey, Andrew J Musser,

and Jenny Clark. Radiative pumping in a strongly coupled microcavity filled with a neat molecular film showing excimer emission. *Physical Chemistry Chemical Physics*, 26(20):14745–14753, 2024.

[165] Lulu Xue, Ziyang Chen, Yatong Zhang, Xiaoya Yan, Liang Zhao, Pengxue Jia, Bo Gao, and Hongyan Shi. Polariton emission property of the organic dye-doped polymer microcavity. *Journal of Materials Chemistry C*, 2025.

[166] Prathmesh Deshmukh, Lianfeng Zhao, Sitakanta Satapathy, Mandeep Khatoniar, Biswajit Datta, Barry P Rand, and Vinod Menon. Radiative pumping of exciton-polaritons in 2d hybrid perovskites. *Optical Materials Express*, 13(6):1655–1662, 2023.

[167] Leonardo Mazza, L Fontanesi, and Giuseppe Carlo La Rocca. Organic-based microcavities with vibronic progressions: Photoluminescence. *Physical Review B—Condensed Matter and Materials Physics*, 80(23):235314, 2009.

[168] Marina Litinskaya, Peter Reineker, and Vladimir M Agranovich. Fast polariton relaxation in strongly coupled organic microcavities. *Journal of luminescence*, 110(4):364–372, 2004.

[169] Ewen Smith and Geoffrey Dent. *Modern Raman spectroscopy: a practical approach*. John Wiley & Sons, 2019.

[170] N Somaschi, L Mouchliadis, D Coles, IE Perakis, DG Lidzey, PG Lagoudakis, and PG Savvidis. Ultrafast polariton population build-up mediated by molecular phonons in organic microcavities. *Applied Physics Letters*, 99(14), 2011.

[171] Ruth H Tichauer, Dmitry Morozov, Ilia Sokolovskii, J Jussi Toppari, and Gerrit Groenhof. Identifying vibrations that control non-adiabatic relaxation of polaritons in strongly coupled molecule–cavity systems. *The Journal of Physical Chemistry Letters*, 13(27):6259–6267, 2022.

[172] N Somaschi, L Mouchliadis, D Coles, IE Perakis, DG Lidzey, PG Lagoudakis, and PG Savvidis. Phonon-driven resonantly enhanced polariton luminescence in organic microcavities. In *Ultrafast Phenomena and Nanophotonics XVI*, volume 8260, pages 148–155. SPIE, 2012.

[173] Dario Ballarini, Milena De Giorgi, Salvatore Gambino, Giovanni Lerario, Marco Mazzeo, Armando Genco, Gianluca Accorsi, Carlo Giansante, Silvia Colella, Stefania D'Agostino, et al. Polariton-induced enhanced emission from an organic dye

under the strong coupling regime. *Advanced Optical Materials*, 2(11):1076–1081, 2014.

[174] Ruth H Tichauer, Dmitry Morozov, Ilia Sokolovskii, J Jussi Toppari, and Gerrit Groenhof. Identifying vibrations that control non-adiabatic relaxation of polaritons in strongly coupled molecule–cavity systems. *The Journal of Physical Chemistry Letters*, 13(27):6259–6267, 2022.

[175] Eric J Aird, Kassidy J Tompkins, Maria Paz Ramirez, and Wendy R Gordon. Enhanced molecular tension sensor based on bioluminescence resonance energy transfer (bret). *ACS sensors*, 5(1):34–39, 2019.

[176] Shashi Bhuckory, Joshua C Kays, and Allison M Dennis. In vivo biosensing using resonance energy transfer. *Biosensors*, 9(2):76, 2019.

[177] Rajesh Babu Sekar and Ammasi Periasamy. Fluorescence resonance energy transfer (fret) microscopy imaging of live cell protein localizations. *The Journal of cell biology*, 160(5):629, 2003.

[178] Joseph A Brzostowski, Tobias Meckel, Jiang Hong, Alice Chen, and Tian Jin. Imaging protein-protein interactions by förster resonance energy transfer (fret) microscopy in live cells. *Current Protocols in Protein Science*, 56(1):19–5, 2009.

[179] Wade A Luhman and Russell J Holmes. Investigation of energy transfer in organic photovoltaic cells and impact on exciton diffusion length measurements. *Advanced Functional Materials*, 21(4):764–771, 2011.

[180] Musubu Ichikawa, Eiichi Suto, Hyeon-Gu Jeon, and Yoshio Taniguchi. Sensitization of organic photovoltaic cells based on interlayer excitation energy transfer. *Organic Electronics*, 11(4):700–704, 2010.

[181] Mao Wang, Manuel Hertzog, and Karl Börjesson. Polariton-assisted excitation energy channeling in organic heterojunctions. *Nature communications*, 12(1):1874, 2021.

[182] Alessio Cargioli, Maksim Lednev, Lorenzo Lavista, Andrea Camposeo, Adele Sassella, Dario Pisignano, Alessandro Tredicucci, Francisco J Garcia-Vidal, Johannes Feist, and Luana Persano. Active control of polariton-enabled long-range energy transfer. *Nanophotonics*, 13(14):2541–2551, 2024.

[183] Th Förster. Zwischenmolekulare energiewanderung und fluoreszenz. *Annalen der physik*, 437(1-2):55–75, 1948.

[184] Gregory D Scholes. Long-range resonance energy transfer in molecular systems. *Annual review of physical chemistry*, 54(1):57–87, 2003.

[185] Daniel J Tibben, Gus O Bonin, Inseong Cho, Girish Lakhwani, James Hutchison, and Daniel E Gómez. Molecular energy transfer under the strong light–matter interaction regime. *Chemical Reviews*, 123(13):8044–8068, 2023.

[186] Stéphane Kéna-Cohen, M Davanço, and SR Forrest. Strong exciton-photon coupling in an organic single crystal microcavity. *Physical review letters*, 101(11):116401, 2008.

[187] David G Lidzey, Donal DC Bradley, Adam Armitage, Steve Walker, and Maurice S Skolnick. Photon-mediated hybridization of frenkel excitons in organic semiconductor microcavities. *Science*, 288(5471):1620–1623, 2000.

[188] V Agranovich, H Benisty, and C Weisbuch. Organic and inorganic quantum wells in a microcavity: Frenkel-wannier-mott excitons hybridization and energy transformation. *Solid state communications*, 102(8):631–636, 1997.

[189] RJ Holmes, Stéphane Kéna-Cohen, VM Menon, and SR Forrest. Strong coupling and hybridization of frenkel and wannier-mott excitons in an organic-inorganic optical microcavity. *Physical Review B—Condensed Matter and Materials Physics*, 74(23):235211, 2006.

[190] Michael Slootsky, Xiaoze Liu, Vinod M Menon, and Stephen R Forrest. Room temperature frenkel-wannier-mott hybridization of degenerate excitons in a strongly coupled microcavity. *Physical review letters*, 112(7):076401, 2014.

[191] Xiaolan Zhong, Thibault Chervy, Lei Zhang, Anoop Thomas, Jino George, Cyriaque Genet, James A Hutchison, and Thomas W Ebbesen. Energy transfer between spatially separated entangled molecules. *Angewandte Chemie International Edition*, 56(31):9034–9038, 2017.

[192] Maciej Ściesiek, Krzysztof Sawicki, Wojciech Pacuski, Kamil Sobczak, Tomasz Kazimierczuk, Andrzej Golnik, and Jan Suffczyński. Long-distance coupling and energy transfer between exciton states in magnetically controlled microcavities. *Communications Materials*, 1(1):78, 2020.

[193] Katherine Akulov, Dan Bochman, Adina Golombek, and Tal Schwartz. Long-distance resonant energy transfer mediated by hybrid plasmonic–photonic modes. *The Journal of Physical Chemistry C*, 122(28):15853–15860, 2018.

[194] Kyriacos Georgiou, Paolo Michetti, Lizhi Gai, Marco Cavazzini, Zhen Shen, and David G Lidzey. Control over energy transfer between fluorescent bodipy dyes in a strongly coupled microcavity. *ACS Photonics*, 5(1):258–266, 2018.

[195] Minjung Son, Zachary T Armstrong, Ryan T Allen, Abitha Dhavamani, Michael S Arnold, and Martin T Zanni. Energy cascades in donor-acceptor exciton-polaritons observed by ultrafast two-dimensional white-light spectroscopy. *Nature Communications*, 13(1):7305, 2022.

[196] Peter B Johnson and R-WJPrB Christy. Optical constants of the noble metals. *Physical review B*, 6(12):4370, 1972.

[197] Irving H Malitson. Refraction and dispersion of synthetic sapphire. *JOSA*, 52(12):1377–1379, 1962.

[198] Jan Matthias Lüttgens. *Strong Light-Matter Coupling with Single-Walled Carbon Nanotubes*. PhD thesis, 2022.

[199] P-A Plötz, SP Polyutov, SD Ivanov, F Fennel, S Wolter, Thomas Niehaus, Z Xie, S Lochbrunner, Frank Würthner, and O Kühn. Biphasic aggregation of a perylene bisimide dye identified by exciton-vibrational spectra. *Physical Chemistry Chemical Physics*, 18(36):25110–25119, 2016.

[200] Tobias Wesp, Tim Bruckhoff, Julian Petry, Hubert Wadepohl, and Lutz H Gade. Towards nitrogen-rich n-heteropolycycles: Synthesis of octaazaperopyrenes (oapp). *Chemistry–A European Journal*, 28(17):e202200129, 2022.

[201] Salvatore Gambino, Marco Mazzeo, Armando Genco, Omar Di Stefano, Salvatore Savasta, Salvatore Patane, Dario Ballarini, Federica Mangione, Giovanni Lerario, Daniele Sanvitto, et al. Exploring light–matter interaction phenomena under ultrastrong coupling regime. *ACS Photonics*, 1(10):1042–1048, 2014.

[202] Martin Held, Arko Graf, Yuriy Zakharko, Pengning Chao, Laura Tropf, Malte C Gather, and Jana Zaumseil. Ultrastrong coupling of electrically pumped near-infrared exciton-polaritons in high mobility polymers. *Advanced Optical Materials*, 6(3):1700962, 2018.

[203] Eero Hulkko, Siim Pikker, Ville Tiainen, Ruth H Tichauer, Gerrit Groenhof, and Jussi J Toppari. Effect of molecular stokes shift on polariton dynamics. *The Journal of Chemical Physics*, 154(15), 2021.

[204] Tao E Li, Abraham Nitzan, and Joseph E Subotnik. Polariton relaxation under vibrational strong coupling: Comparing cavity molecular dynamics simulations against fermi's golden rule rate. *The Journal of Chemical Physics*, 156(13), 2022.

[205] Shaocong Hou, Mandeep Khatoniar, Kan Ding, Yue Qu, Alexander Napolov, Vinod M Menon, and Stephen R Forrest. Ultralong-range energy transport in a disordered organic semiconductor at room temperature via coherent exciton-polariton propagation. *Advanced Materials*, 32(28):2002127, 2020.

[206] Matthew Du, Luis A Martınez-Martınez, Raphael F Ribeiro, Zixuan Hu, Vinod M Menon, and Joel Yuen-Zhou. Theory of polariton long-range excitation energy transfer. *arXiv preprint arXiv:1711.11576*, 2017.

[207] Ding Xu, Arkajit Mandal, James M Baxter, Shan-Wen Cheng, Inki Lee, Haowen Su, Song Liu, David R Reichman, and Milan Delor. Ultrafast imaging of polariton propagation and interactions. *Nature Communications*, 14(1):3881, 2023.

[208] Clara Bujalance, Laura Caliò, Dmitry N Dirin, David O Tiede, Juan F Galisteo-López, Johannes Feist, Francisco J García-Vidal, Maksym V Kovalenko, and Hernán Míguez. Strong light–matter coupling in lead halide perovskite quantum dot solids. *ACS nano*, 18(6):4922–4931, 2024.

[209] Tuomas Pajunpää, Fedor Nigmatulin, Suvi-Tuuli Akkanen, Henry Fernandez, Gerrit Groenhof, and Zhipei Sun. Polariton-assisted long-distance energy transfer between excitons in two-dimensional semiconductors. *Physical Review B*, 109(19):195409, 2024.

[210] Guosong Hong, Alexander L Antaris, and Hongjie Dai. Near-infrared fluorophores for biomedical imaging. *Nature biomedical engineering*, 1(1):0010, 2017.

[211] Guangcun Chen, Yuheng Cao, Yanxing Tang, Xue Yang, Yongyang Liu, Dehua Huang, Yejun Zhang, Chunyan Li, and Qiangbin Wang. Advanced near-infrared light for monitoring and modulating the spatiotemporal dynamics of cell functions in living systems. *Advanced science*, 7(8):1903783, 2020.

[212] Antoni Rogalski. Recent progress in infrared detector technologies. *Infrared Physics & Technology*, 54(3):136–154, 2011.

[213] Paul M Pellegrino, Ellen L Holthoff, and Mikella E Farrell. *Laser-based optical detection of explosives*. CRC Press, 2018.

[214] Harry A Atwater and Albert Polman. Plasmonics for improved photovoltaic devices. *Nature materials*, 9(3):205–213, 2010.

[215] Martin Held, Arko Graf, Yuriy Zakharko, Pengning Chao, Laura Tropf, Malte C Gather, and Jana Zaumseil. Ultrastrong coupling of electrically pumped near-infrared exciton-polaritons in high mobility polymers. *Advanced Optical Materials*, 6(3):1700962, 2018.

[216] Andreas Mischok, Sabina Hillebrandt, Seonil Kwon, and Malte C Gather. Highly efficient polaritonic light-emitting diodes with angle-independent narrowband emission. *Nature Photonics*, 17(5):393–400, 2023.

[217] Zehua Hu, Tanjung Krisnanda, Antonio Fieramosca, Jiaxin Zhao, Qianlu Sun, Yuzhong Chen, Haiyun Liu, Yuan Luo, Rui Su, Junyong Wang, et al. Energy transfer driven brightening of mos2 by ultrafast polariton relaxation in microcavity mos2/hbn/ws2 heterostructures. *Nature Communications*, 15(1):1747, 2024.

[218] Dmitriy Dovzhenko, Maksim Lednev, Konstantin Mochalov, Ivan Vaskan, Yury Rakovich, Alexander Karaulov, and Igor Nabiev. Polariton-assisted manipulation of energy relaxation pathways: donor–acceptor role reversal in a tuneable microcavity. *Chemical Science*, 12(38):12794–12805, 2021.

[219] Matthew Du, Luis A Martínez-Martínez, Raphael F Ribeiro, Zixuan Hu, Vinod M Menon, and Joel Yuen-Zhou. Theory for polariton-assisted remote energy transfer. *Chemical science*, 9(32):6659–6669, 2018.

[220] RJ Holmes and SR Forrest. Strong exciton-photon coupling and exciton hybridization in a thermally evaporated polycrystalline film of an organic small molecule. *Physical review letters*, 93(18):186404, 2004.

[221] Vladimir M Agranovich, M Litinskaia, and David G Lidzey. Cavity polaritons in microcavities containing disordered organic semiconductors. *Physical Review B*, 67(8):085311, 2003.

[222] Xiaolan Zhong, Thibault Chervy, Shaojun Wang, Jino George, Anoop Thomas, James A Hutchison, Eloise Devaux, Cyriaque Genet, and Thomas W Ebbesen. Non-radiative energy transfer mediated by hybrid light-matter states. *Angewandte Chemie*, 128(21):6310–6314, 2016.

Eidesstattliche Versicherung

gemäß §8 der Promotionsordnung für die Gesamtfakultät für Mathematik, Ingenieur- und Naturwissenschaften der Universität Heidelberg

1. Bei der eingereichten Dissertation zu dem Thema *„Strong Light-Matter Coupling with N-Heteropolycycles“* handelt es sich um meine eigenständig erbrachte Leistung.
2. Ich habe nur die angegebenen Quellen und Hilfsmittel benutzt und mich keiner unzulässigen Hilfe Dritter bedient. Insbesondere habe ich wörtlich oder sinngemäß aus anderen Werken übernommene Inhalte als solche kenntlich gemacht.
3. Die Arbeit oder Teile davon habe ich bislang nicht an einer Hochschule des In- oder Auslands als Bestandteil einer Prüfungs- oder Qualifikationsleistung vorgelegt.
4. Die Richtigkeit der vorstehenden Erklärungen bestätige ich.
5. Die Bedeutung der eidesstattlichen Versicherung und die strafrechtlichen Folgen einer unrichtigen oder unvollständigen eidesstattlichen Versicherung sind mir bekannt.

Ich versichere an Eides statt, dass ich nach bestem Wissen die reine Wahrheit erklärt und nichts verschwiegen habe.

Heidelberg, 21.05.2025

Parvathi Valsalan